UNIVERSITY OF SOUTHAMPTON

The Evolution of Radio Galaxies

Yang Wang

Submitted for the degree of Doctor of Philosophy

SCHOOL OF PHYSICS AND ASTRONOMY
FACULTY OF SCIENCE

February 28, 2010

ABSTRACT

Radio galaxies with extended lobes are believed to interact strongly with their environment. In this thesis, I investigate the evolution of radio galaxies with different properties and track them through the cosmological ages.

In Chapters 2 and 3, I perform a "Monte-Carlo-based" population synthesis study which combines a model for the luminosity evolution of an individual FR II source with the radio luminosity function as a function of redshift. The artificial samples generated are then compared with complete observational samples. The results show that the properties of FR II sources are required to evolve with redshift. I also study the distribution of the jet properties as a function of redshift. From currently available data it is not possible to constrain the shape of the distribution of environment density or age, but jet power is found to follow a power-law distribution with an exponent of approximately -2. This power-law slope does not change with redshift out to $z = 0.6$. I also find the distribution of the pressure in the lobes of FRII sources to evolve with redshift up to $z \sim 1.2$.

FR I sources are not yet considered in Chapter 3, as existing analytical models for FR I soures are less successful. Thus in Chapters 4, I present a new analytical model for FR I jets. The model is based on a mixing-layer structure in which an initially laminar, relativistic flow is surrounded by a shear layer. I apply the appropriate conservation laws to constrain the jet parameters, starting the model where the radio emission is observed to brighten abruptly. Applying the model to a sample of the well-observed FR I sources, including example 3C 31, I find a self-consistent solution, from which I derive the jet power together with other properties like the entrainment rate.

The model in Chapter 4 leads an idea of estimating the maximum lengths and ages of the FR II sources by considering the entrainment process during their evolutions. In Chapter 5, I consider the laminar part of the jet may be destroyed due to the entrainment under certain assumpsions, in which case the radio outflows cease to be FR IIs after a few 10^8 yrs, at which point they have typically reached sizes of around 1 Mpc. Based on this idea, I then further discuss a plausible transition process from FR IIs into FR Is.

Contents

List of Figures

List of Tables

Chapter 1

Introduction

1.1 Active galactic nuclei (AGN)

An active galactic nucleus (AGN) is a compact, intrinsically luminous region at the centre of a galaxy. It produces strong emission in almost all wavebands, from X-ray through the optical into the radio. It is thought that AGN must be powered by accretion onto supermassive black holes (Lynden-Bell, 1969), which are believed to exist in all AGN (Magorrian et al., 1998). It is not clear why AGN formation takes place at the centres of some galaxies, but it is believed that it occurs as part of the evolution of all galaxies (Kauffmann et al., 2003).

Powerful AGN can have very high luminosities and dominate the objects observed at high redshifts. From X-ray observations, we know that there are significant interactions between the galaxies and the surrounding gas on scales of several tens to hundreds of kpc from their central AGN (e.g. Bohringer et al., 1995; Reynolds et al., 2005). A denser gas environment may imply a more massive galaxy (O'Sullivan et al., 2001), while more massive galaxies also contain more massive black holes at their centre (e.g. Kormendy & Richstone, 1995). Thus, AGN are believed to influence a significant fraction of the matter-filled universe (Gopal-Krishna & Wiita, 2001; Kronberg et al., 2001; Rawlings & Jarvis, 2004), AGN activity is often accompanied by jet production. Jets with highly collimated structure contain fast particles which are produced from the innermost regions of the accretion disks in the centres of AGN, although the jet production mechanism is still not well understood. Even though synchrotron and inverse-Compton processes make jets radiate in all wavebands, from the radio to the gamma-ray, the jets are most obvious in radio observations. Based on the radio properties, AGN can be divided into two groups: radio-quiet AGN and radio-loud AGN. In the former case, jets and their emission can be ignored. In the latter case, the luminosity from the jets and related lobes dominates at least in the radio band.

1.2 Classification of AGN

AGN are usually subdivided into different classes based on their physical/observational properties. Generally speaking, most AGN can be classified as Seyfert galaxies, quasars, blazars or radio galaxies. I list the main physical features for each group below:

Seyfert galaxies are radio-quiet AGN which were first defined by Seyfert (1943). They have very bright nuclei, and their spectra have notable emission lines. Seyfert galaxies are classified as Type I when their spectra show both narrow and broad emission lines, and as Type II when only narrow lines are observed. The host galaxies of Seyferts are usually spiral or irregular galaxies. Most Seyfert galaxies are observed at low redshifts, but this may due to selection effects, as they are not powerful enough to be observed at high redshifts.

Quasars look like point sources, but considering their high redshifts, they are the most powerful and energetic objects in the known universe. The luminosities of some quasars change rapidly in optical and X-ray bands, and this indicates that the sizes of quasars are small, may be as small as the Solar System. Quasars can be observed in all wavebands with huge amount of overall energy. Initially, it is hard to understand how such a small system can be so powerful, with luminosities exceeding that of the whole Milky Way. However, it is now widely accepted that this is because the associated relativistic jets point nearly directly towards us in most cases. I will give a further introduction on this point in next section, which will talk about the AGN unification scheme.

Blazars are very compact sources with rapid and large amplitude flux variability. Particularly powerful blazars are referred to the *Optically Violent Variable* (OVV) quasars, while the less powerful ones are referred to as *BL Lac* objects. Another important difference between these two subsets is that OVV quasars exhibit strong broad emission lines, while the spectra of BL Lac objects are dominated by a featureless non-thermal continuum.

Radio galaxies show obvious radio emissions from nuclear and extended structure. The radio emission is nearly always due to the synchrotron process and contains important information about how AGN evolve and interact with their environment. I will discuss radio galaxies in more details below, as I will be focusing on them in this thesis.

1.3 AGN Unification

Based on detailed studies of the different types of AGN, an AGN unification scheme was introduced that attempts to explain the relationships between the various classes. Figure 1.1 is a sketch illustrating the unification scheme of AGN, taken from Ferrari (1998). Although detailed observations show that this unification scheme may not capture all the complexities of the AGN populations, it is still widely accepted that orientation and luminosity are the key factors in determining the observational appearance of AGN.

For radio-loud AGN, the scheme considers two populations, distinguished by their luminosities. At the high luminosity end, the scheme assumes that FR II radio galaxies, quasars and OVVs all belong to the same parent population. The observed difference between these three populations must then primarily be due to different viewing angles and luminosities. For high luminosity and large viewing angles (viewed edge-on), a normal FR II source will be observed with narrow line emission properties. When the viewing angle decreases, the optical core begins to dominate the host galaxy, and a broad line quasar will be observed. In extreme conditions, when viewed nearly along the jet axis, a beamed

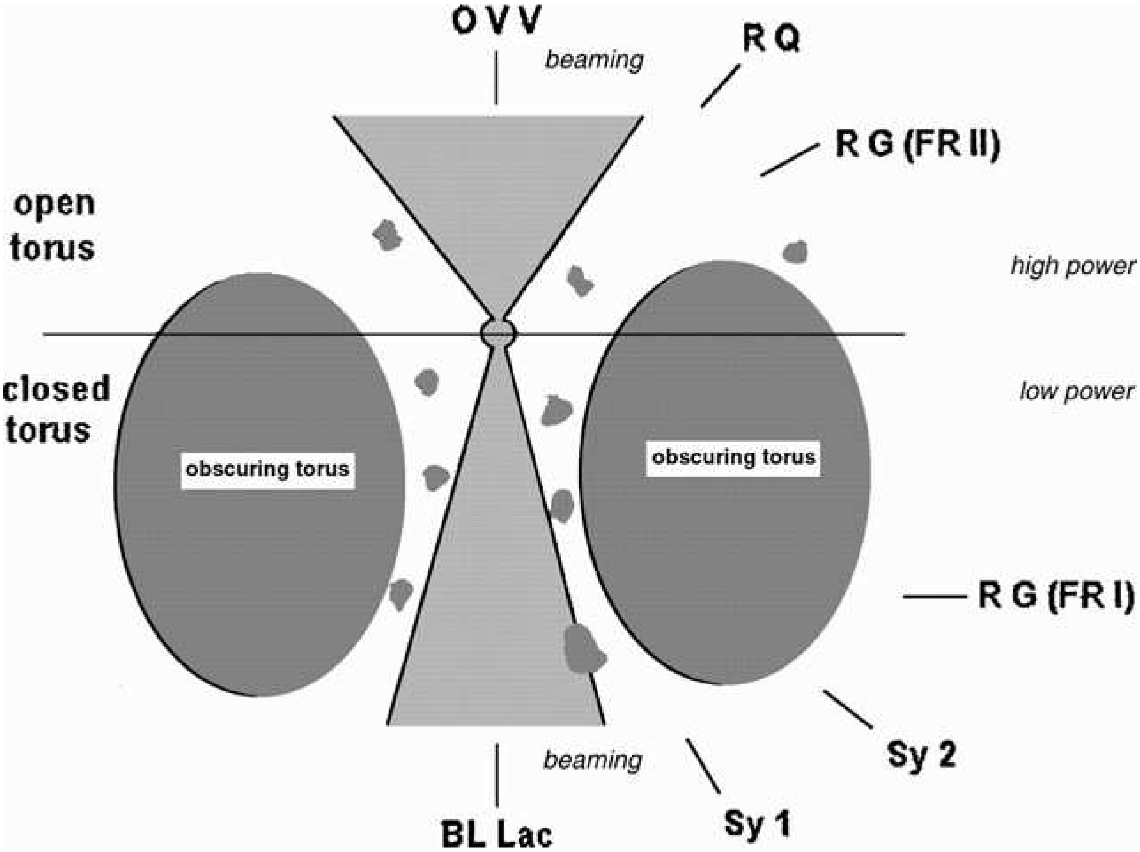

Figure 1.1: A sketch of the unification scheme. The upper part corresponds to high-power sources with the jet emerging from an open torus, the lower part to low-power sources with the jet emerging from a closed torus. Different morphologies are produced by the orientation of the observer with respect to the jet/obscuring torus. OVV, optically violent variables; RQ, radio-loud quasars; RG, radio galaxies; Sy, Seyfert galaxies. The drawing is taken from Ferrari (1998)

OVV object will be observed.

Similar arguments apply for low-luminosity radio-loud AGN, suggesting that the FR I radio galaxies and BL Lac objects belong to the same parent population. Thus a low-luminosity radio galaxy with a weak jet will be observed as normal FR I radio galaxy when viewed edge-on, but as a BL Lac object when the line of sight is parallel with the jet axis.

This unification scheme could also apply at the low power end. When the low-power AGN is viewed edge-on, only the narrow line region can be seen, so a Seyfert II galaxy will be observed. As the viewing angle decreases, the observer can begin to see the broad line region and a Seyfert I galaxy will be observed. Finally, when one observes the galaxy directly along the jet axis, one sees a radio-quiet BL Lac objects.

1.4 Advantages of radio observations

Radio observations are unique compared with observations in other wavebands. They do not depend on the time of day, the weather conditions or the environment. This allows radio telescopes to be built anywhere with radio-quiet environment. Moreover, interferometry makes it possible to connect large numbers of antennas together to form high-sensitivity and high-resolution arrays, such as the Very Large Array (VLA), and even connect global dishes and arrays together with Very Long Baseline Interferometry (VLBI). The next generation of telescopes for radio astronomy which are currently being developed, will be even more powerful. The VLA is being upgraded to the EVLA, which will offer better sensitivity, resolution and imaging capability. The Low Frequency Array (LOFAR), which is being built across Europe, is expected to start operations in the near future. Finally, the development of the Square Kilometer Array (SKA), which is an international radio telescope for the 21st century, is also in progress.

AGN and radio galaxies were first observed in the radio band in the 1950's by Cambridge University and Sydney University. Due to the advantages of radio observations, we can observe very distant and powerful active galaxies with massive black holes in radio band. Thus, radio astronomy has been closely connected with the study of cosmology. In particular, powerful radio telescopes can provide us with detailed images of radio galaxies in the deep universe, allowing us to study the evolution of galaxies at high redshift along with the evolution of their environments.

1.5 Classification of radio galaxies

Fanaroff & Riley (1974) split extragalactic radio sources into two classes based on their

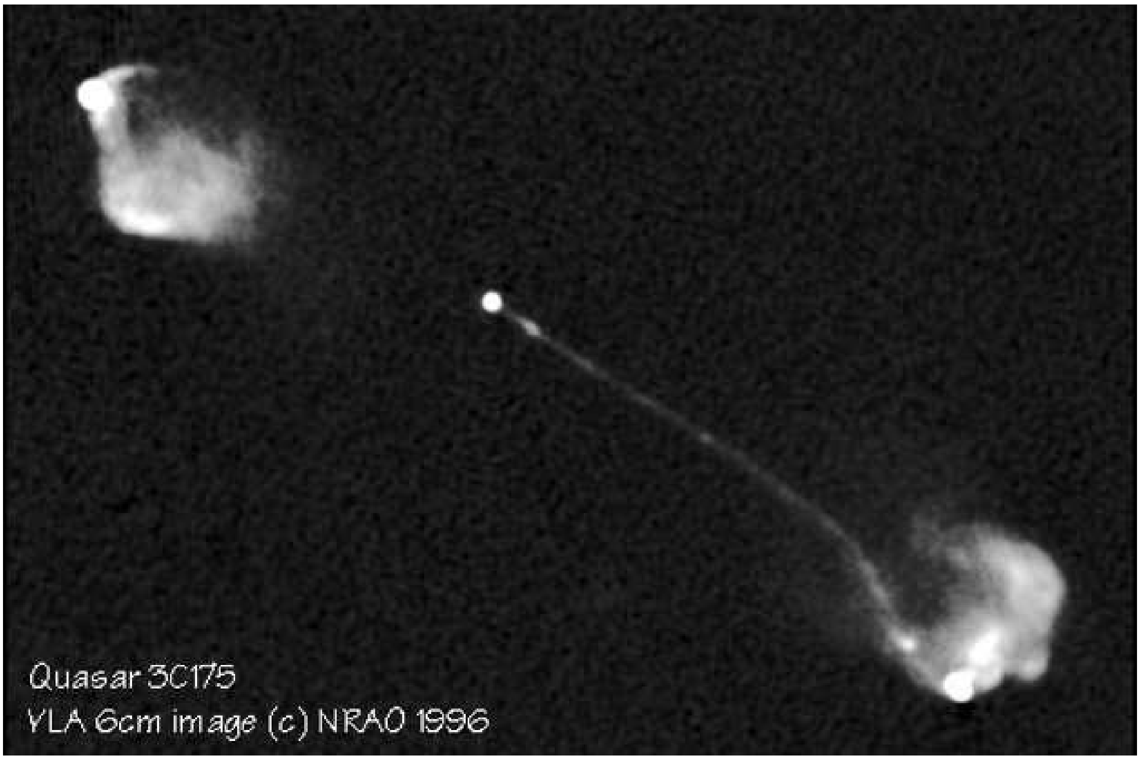

Figure 1.2: A typical FR II source: 3C 175. The VLA observation shows a brighting core, two hotspots at both ends of the jet and lobe structure. There is a slim jet connecting the core and the hotspot.

morphology. Fanaroff-Riley class I (FR I) objects have bright cores and edge-darkened lobes, while Fanaroff-Riley class II (FR II) objects are edge-brightened and contain hotspots. This classification has proved to be extremely robust: the division between the classes depends primarily on radio luminosity (Fanaroff & Riley, 1974), with FR II sources being more powerful, but also on the stellar luminosity of the host galaxy (Ledlow & Owen, 1996). There are significant differences between the structures of the jets in the two classes: those in FR I sources often flare close to the nucleus and have large opening angles, whereas their equivalents in FR II sources are highly collimated out to the hotspots (Bridle, 1984). In Figure 1.2, I show the structure of 3C 175, which is a typical FR II source, while in Figure 4.5 I show a typical FR I source, 3C 31.

Considering their morphologies in more detail reveals additional differences between FR Is and FR IIs. FRII sources have fairly homogeneous structures with jets extending from the AGN to very bright hotspots surrounded by low surface brightness lobes. By

Figure 1.3: A typical FR I source: 3C 31. The VLA observation shows turbulence tailed structure instead of hotspot structure at the end of the jet. The jet is bright in the center and dark on the edge.

contrast, FRIs are more complex and have only one common feature: no hot spots at the outer end of the jet. About half of the FR I sources show a *fat double* morphology with a well-defined lobe structure similar to those in FR II, while the rest inflate turbulent lobes after passing through a so-called brightening point, with plumes or tails at the end (Owen & Laing, 1989; Owen & White, 1991; Parma et al., 2002). In the local universe, FRI sources are more common, but at high redshift, most of the sources observed are FRIIs(, though this is probably mainly due to the selection effects).

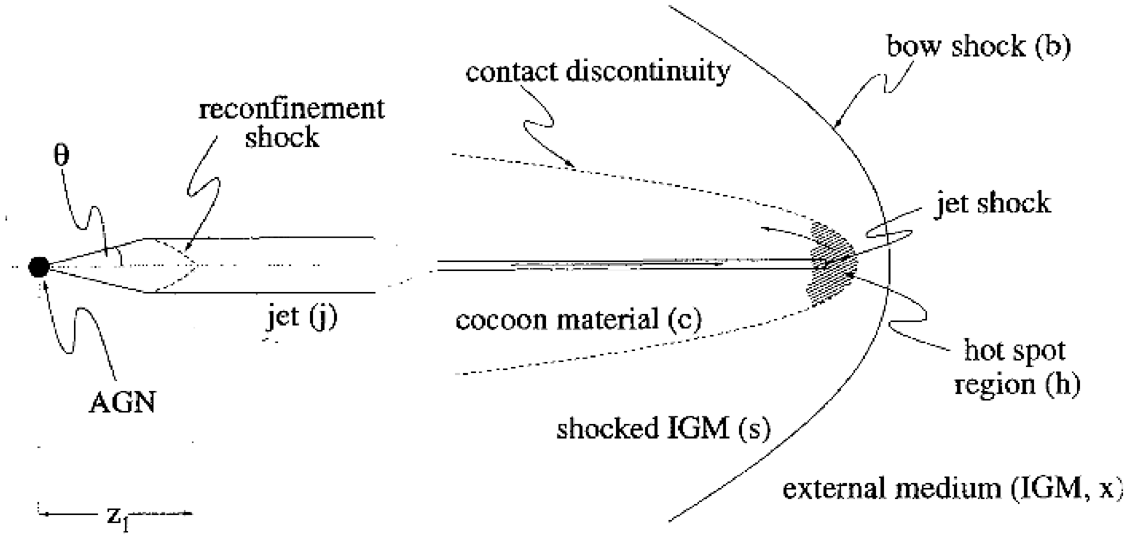

Figure 1.4: Basic elements of a FR II radio galaxy. This sketch is taken from Figure 1 of KA97.

1.5.1 Models for FR II radio galaxies

Many analytical models for FR II sources have been published. The widely accepted structure of FR II sources contains a jet propagating from the central AGN. The jet contains highly relativistic particles, which are powered by the AGN. The jet impacts the surrounding environment and forms a shock at its end. The pressure and density are extremely high at this point, so the shock produces strong radio emission. This is referred to as the *hotspot*. Figure 1.4.shows a sketch of the structure of an FR II source. The particles are then accelerated in the hotspot and injected into the lobe around the jet. The lobe is more likely to be over-pressured as it expands into the environment. However, Falle (1991) and Kaiser & Alexander (1997, hereafter KA97) assumed that the jet is in pressure-equilibrium with its own lobe, and showed that the expansion of the lobe and the bow shock in front of it is self-similar. The radio lobe luminosity evolution has been calculated by Kaiser et al. (1997, hereafter KDA). The radio synchrotron emission of the lobes is due to relativistic electrons spiralling in the magnetic field of the lobe. The model of KDA self-consistently takes into account the energy losses of these electrons due to the adiabatic expansion of the lobes, synchrotron radiation and inverse Compton scattering of cosmic microwave background photons off the electrons. Blundell et al. (1999, hereafter

BRW) essentially follows the KDA prescription, but there are two main differences. The first is that KDA assumes a constant injection index while BRW assume the injection index is a function of the energy of the particles injected, which is determined by the dwell times that particles spend in the hotspot. This will affect the energy distribution of the total particle population injected. The second is that the adiabatic expansion losses out of the hotspot are determined not by the pressure of the entire head region but only by the pressure of the hotspot. The pressure of the head region only determines the growth of the source length. As the jet power strongly affects the hotspot pressure, it will also affect the energy loss processes, which leads to a strong P-α relationship. Meanwhile, the adiabatic expansion losses include that from both the hotspot into the lobe and the on-going lobe expansion, so the jet does not grow in a self-similar way, which is assumed by KDA model, and the axial ratio changes with jet age. Manolakou & Kirk (2002, hereafter MK) also follows the KDA prescription but differ in the way that the relativistic particles are injected from the jet into the lobe, and in the treatment of loss terms and particle transport. The radio luminosity evolutions from these three models show significant differences. I will describe these models in more details in Chapter 3.

1.5.2 Models for FR I radio galaxies

Attempts to construct global models of the evolution of FR I sources, linking observable quantities such as linear size and radio luminosity, have been less successful to date. The observations suggest that FR I jets are initially relativistic, but decelerate on kiloparsec scales, whereas FR II jets remain relativistic until they terminate (e.g. Laing 1993). However, the process of deceleration in FR I jets appears to be complex, and may involve a transition to turbulent flow. A number of authors agree that there must mass loading during the deceleration process (Komissarov, 1994; Laing & Bridle, 2002a). Two principal mechanisms have been suggested to account for this mass loading: the stellar winds contained within the jet area (Komissarov, 1994; Bowman et al., 1996) or entrainment from the environment across an unstable boundary layer (Canto & Raga, 1991). Bicknell (1994, hereafter B94) considered energetically dominated jet and used conservation laws of mass, momentum and energy to consider the feasiblity of deceleration. This work takes both internal and external entrainment into account. I will use it as a starting point in building my own analytical model later in Chapter 4.

1.5.3 The transition between FR I and FR II sources

Generally speaking, FR IIs are more powerful than FR Is, with a transition radio luminosity around $P_{178\mathrm{MHz}} \sim 10^{25}\mathrm{W\,Hz^{-1}\,sr^{-1}}$, although a transition luminosity also applies in the optical band (Owen & Ledlow, 1994). FRIIs are preferentially associated with more optically luminous galaxies. The value of the transition luminosity between the FR classes is not precise. It depends on the properties of the host galaxies (Ledlow & Owen, 1996) and increases with increasing optical luminosity of the host galaxies. The origin of the *FR I/II dichotomy* has been discussed extensively in the literature. One possibility is that it is linked to the intrinsic properties of the jet itself (Meier et al., 1997; Urpin, 2002), another is that the interaction between the jet and its environment is the key factor (Falle, 1991; Alexander, 2000; Kaiser & Best, 2007; Kawakatu et al., 2009). However, the underlying physics leading to the FR I/FR II transition are still not well understood. In Chapter 5 of this thesis, I will discuss a possible evolutionary connection between FR Is and FR IIs by considering the termination of FR II sources due to entrainment.

1.6 The P-D diagram

The P-D diagram introduced by Shklovskii (1963) is one of the most important tools for studying the evolution of radio sources. The diagram uses the two main observable properties of radio sources: radio luminosity, P, and linear size, D. Baldwin (1982) pointed out that the P-D diagram is analogous to the Hertzsprung-Russell diagram for stars. However, P-D diagram is a blunter instrument than H-R diagram as it contains sources with different redshifts. Thus, the source distribution in the P-D plane depends on both the intrinsic evolution of individual sources and the cosmological evolution of the source population as a whole. Since we may assume that source lifetimes are considerably shorter than the age of the universe, the P-D diagram has been used to place key constraints on the evolution of individual sources (Baldwin, 1982; Neeser et al., 1995) and to look for consistency between data and models (KDA; BRW; MK). In this work, I am going to investigate the evolution of radio sources across cosmological epochs, so the redshift of the sources will need to be taken into account at the same time. I will therefore introduce a 3-dimensional P-D-z data cube, as described later in Chapter 2.

Figure 1.5 is taken from Figure 1 of KDA and shows the distribution of a number of radio sources on the P-D diagram. The curves across the diagram are the evolution tracks of individual sources predicted by the KDA model for different model parameters. A given radio source is thought to start its evolution in the upper left part of the P-D diagram at high luminosity and small size. As it ages, the source grows larger, and its luminosity decreases, so it will move to the lower right part of the P-D diagram. Different evolutionary models (KDA, BRW, MK) give similar tracks and only differ from each other quantitatively, but not qualitatively.

1.7 The formation and evolution of radio galaxies

The number counts of radio sources contain important information about the distribution of radio sources throughout cosmological time. Longair (1966) suggested that the most powerful radio sources must undergo strong evolution, since the observations covered 5 orders of magnitude in radio flux density, while the number counts of the radio galaxies vary by only 2 orders of magnitude with redshift.

Initially, the evolution of radio source population was modeled by assuring the existence of two distinct populations. More specifically, the high-luminosity population was assumed to undergo strong cosmological evolution, while the low-luminosity one was assumed not to evolve very much with cosmological epoch. Wall (1980) suggested that the sources in these two populations might corresponded to the FR I and FR II sources, respectively. Jackson & Wall (1999) developed this idea and considered FR I and FR II sources as different classes of object with different evolutionary processes. By contrast, Dunlop & Peacock (1990) did not treat FR Is and FR IIs separately, but allow a cosmological evolution depending

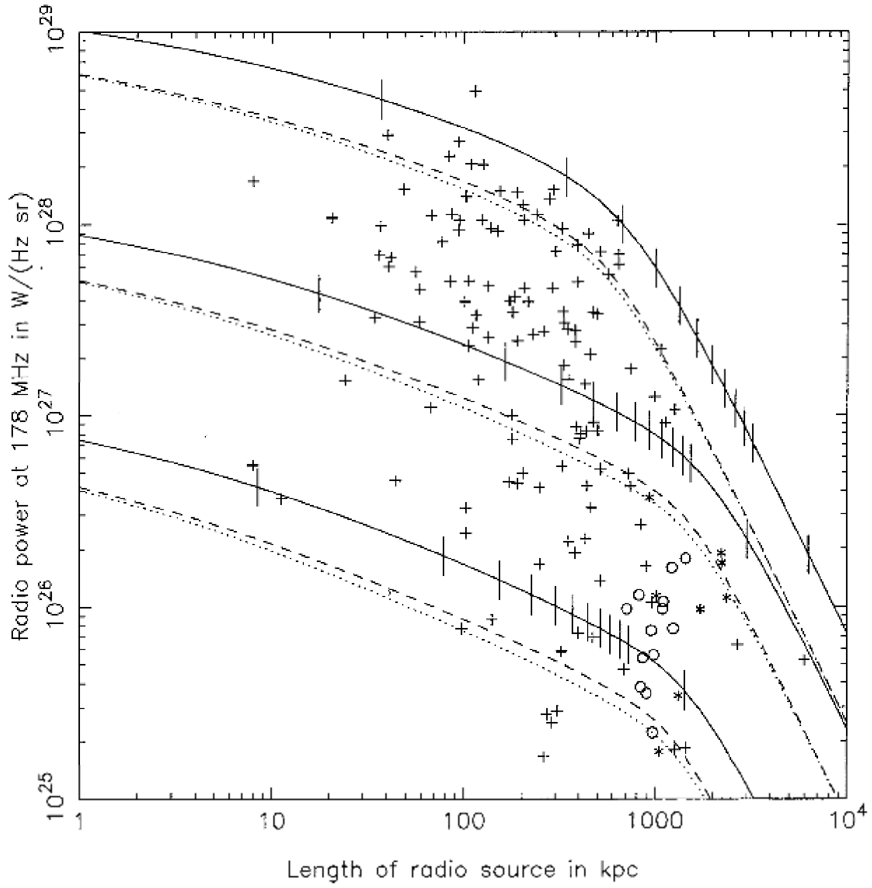

Figure 1.5: Evolutionary tracks of radio sources on P-D diagram, taken from Figure 1 of KDA.

smoothly on the radio luminosity. However, Snellen & Best (2001) analysed FR Is in the Hubble deep field and showed that it is unlikely that FR I radio sources undergo no cosmological evolution between $0 < z < 1$. Thus, both FR I and FR II sources should probably be assumed to evolve with redshift. Willott et al. (2001, hereafter W01) adopted a dual-population scheme, but instead of considering an explicit FR I/FR II divide, they divided the whole population into genetic low-power sources and high-power sources. Both of the populations evolve with redshift, but in different ways. In this thesis, I will use the W01 model, since it is based on the most complete samples.

Cosmological evolution models based on deep surveys indicate that the comoving density of radio galaxies was higher during the quasar era (around redshift z=2) as compared to the present epoch (Jackson & Wall, 1999; Willott et al., 2001; Grimes et al., 2004). Dunlop & Peacock (1990) estimated the radio luminosity function (RLF) of steep-spectrum radio sources and found positive evolution in number density out to $z \approx 2$ and a decline beyond this redshift. Optical and hard X-ray observations of powerful AGN reveal a similar trend (e.g. Ueda et al., 2003). Hopkins et al. (2007) studied the quasar luminosity functions from multi-wavelength bands and found a peak at $z = 2.15$ in the redshift range of $z = 0 - 6$.

As radio galaxies with jet structures can trigger feedback effects in their environments, they play an important role in star formation and star burst activities (e.g. Chokshi, 1997; Gopal-Krishna & Wiita, 2001; Kronberg et al., 2001; Furlanetto & Loeb, 2001; Silk, 2005). The fact that the star formation rate was also considerably higher in the quasar era is in line with this idea (e.g. Gopal-Krishna & Wiita, 2001; Kronberg et al., 2001). Observations in optical and sub-mm wavebands also support the notion that jets can induce star formation (Best et al., 1996; Dey et al., 1997; Bicknell et al., 2000; Greve et al., 2006). All of this evidence indicates that radio galaxies may form in high-density regions of the universe and play an important role in regulating star formation and the overall growth of galaxy clusters.

1.8 This work

It is difficult to determine the cosmological evolution of radio galaxies directly from observations, as the number of well-observed radio sources in complete samples is small. However, based on an evolution model of individual radio sources, Monte-Carlo simulation can be carried out to generate artificial samples containing large numbers of radio sources. These artificial samples can then be compared to the observed samples to test how well the artificial samples match the data. The aim of Chapter 3 is to study the distribution of the properties of radio galaxies throughout cosmological time by finding the best-fitting model parameters as a function of redshift. In Chapter 3, I therefore constrain the cosmological evolution of jet ages and environment densities, as well as the distribution of jet powers.

As already noted above, the Monte-Carlo simulations and tests carried out in Chapter 3 only consider FR II sources, since no suitable model for FR Is was available when this work was carried out. This provides motivation for Chapter 4, in which I build an analytical model for FR I sources. Observations show that there are strong interactions between the outflows and their environments. Thus entrainment may play an important role in the evolution of FR I sourcces. I therefore adopt a layered structure that includes a shear mixing layer from Canto & Raga (1991) and apply the appropriate relativistic conservation laws. In this way, I describe the steady state of 3C 31-type FR I radio sources. Among other things, the model can predict the power/mass flux of the jets and their interactions with the environment.

Having considered this mixing-layer model for FR I sources, I consider whether entrainment may also be relevant for FR IIs, and, if so, what the implications would be. In Chapter 5, I therefore ask if entrainment might ultimately destroy the jet in FR IIs and thus set a limit on the maximum sizes and ages of these sources. I also consider the evolution of the sources beyond their death as FR IIs and show that they may ultimately emerge as classic FR Is.

1.9 Synopsis of the thesis

In *Chapter 2*, I give a detailed description of the flux-limited samples which are used in this thesis. The observational samples include 3CRR, 6CE, 7CRS and BRL samples. I also present the classification of the first and second fields of the 7CRS sample in this chapter.

In *Chapter 3*, I present multi-dimensional Monte-Carlo simulations to generate artificial samples of radio sources. These samples are compared with the observational samples in order to find the best fit parameters describing the evolution of the FR II source population.

In *Chapter 4*, I construct an analytical model for FR I sources based on a layered structure, relativistic conservation laws, and observations of a well-observed FR I source, 3C 31.

In *Chapter 5*, I estimate the maximum lengths and ages of FR II sources by considering the entrainment process working on them. Following this idea to its logical conclusion, I then sketch a plausible scenario for the transition of FR IIs into FR Is.

In *Chapter 6*, I summarize the main results obtained in this thesis and discuss the directions they suggest for future work on the evolution of radio sources.

Appendices list the observational properties of the radio samples I used in this paper. In all chapters, I use a cosmological model with $H_0 = 71\,\mathrm{km\,s^{-1}\,Mpc^{-1}}$, $\Omega_\mathrm{M} = 0.3$, $\Omega_\Lambda = 0.7$.

Chapter 2

Complete samples of radio galaxies

Many deep surveys have been carried out in order to understand the evolution of radio sources in the high redshift universe. Various samples based on these surveys have been published in recent years. My work in this thesis uses analytical FR II models connecting the sources properties with the radio emission of the lobes without the hotspots. The emission from the hotspots is most important at high frequencies, where it may even dominate the total emission. Thus, in order to minimize the effect of the hotspot, these models should ideally be applied and compared to samples observed at low frequency. As I am going to carry out population studies, I need samples that contain all radio sources within a well-defined sky area with radio fluxes above a specified limit at the observing frequency. Additionally, the data should include the angular sizes and fluxes of the radio lobes. Finally, in order to investigate the cosmological evolution, I also need the cosmological redshifts of the host galaxies of all radio sources in the sample as measured by optical observations. The resulting criteria for suitable samples can be summarized as of:

1. The survey is carried out at low frequency.
2. All the radio sources in a certain sky area above a certain flux are included.
3. Angular size (θ), radio flux (s) and redshift (z) have all been observationally determined for all sources.

Based on these criteria, the complete samples I am going to use in this thesis are the 3CRR, 6CE, 7CRS and BRL samples. In this chapter, I will give detailed descriptions of these four samples.

2.1 The 3CRR sample

The Third Cambridge Catalogue of Radio sourcces (3C) is a catalogue of radio sources observed initially at 159 MHz, and subsequently at 178 MHz. A revised catalogue (3CR) using observations at 178 MHz was published by Bennett (1962). Further revision was given by Laing et al. (1983), and this is the well-known 3CRR sample which has been used in many studies of radio galaxies.

The 3CRR sample has a flux-limit of $S_{178} \geq 10.9$ Jy at 178 MHz and includes all radio sources with Declination $> 10^{\circ}$ and at $> 10^{\circ}$ from the Galactic plane. It covers a sky area with a solid angle of 4.23 sr, which is the biggest among all the samples used in this thesis. The 3CRR sample contains 173 sources in total. However, two of these sources, 3C 345 and 3C 454.3, are flat-spectrum quasars which should be excluded, as their fluxes are raised above the selection limit by Doppler-boosting cores. The source 3C 231 is also excluded, as it is a nearby starburst galaxy rather than a radio-loud AGN. The remaining 170 sources in the sample have been made electronically available by Chris Willott at www.science.uottawa.ca/∼cwillott/3crr/3crr.html. However, I list all the sources with their names, redshifts, angular sizes, flux densities and morphology classifications in Appendix 1.

2.2 The 6CE sample

The Sixth Cambridge Sample (6CE) constructed by Eales (1985) is based on the 6C survey and was re-selected and updated by Rawlings et al. (2001). This sample is observed at 151 MHz and goes fainter than the 3CRR sample, covering a flux range of $2.0 \leq S_{151} \leq 3.93$ Jy. Note that the 6CE sample is the only sample that has an upper flux limit as well as a lower flux limit. The sample covers the sky area $08^{h}20^{m}30^{s} < \mathrm{RA(B1950)} < 13^{h}01^{m}30^{s}$ and $34^{\circ} < \mathrm{Dec.(B1950)} < 40^{\circ}$. This amounts to 0.102 sr, and the total number of the sourcses in the sample is 59. For detailed descriptions of the sample and the way in which source morphology and angular size were determined, please see Eales (1985). The angular sizes of some sources were updated by Naundorf et al. (1992). The revised flux density at 151 MHz and the redshift of the sources can be found in Rawlings et al. (2001). The redshifts of some sources were updated later by Inskip et al. (2002). The source 6C 1036+3616 is so close to a bright star that it is impossible to obtain any effective optical/near-IR follow-up, and this source as therefore excluded. I summarize and list the parameters of the remaining 58 sources in Appendix 2.

2.3 The 7CRS sample

The Seventh Cambridge Redshift Survey (7CRS) is a combination of the sub-divisions I,II and III of the original 7C survey (McGilchrist et al., 1990), which are all observed at 151 MHz. Together they cover a sky area of 0.022 sr and contain 130 radio sources. The 7C-III sample contains 54 radio sources within 3° of $18^{h}00^{m} +66^{\circ}$. Their redshifts, flux-densities, spectral indexes and morphologies can be found in Lacy et al. (1999). The 7C-I and 7C-II samples overlap with fields 5C6 and 5C7, respectively, of the original 5C survey (Pearson & Kus, 1978). The 7C-I sample is centered on $02^{h}14^{m}00^{s}$, $+32^{\circ}00'00''$ (epoch B1950.0), covers a sky area of 0.0061 sr and contains 37 sources. The 7C-II sample is centered on $08^{h}17^{m}00^{s}$, $+27^{\circ}00'00''$ (epoch B1950.0), covers a sky area of 0.0069 sr and contains 39 sources, including one souce in common with the 3CRS sample (3C 200) and one flat-spectrum quasar 5C7 230. I therefore remove these two objects from the sample. Part of the data for these two sub-samples are published in Willott et al. (2002) and Willott et al. (2003). They are also referred to in many papers (e.g. Grimes et al., 2004), but have not been published separately in the refereed literature. However, the full data could be obtained from www-astro.physics.ox.ac.uk/∼sr/grimes.html. As different types of radio sources are likely to evolve in different ways, I classified the morphologies of the sources in these two sub-samples. The result of this classification was published in Wang & Kaiser (2008). The details of the classification work will be described in the following subsection, and the overall data are listed in Appendix 3.

2.3.1 Classification of 7C-I and 7C-II

The Very Large Array (VLA) is one of the world's biggest radio observatories and consists of 27 antennas, each of which has a diameter of 25 meters, in a Y-shaped configuration. The antennas can move along their rails in order to switch between four different configurations: A, B, C and D, with different maximum antenna separations. Longer baseline configurations give a larger field of view and smaller angular resolution, although the field of view and the angular resolution also depend on the observational frequency. The VLA usually operates in 8 radio bands: 4(74 MHz), P(320 MHz), L(1.4 GHz), C(4.8 GHz), X(8.4 GHz), U(15 GHz), K(23 GHz) and Q(45 GHz). When observing a given source, if we want to look at its large scale structure, D-array or single dish should be chosen. Meanwhile, if we want to look at its detailed structure, A or B-array could provide higher resolution. Thus, proper configuration and observational frequency should be chosen to ensure full coverage of the whole large scale structure of the source with enough resolution to identify small scale features.

All the sources in 7C-I and 7C-II sub-samples have been observed by the VLA, and their archived data can be downloaded from https://archive.nrao.edu/archive/bigquerypage.jsp. Although the VLA does not operate in the 151 MHz waveband, as I aim to check only the large scale structure of the sources, I could just choose L band or C band alternatively. However, as I discussed in the last paragraph, cautions need to be taken to ensure that the proper array configuration was chosen. I first calculate the angular size of each source from current redshift and linear size data, then select a proper configuration which provides smallest viewing angle available just covering the whole source. In this case, the selected configuration could provide both enough spacings and high resolution at the same time. The program codes of the archival files I used and their information are listed in Appendix 3.

I classified the sources of 7C-I and 7C-II into three groups. 'II' indicates FR II morphology, with edge-brightened structure and clear hotspot at the end of the jet. If there

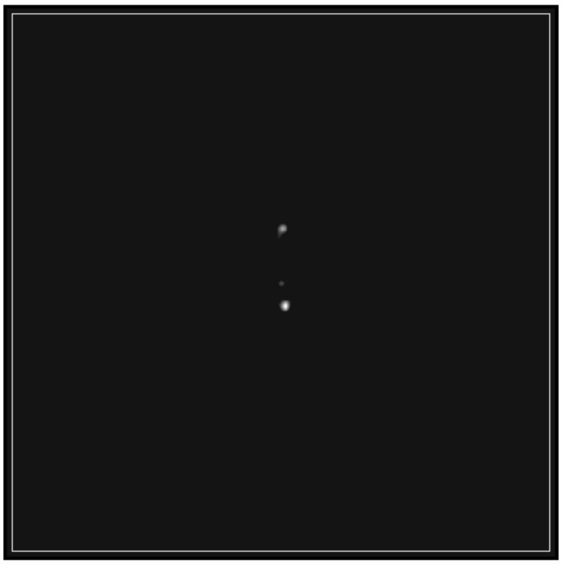

Figure 2.1: Radio Image for 5C6 5, taken from VLA observation. The picture shows a bright core and two hotspots on both sides. This source was classified as FR II source.

are two or three very bright points in an image of a source, I refer them to be the hotspot and/or core and classify the source as FR II type; 'I' indicates FR I morphology, with the laminar part dominating throughout the jet and usually have a turbulent structure. If there is only extension structure with one or not bright point in the image, I classify the source as FR I type. The classification 'c' refers to compact object, which means the source is very small and cannot be resolved even by the most sensitive array configuration available with the highest angular resolution. Some sources only show one bright point in their images from current VLA data and they all have very small angular sizes calculated from current data. They may have better images and classifications from other telescopes or surveys, but at the moment, I just classify them as compact objects. Figure 2.1 shows a typical FR II source (5C6 5), Figure 2.2 a typical FR I source (5C6 279) and Figure 2.3 a compact object (5C7 15).

2.4 The BRL sample

Best et al. (1999) define a complete sample (BRL) at an observing frequency of 408 MHz.

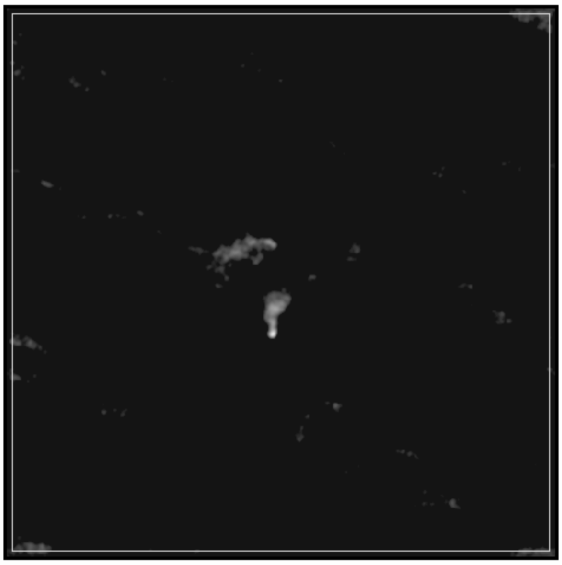

Figure 2.2: Radio morphology for 5C6 279, taken from VLA observation. The picture shows a core with tailed structure. This source was classified as FR I source.

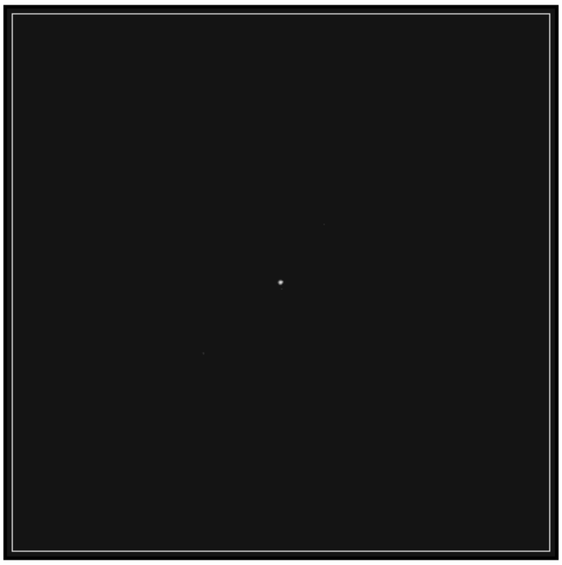

Figure 2.3: Radio morphology for 5C7 15, taken from VLA observation. There is not enough resolution, so only a point source is seen. This source was classified as a compact object.

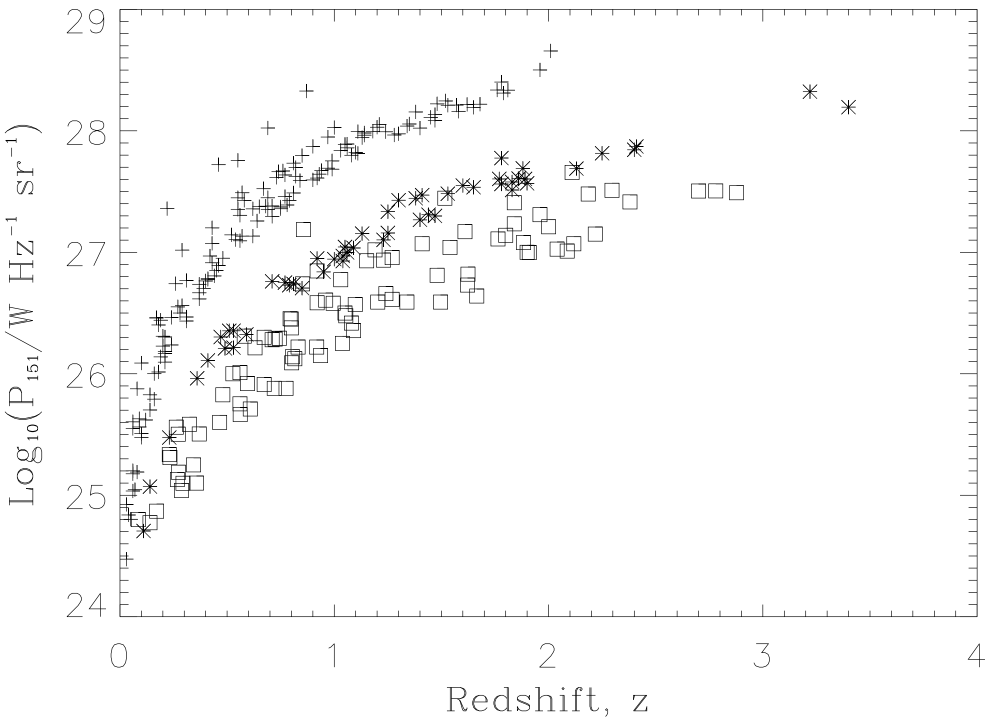

Figure 2.4: The radio luminosity-redshift plane for the 3CRR, 6CE and 7CRS samples. The different symbols identify sources from different samples: 3CRR (pluses), 6CE (asterisks) and 7CRS (squares). I convert the luminosities of 3CRR sources to that at 151 MHz based on their individual spectral index and I do not include the BRL sample in this plane as its observational frequency is far away from the other three.

The sample was selected according to the criteria $s_{408} > 5$ Jy, $-30° \leq \delta \leq 10°$, $|b| \geq 10°$, and only objects associated with extragalactic hosts were retained. Considering a typical spectral index of -0.8, this flux limit can be translated to around 10 Jy at 178 MHz, which is close to that of the 3CRR sample. Thus the BRL sample together with 3CRR sample allow us to estimate the similarity of samples drawn from the same parent population with similar selection criteria, but in different parts of the sky. The sample contains 178 sources and their properties are described in Table 3 in Best et al. (1999). The redshifts of some sources were updated by Best et al. (2000) and Best et al. (2003). I summarize the BRL sample properties that will be used in this thesis in Appendix 4.

2.5 Summary

In this chapter, I have given a brief description of the complete samples currently available at low frequency and summarized their observational properties, e.g. radio flux, redshift and angular size. Figure 2.4 present the luminosity distribution of all the sources in 3CRR, 6CE and 7CRS samples along the redshift, and the flux limits and the selection effects are clearly shown in the diagram. I have also classified the radio morphologies for 7C-I and 7C-II samples. In the next chaper, I will use these complete samples to study how radio galaxies evolve throughout cosmological time.

Chapter 3

The cosmological evolution of the FRII source population

Having constructed the complete samples and obtained their morphology classifications as described above, these samples could be used to investigate the cosmological evolution of the FR II source population. In this chapter, I will perform multi-dimensional Monte-Carlo simulations to generate large artificial samples of FR II sources based on analytical models. I will also compare these artificial samples with the 3CRR, 6CE and 7CRS samples in order to find the best fitting model describing the cosmological evolution of the FR II radio galaxy population.

The purpose of the work in this chapter is to use an existing model for the evolution of individual radio sources together with the redshift-dependent radio luminosity function to generate artificial samples containing a large number of sources. From these artificial samples I can find the best fitting parameters describing the radio sources and their environments, how the jet properties are distributed and how they evolve over cosmological time scales. This approach differs from that of Kaiser & Alexander (1999, hereafter KA99) who assume a *birth function* to describe the probability of the radio source progenitors becoming active and turning into radio sources. In this birth function approach, they simply assume that the more powerful sources are much rarer than weaker ones. More specifically, KA99 assume that radio sources with certain jet powers follow a power-law probability distribution in jet power:

$$\begin{aligned} p(Q_0)dQ_0 \quad &\propto \quad Q_0 dQ_0 \qquad \text{if } Q_{\min} < Q_0 < Q_{\max}, \\ & \quad 0 \qquad \text{if } Q_0 \geq Q_{\max} \text{ or } Q_0 \leq Q_{\min}. \end{aligned} \tag{3.1}$$

KA99 argued that the intrinsic luminosity evolution of radio sources is determined by the properties of their jets and the environments which the progenitors are located in at some cosmological epoch. I use a different approach in this chapter by directly using the RLF from W01 instead of the birth function. Thus, in my approach, the radio luminosity function is guaranteed to find the right number counts for sources with different luminosities at different redshift, and it is the size distribution and its evolution that ultimately constrain the model parameters.

Blundell & Rawlings (1999) also investigated the trends of radio galaxy properties with redshift. The main difference between their work and mine is that they use BRW model to describe the evolution of individual radio source while I am more concentrating on KDA model in this paper. BRW model differs from KDA model a lot and leads to steeper tracks in the P-D diagram. The main differences between the two models will be discussed later in Section 3.7. They also assume a power-law distributed birth function to investigate the distribution of the whole population. Barai & Wiita (2006, hereafter BW06) and Barai & Wiita (2007, hereafter BW07) tested the same three evolutionary models for FRII sources I use here. They showed that none of them fit the observational data, but again they only took into account the birth function instead of the RLF. I will consider this point in more detail in Section 3.1 and compare my results with those of BW06 and Blundell & Rawlings (1999) in Section 3.8.

3.1 The observed radio luminosity function at 151 MHz

In order to construct my artificial samples I need to know the relative number of objects with a given radio luminosity at a given redshift. The radio luminosity function (RLF) which has been developed based on the observational samples described in the last chapter meet this requirement. The RLF, $\rho(P, z)$ is defined as the number of radio sources per unit co-moving volume and per unit logarithm to base ten of luminosity at a given redshift. Several determinations of $\rho(P, z)$ at various observing frequencies are available in the literature. To minimize the effect of the hotspot emission. I use the RLF at 151 MHz compiled by W01 on the basis of 3CRR, 6CE and 7CRS samples.

W01 model the RLF as the sum of two distinct populations that are allowed to evolve independently with redshift. The low-luminosity population, whose number density is ρ_{l}, contains a mixture of FRI-type sources and the lowest luminosity FRII-type objects. The high luminosity population, whose number density is ρ_{h}, contains only FRII-type sources. The total RLF is then $\rho(P, z) = \rho_{\mathrm{l}} + \rho_{\mathrm{h}}$.

The low-luminosity population is modelled as a Schechter function,

$$\rho_l = f_{\mathrm{l}}(z)\rho_{\mathrm{l}0}\left(\frac{P}{P_{\mathrm{l}\bigstar}}\right)^{-\alpha_{\mathrm{l}}} \exp\left(\frac{-P}{P_{\mathrm{l}\bigstar}}\right), \tag{3.2}$$

where $\rho_{\mathrm{l}0}$ is a normalization term. At luminosities P below the break luminosity, $P_{\mathrm{l}\bigstar}$, the RLF approximates a power-law with slope $-\alpha_{\mathrm{l}}$. The low-luminosity population decreases exponentially above $P_{\mathrm{l}\bigstar}$. The normalization of ρ_{l} is taken to evolve with redshift through

$$f_{\mathrm{l}}(z) = (1+z)^{k_{\mathrm{l}}} \tag{3.3}$$

up to a maximum redshift $z_{\mathrm{l}0}$ beyond which f_{l} remains constant. Here, I use model C of W01, which gives the best fitting result to the observations, and so I adopt $\log \rho_{\mathrm{l}0} = -7.523$, $\alpha_{\mathrm{l}} = 0.586$, $\log P_{\mathrm{l}\bigstar} = 26.48$, $k_{\mathrm{l}} = 3.48$ and $z_{\mathrm{l}0} = 0.710$.

The high-luminosity population is parameterized in a similar way as

$$\rho_{\mathrm{h}} = f_{\mathrm{h}}(z)\rho_{\mathrm{h}0}\left(\frac{P}{P_{\mathrm{h}\bigstar}}\right)^{-\alpha_{\mathrm{h}}} \exp\left(\frac{-P_{\mathrm{h}\bigstar}}{P}\right), \tag{3.4}$$

where the exponential cut-off is now located below the break luminosity, $P_{\mathrm{h}\bigstar}$, and the power-law with slope $-\alpha_{\mathrm{h}}$ extends above $P_{\mathrm{h}\bigstar}$. The number density of sources in the high-luminosity population is modelled as rising up to $z = z_{\mathrm{h}0}$ and then decreasing at higher redshifts as

$$\begin{aligned} f_{\mathrm{h}} &= \exp\left[-\frac{1}{2}\left(\frac{z - z_{\mathrm{h}0}}{z_{\mathrm{h}1}}\right)^2\right] \text{ for } z < z_{\mathrm{h}0} \\ f_{\mathrm{h}} &= \exp\left[-\frac{1}{2}\left(\frac{z - z_{\mathrm{h}0}}{z_{\mathrm{h}2}}\right)^2\right] \text{ for } z \geq z_{\mathrm{h}0}. \end{aligned} \tag{3.5}$$

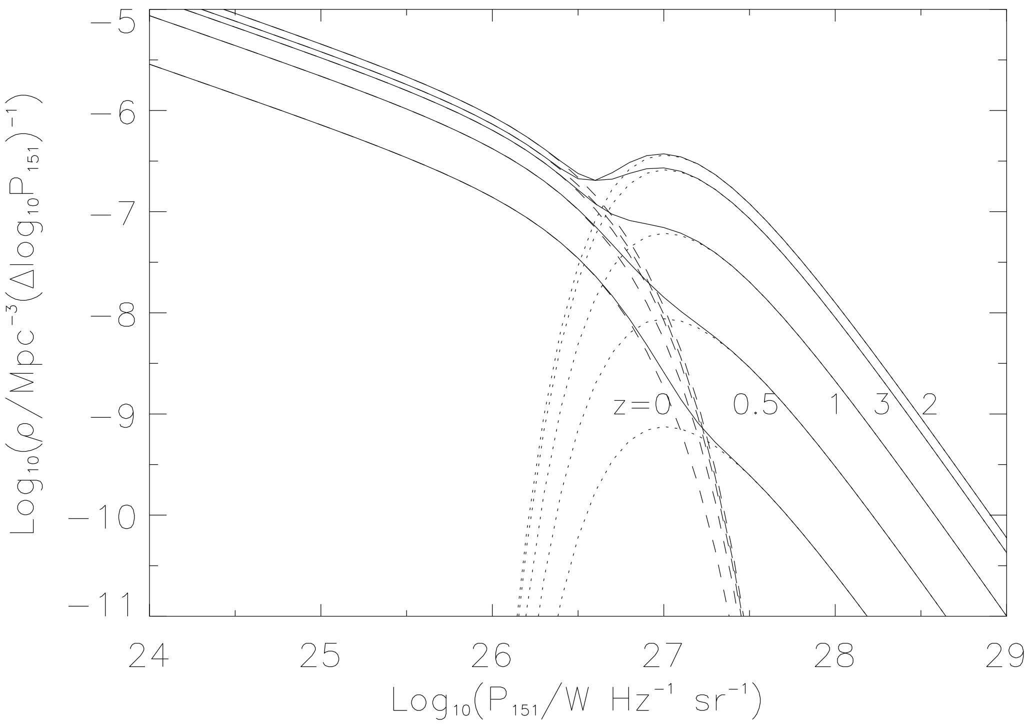

Figure 3.1: The adopted radio luminosity function corresponding to model C of W01 for $\Omega_M = 0.3$, $\Omega_\Lambda = 0.7$ and $\Omega_k = 0$. Dashed and dotted lines show the low-luminosity and high-luminosity population respectively. The solid lines show the sum of both components.

The relevant constants introduced by W01 are $\log \rho_{\rm h0} = -6.757$, $\alpha_{\rm h} = 2.42$, $\log P_{\rm h\star} = 27.39$, $z_{\rm h0} = 2.03$, $z_{\rm h1} = 0.568$ and $z_{\rm h2} = 0.956$.

In this chapter I only model sources of type FRII. However, W01 do not distinguish between the FR classes in their determination of the RLF, and while $\rho_{\rm h}$ contains only FRII-type objects, the exact composition of $\rho_{\rm l}$ in terms of FR class is not known. Here, I simply assume that 40% of the sources contributing to the low luminosity part of the RLF are of type FRII. I find below that this assumption allows for a good fit of the properties of my artificial samples to those of the observed samples. However, the fraction of FRII-type sources in $\rho_{\rm l}$ may be a function of redshift and/or luminosity. In fact, in Section 8.4.2 below I show that the observed sample with the lowest flux limit I use in this paper, the 7CRS sample, is more easily modelled with an evolving FR II fraction. The birth functions used by BRW, BW06 and BW07 simply set a cutoff at low-power end, but the distinction between FR I and FR II sources is more due to their luminosity. Thus the RLF approach may include more proper FR IIs in the final artificial samples.

W01 compute the RLF for a cosmological model with $H_0 = 50\,\mathrm{km\,s^{-1}\,Mpc^{-1}}$, $\Omega_\mathrm{M} = 0$, $\Omega_\Lambda = 0$ and $\Omega_\mathrm{k} = 1$. I adopt the cosmological parameters consistent with the WMAP results, $H_0 = 71\,\mathrm{km\,s^{-1}\,Mpc^{-1}}$, $\Omega_\mathrm{M} = 0.3$, $\Omega_\Lambda = 0.7$ and $\Omega_\mathrm{k} = 0$. Hence I need to convert the RLF, ρ, to the correct cosmological model, using the relation (Peacock, 1985):

$$\rho_1(P_1, z)\frac{\mathrm{d}V_1}{\mathrm{d}z} = \rho_2(P_2, z)\frac{\mathrm{d}V_2}{\mathrm{d}z}, \tag{3.6}$$

where P is the luminosity derived for a measured flux and redshift z in a specific cosmological model, while V is the comoving volume. The indices here refer to the two different cosmological models.

The comoving distance in a given cosmological model is (e.g. Hogg, 1999)

$$D_M(z) = \frac{c}{H_0}\int_0^z \frac{\mathrm{d}z'}{\sqrt{\Omega_\mathrm{M}(1+z')^3 + \Omega_\mathrm{k}(1+z')^2 + \Omega_\Lambda}}. \tag{3.7}$$

The luminosity distance is given by $D_L = (1+z)D_M$, so the measured flux of a source at redshift z corresponds to different luminosities in different cosmological models, which are related by

$$P_1 D_{M,1}^{-2} = P_2 D_{M,2}^{-2}. \tag{3.8}$$

The comoving volume of a spherical shell at D_M is:

$$\mathrm{d}V = 4\pi D_M^2\,\mathrm{d}D_M. \tag{3.9}$$

I use the above relations to translate the RLF of W01 into my adopted cosmological model. The resulting RLF is shown in Figure 3.1.

3.2 The P-D-z data cube

I use the RLF described above to constrain the number of sources in my artificial samples with a given radio luminosity at a specified redshift. Therefore, by construction, my artificial samples agree with the two-dimensional distribution of radio luminosities, P, and redshifts, z, i.e. they correctly reproduce the RLF, or equivalently, the p-z diagram, of the observed complete samples. However, we also know the measured linear size of the radio lobe for each source in each observational sample. The full data set therefore consists of a three-dimensional data cube whose axes are radio luminosity, P, linear size, D, and redshift, z. Thus I can evaluate the goodness-of-fit for any artificial samples by comparing them to the source distribution in the full P-D-z data cube.

BRW, BW06 and BW07 also considered the radio spectral index as a fourth parameter. They found that the observed distribution of the spectral index could not be fitted very well. They use the same models for the evolution of radio sources that I employ here in this chapter. These models significantly restrict the possible range of the spectral index, and this effect naturally explains the difficulties encountered by BW06 and BW07. Here I do not attempt to reproduce the observed distribution of spectral indices, as this would either result in the same problem or require the introduction of an additional model parameter. I will return to this point below.

3.3 Models for the dynamic and emission evolution of individual FR II sources

The large-scale structure of FRII-type sources is inflated by powerful jets accelerated in the vicinity of the supermassive black holes at the centre of the AGN inside the host galaxies. The jets end in strong shocks which accelerate electrons to relativistic velocities and may increase the strength of the magnetic field. The magnetized plasma passing through the jet shock subsequently inflates the lobe or cocoon. This basic dynamical picture was first proposed by Scheuer (1974) and Blandford & Rees (1974).

Falle (1991) and KA97 assumed the jet is in pressure-equilibrium with its own lobe, then showed that the expansion of the lobe and the bow shock in front of it is self-similar. A sketch of the model is shown in Figure 1.4. Here I use the model of KA97 to describe the dynamics of the lobes. I summarize the most important features of the model below.

The growth of the jet length is essentially determined by a balance of the ram pressures of the jet material and of the medium surrounding the host galaxy, which is pushed aside by the jet. X-ray observations of the hot gas in the vicinity of elliptical galaxies, in galaxy groups and in galaxy clusters find density distributions that are well fitted by power-law models (e.g. Fukazawa et al., 2004). In the KA97 model the density distribution that are outside the core radius a_0 is approximated by a power-law:

$$\rho_x = \rho_0 \left(\frac{d}{a_0} \right)^{-\alpha}, \tag{3.10}$$

where d is the radial distance from the AGN at the centre of the density distribution and ρ_0 is the density at the core radius. The exponent α is constrained by observations to the range $0 < \alpha \leq 2$.

I assume that the gas in the vicinity of the AGN has a non-relativistic equation of state, $\Gamma_x = 5/3$, while the lobes only contain magnetic fields and relativistic particles, $\Gamma_c = 4/3$. For a jet providing a constant power Q_0 for a time t and inflating a lobe with an aspect ratio R_{T}, the lobe length, D, and the pressure inside the lobe, p_{c} are given by:

$$\begin{aligned} D &= c_1 \left(\frac{Q_0}{\rho_0 a_0^{\alpha}} \right)^{\frac{1}{5-\alpha}} t^{\frac{3}{5-\alpha}}, \\ p_{\mathrm{c}} &= \frac{27 c_1^{2-\alpha}}{16(5-\alpha)^2} R_{\mathrm{T}}^{-2} (\rho_0 a_0^{\alpha})^{\frac{3}{5-\alpha}} t^{\frac{-4-\alpha}{5-\alpha}} Q_0^{\frac{2-\alpha}{5-\alpha}}, \end{aligned} \tag{3.11}$$

where

$$c_1 = \left(\frac{64 R_{\mathrm{T}}^4 (5-\alpha)^3}{81\pi(8-\alpha+3R_{\mathrm{T}}^2)} \right)^{\frac{1}{5-\alpha}}. \tag{3.12}$$

Note that the model of the source dynamics only depends on the combination $\rho_0 a_0^{\alpha}$, but not on ρ_0 and a_0 separately. For convenience, I therefore introduce the parameter $\Lambda = \rho_0 a_0^{\alpha}$. In this thesis, I initially assume $\alpha = 2$, as this considerably simplifies the equations. I will discuss the effect of relaxing this assumption in Section 3.7.4.1.

KDA extended the dynamics model of KA97 to include the calculation of the radio emission expected from the lobe. To this end, they divided the radio lobe into small volume elements δV. Each δV is injected into the lobe at a certain time t_i. The overall dynamics of the lobe, specifically the evolution of p_{c} over a short time interval δ_{t_i}, were considered in KA97. The volume elements contains relativistic electrons, which are initially accelerated at time t_i. The energy distribution of the relativistic electrons is assumed to initially

follow a power-law with exponent p between a low and high energy cut-off represented by the Lorentz factors of the least and most energetic electrons, $\gamma_{\rm min}$ and $\gamma_{\rm max}$, respectively.
:

$$n(\gamma_i, t_i)d\gamma_i = n_0 \gamma_i^{-p} d\gamma_i. \tag{3.13}$$

Observations suggest that the value of the exponent p should fall in the range between 2 and 3 (Alexander & Leahy, 1987). Meanwhile, for many radio sources, the value of p is actually a function of wavelength, mainly because the spectra are curved as different physics dominate the radiations respectively at different wavebands. The value of p is also related to the acceleration process happening in the hotspot, which is not well understood at the moment. Thus, in order to keep the equations and the model simple, I choose $p = 2$. Please note that this value will over predict the number of FR IIs at high redshift (BRW). The exact value of $\gamma_{\rm max}$ does not significantly influence the model results as long as it is large, but the value of $\gamma_{\rm min}$ does affect the model result. Thus in this thesis, I will follow KDA's assumption of $\gamma_{\rm min} = 1$ and $\gamma_{\rm max} = 10^5$. The details of all relevant model equations can be found in the KA97 and KDA papers, while a summary of them can also be found in Kaiser & Best (2007, hereafter KB07).

The model takes into account the energy losses of the relativistic electrons due to the adiabatic expansion of the lobe, synchrotron radiation and inverse Compton losses from scattering of the cosmic microwave background radiation (CMBR). The rate of energy losses is represented by the derivative of the Lorentz factor:

$$\frac{d\gamma}{dt} = -\frac{a_1}{3}\frac{\gamma}{t} - \frac{4}{3}\frac{\delta_T}{m_e c}\gamma^2 (u_B + u_C), \tag{3.14}$$

where a_1 is a constant representing the expanding rate of the jet volume, δ_T is the Thompson cross-section, m_e is the electron mass, u_B is the energy density of the magnetic field in the lobe and u_C is the energy density of the CMBR. By summing up the contribution from all volume elements within the lobe and integrating over the injection times, t_i, I can calculate the total radio emission from the lobe as a function of jet age, t:

$$P_\nu = \int_{t_{min}}^{t} \frac{\delta_T c}{14\pi\nu} Q_0 n_0 (2R_T)^{0.5} \gamma \left(\frac{t}{t_i}\right)^{-2.5} dt_i. \tag{3.15}$$

The model above determines the spectral index equal to $(p-1)/2$, so $2 \leq p \leq 3$ limits the range of spectral indices predicted by the model to the narrow range from -0.5

to -1. For young sources, adiabatic losses are most important, while for old objects inverse Compton losses dominate; both processes lead to a steep spectrum. For 'middle-age' sources between these extremes, the relativistic electrons are not much affected by radiative energy losses, and so the spectrum flattens (KB07). In objects with observed spectral indices not conforming to this pattern a different acceleration regime may be applicable and lead to a different value of p. More specifically, my choice of a fixed value for p in this thesis implies that I also fix the spectral indices and cannot expect the spectral index distribution of my artificial source populations to agree with that of the observed complete samples. Meanwhile, different spectral index will also affect the selection effect of the observed complete samples, more specifically, steeper spectral index may cause more sources lost at high redshift (BRW99). As a result, the flux limit I chose during my simulation process later could also be affect by a fixed p. However, the introduction of an unknown distribution for p into the model would considerably complicate the analysis of my results and introduce another model parameter. Thus, I still concentrate on a fixed p here.

The combined model of KA97 and KDA in the form specified there depends on parameters of R_{T}, Λ and Q_0. For a certain radio source with given z and t, a complete set of these parameters fully determines the linear size of the lobes, D, and their radio luminosity, P. Therefore I can take the observed distribution of sources in the P-D-z space to constrain the underlying distribution of the density of their environments described as Λ, their age t and their jet power Q_0. In the following, I explain the practical implementation of this process, as well as my assumption for the distribution of lobe aspect ratios, R_{T}.

3.4 Monte-Carlo simulation

The RLF, $\rho(P, z)$, gives the comoving number density of radio sources at a cosmological redshift z with a given radio luminosity P. The number of sources within the ranges z to $z + \mathrm{d}z$ and logP to logP + dlogP is given by $n = \rho(P, z)\,\mathrm{d}\log P\,\mathrm{d}V$, where $\mathrm{d}V$ is the comoving volume sampled between z and $z + \mathrm{d}z$. The relevant formulae are presented in Section 3.1. I consider redshifts from $z = 4$ to $z = 0$ with a step size of $\mathrm{d}z = 0.004$ and

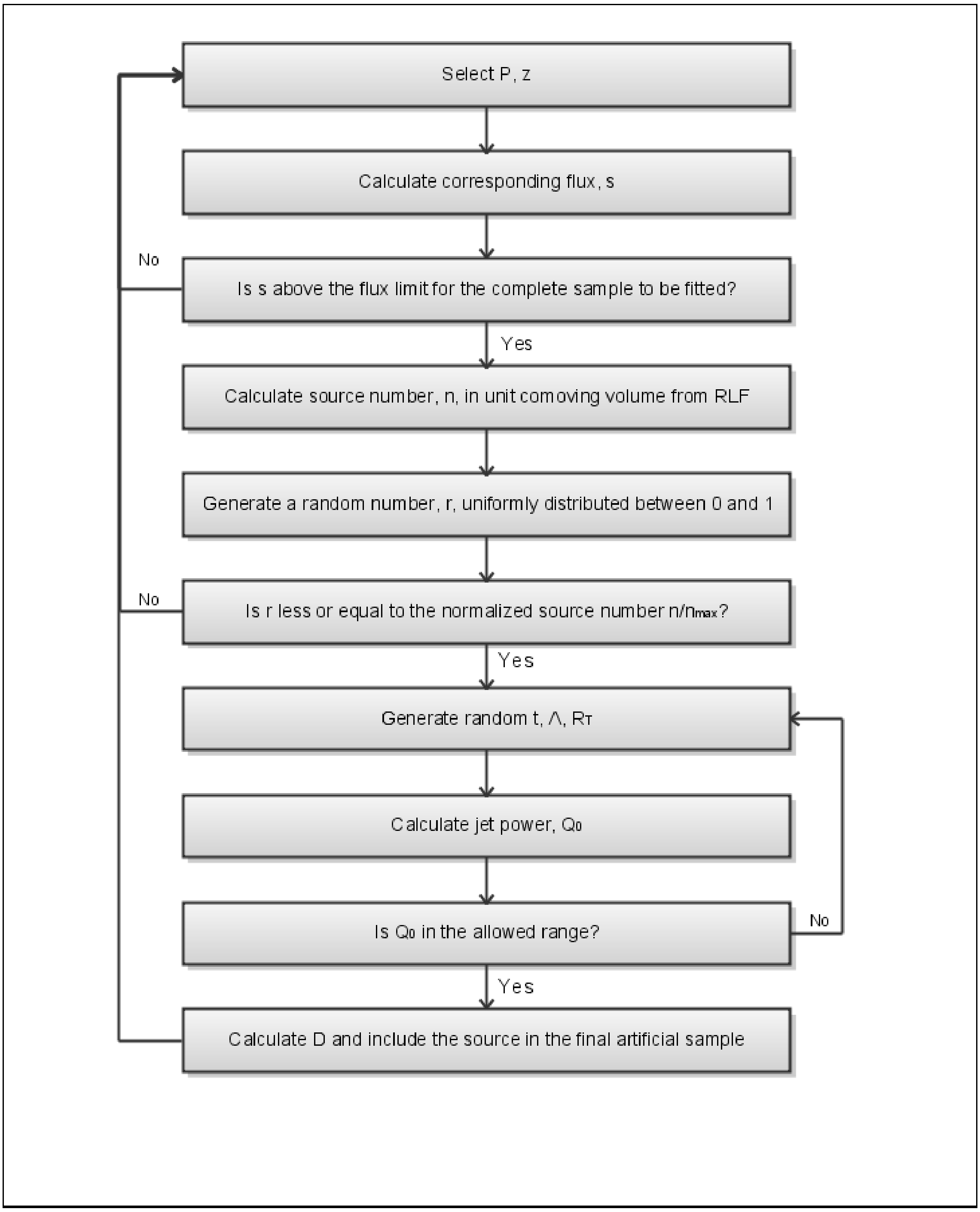

Figure 3.2: The flow diagram of the Monte-Carlo process I use in this paper.

radio luminosities at an observing frequency of 151 MHz from $P = 10^{24.5}\,\mathrm{W\,Hz^{-1}\,sr^{-1}}$ to $P = 10^{29}\ \mathrm{W\,Hz^{-1}\,sr^{-1}}$ in steps of $\mathrm{d}\log P = 0.01$. These ranges cover the entire source population in all three observed samples I consider. I only calculate n for combinations of P and z for which the corresponding observable flux exceeds the flux limit of the observed complete sample I use to compare my artificial sample with.

After calculating n at all given values of P and z defined by the ranges and step sizes described in last paragragh, I normalize it such that its maximum is equal to unity. I can then interpret $n\,(P, z)$ as the distribution of the probability to find a source in an artificial sample with a given combination of redshift and radio luminosity. To construct my artificial sample, I then iterate through all allowed combinations of P and z and generate a random number, r, uniformly distributed between 0 and 1. If $r \leq n\,(P, z)$ for the chosen P and z, then a source with this radio luminosity and redshift is included in the artificial sample. I can increase the sample size by repeating the same process a fixed number of times at all allowed combinations of P and z.

Once a source with a given combination of radio luminosity and redshift is included in the artificial sample, I need to calculate the linear size of its lobe to determine its position in the P-D-z data cube for comparison with the observations. For this, I need the aspect ratio of the lobe, R_{T}, the age of the source, t, and the parameter describing the external density distribution, Λ. Fixing the values of these three parameters uniquely determines the length of the lobes, D, and the jet power, Q_0. In other words, fixing the values of three parameters uniquely determines the values of the remaining two. For each source in the artificial sample, I choose random values for R_{T}, t and Λ from distributions of these parameters discussed below.

It is difficult to accurately determine the aspect ratio of the lobe of a radio source. The lobe should ideally be detected all the way back to the central AGN, which suggests the use of a low observing frequency to minimize the effects of radiative energy losses. At the same time I need sufficient angular resolution to resolve the lobe perpendicular to the jet axis. This is best achieved at high observing frequencies. In practice a balance must be found between these requirements, and so an observationally determined distribution of R_{T} is not available in the literature. For simplicity I choose a uniform distribution across the range $1.3 \leq R_{\rm T} \leq 6$, where the limits are motivated by observed values (Leahy & Williams, 1984). Below I discuss the minor effects on my results of changing this distribution.

If I assume that all radio sources have a common maximum lifetime $t_{\rm max}$, then the distribution of their ages is given by a uniform distribution extending from $t = 0$ to $t = t_{\rm max}$. Spectral ages of some objects reach a few 10^8 years (e.g. Alexander & Leahy, 1987), but recently Bird et al. (2008) found an average age of around 10^7 years for a sample of FRII-type objects located in low redshift galaxy groups, suggesting a maximum lifetime of a few 10^7 years. The maximum lifetime depends on the availability of fuel for the jet-producing AGN, and it would therefore be surprising if $t_{\rm max}$ was the same for all sources. However, the spread around the average age found by Bird et al. (2008) is comparatively small, so, for simplicity, I assume that $t_{\rm max}$ is indeed the same for all sources at a given redshift. I will show below that $t_{\rm max}$ defined in this way may be a function of redshift.

The parameter Λ describing the density distribution in the environment of a source can, in principle, be determined from X-ray observations. FRII-type objects seem to be preferentially located in isolated galaxies or galaxy groups. With $\alpha = 2$, I expect Λ between $10^{17}\,{\rm kg\,m^{-1}}$ and $10^{18}\,{\rm kg\,m^{-1}}$ for individual galaxies (Fukazawa et al., 2004). For group environments, Jetha et al. (2007) find values for Λ in the range $2 \times 10^{18}\,{\rm kg\,m^{-1}}$ and $4 \times 10^{19}\,{\rm kg\,m^{-1}}$. Note that all these determinations predict somewhat high values for Λ, because I am using $\alpha = 2$ at the moment. For $\alpha = 1.5$, the values of Λ are more consistent with the values given by Fukazawa et al. (2004) and Jetha et al. (2007). The gas haloes of many galaxies and galaxy groups show flatter slopes, implying smaller values of Λ. Again, there is no determination of the complete distribution of Λ for the environments of radio sources available in the literature. Hence I draw random values for Λ from a uniform distribution extending from $\Lambda = 0$ to $\Lambda = \Lambda_{\rm max}$, where the maximum value is to be determined from the models and may be a function of redshift. Random Λ with a different distribution, i.e. Gaussian distribution, are also tested later in this chapter.

For every allowed combination of the radio luminosity and the redshift plus the randomly chosen values for $R_{\rm T}$, t and Λ, I can now proceed to calculate a linear size, D, of the lobe and jet power, Q_0, for each source to be included in the artificial sample. The parameter distributions used here allow for a wide range of possible values for Q_0, but not all values for Q_0 are acceptable. Sources with weak jets, i.e. small jet powers, will develop turbulent, rather than laminar jets, and this will result in FRI-type lobes. Rawlings & Saunders (1991) suggest that the transition between the FR types occurs close to $Q_0 = 10^{37}$ W based on radio observations of lobes and optical line emission from the AGN itself. A similar lower limit for the jet power of sources with an FRII-type morphology was derived by KB07 using the model I employ here as well. An upper limit on Q_0 may be given by the Eddington luminosity of the most massive black holes. In this thesis I require that $10^{37}\,\mathrm{W} \leq Q_0 \leq 5 \times 10^{40}\,\mathrm{W}$. Model parameters that imply a jet power outside this range are rejected. For rejected sources I generate new sets of model parameters, R_{T}, t and Λ, in the way described above until an acceptable value for Q_0 is found.

Note here that the mathematical form of the distributions for the model parameters only indirectly influences the distributions of these parameters in the final artificial sample. Combinations of model parameters must lead to acceptable results in the sense that not only must the resulting source have the correct radio luminosity and redshift, its jet power must also fall within the specified range. The resulting parameter distributions will in general not follow the distributions they are originally drawn from, because many possible parameter combinations will be rejected as described above. In practice, this means that the choice of uniform distributions over other mathematical functions only weakly influences the final distributions of the model parameters. I will discuss and demonstrate this point in more detail in Section 3.6.3.

Once an acceptable combination of model parameters is found, I can calculate the corresponding length of the lobes, D. This is the physical length of the lobe, and, in order to compare to the observed complete samples, I need to take into account that the lobes may be projected, since their main axis is oriented at an angle θ to my line of sight. The observed lobe length is therefore given as $D_{\mathrm{ob}} = D \sin\theta$, where the random orientation θ is distributed as $\sin\theta\,\mathrm{d}\theta$ between $\theta = 0$ and $\theta = \pi/2$. Before including a source in the P-D-z data cube of my artificial sample, I choose a random orientation angle and project the lobes into the plane of the sky. For simplicity, hereafter I denote the D_{ob} as just D.

The process of generating my artificial samples described above is summarized in the flow diagram in Figure 3.2. My artificial samples contain of order 6000 sources. This is a much larger number than is contained in the observed samples. However, I found that such a large number is required to arrive at reasonably smooth source distributions in the P-D-z data cubes, and also to minimize the influence of the initial model parameter distributions on the final distributions.

3.5 Kolmogorov-Smirnov test

My artificial samples define a source distribution within the P-D-z data cube. I then use a three-dimensional version of the Kolmogorov-Smirnov (KS) test to compare my model results with the observations.

The classical one-dimensional Kolmogorov-Smirnov test makes use of the probability distribution of the quantity D_{KS}, defined as the largest absolute difference between the one-dimensional cumulative distributions of two samples, where one or both samples can be continuous or discrete. Peacock (1983) extends this idea to a two-dimensional test by making use of the maximum absolute difference between two distributions, when all four possible ways to cumulate data following the directions of the coordinate axes are considered. For the comparison of a sample with n members with a continuous distribution Peacock's test requires that the cumulative distributions should be calculated in all $4n^2$ quadrants of the plane defined by,

$$\begin{aligned} (x < X_i, y < Y_j),\ (x < X_i, y > Y_j),\ (x > X_i, y < Y_j), \\ (x > X_i, y > Y_j), \end{aligned} \tag{3.16}$$

for all possible combinations of the indexes i and j from 1 to n. Here, X_i and Y_i denote the coordinates of individual members of the discrete sample.

Fasano & Franceschini (1987) show that it is sufficient to consider only the four quadrants defined by each individual data point in the discrete sample, i.e. $i = j$. This reduces the total number of quadrants in which the distributions are accumulated to $4n$. Furthermore, the extension of this methodology to three dimensions is straightforward, provided all eight quadrants defined by each individual data point are considered in deriving the largest difference, $D_{\rm KS}$, of the cumulative distributions.

Using the three-dimensional KS test, I can now compare the fit of various artificial source distributions within the P-D-z data cube arising from different models with that of the observed samples. However, the method does not assign a formal goodness-of-fit measure, because the statistic distribution of $D_{\rm KS}$ in the three-dimensional KS test is not known in general. Also, the selection criteria for the observed samples, in particular their flux limit, prevent the population of certain parts of the P-D-z cube. In order to assess which model provides an acceptable fit to the observations, I separately construct the statistics of $D_{\rm KS}$ for each model calculation. For this I generate a large number of sources for a specific model as detailed above. I then repeatedly draw random subsamples from these model sources with a total source number equal to that of the observed comparison sample. I calculate the total difference $D_{\rm KS}$ of the cumulative distributions of the subsamples and the parent model sample. In this way I build up the probability distribution of $D_{\rm KS}$ for this particular model. Based on this statistic I assign a probability $P(D_{\rm KS,obs})$ to the value $D_{\rm KS,obs}$ calculated for the observed sample. $P(D_{\rm KS,obs})$ is defined as the fraction of test samples having larger $D_{\rm KS}$ than the real sample. It is therefore the probability that a fit as poor as that to the real data should be seen under the hypothesis that the model is correct. However, this technique can only guide me in the selection of models. It cannot identify the statistically most likely model, as the distribution of $D_{\rm KS}$ will be different for each observational sample. In Table 3.1, I show the distribution of $P(D_{\rm KS})$ for each sample.

3.6 Results

I now have all the ingredients to generate my artificial samples and compare them to the observed samples. In doing so, my general approach is to start with the simplest models and only modify these as necessary to achieve a better agreement with the observations. It is not feasible to show the full three-dimensional source distributions used in the comparisons. In order to present my results, I therefore plot two-dimensional projections of the

$P(D_{\rm KS})$	$D_{\rm KS}$ for 3CRR	$D_{\rm KS}$ for 6CE	$D_{\rm KS}$ for 7CRS
0.1%	0.172	0.277	0.216
1%	0.152	0.240	0.186
10%	0.122	0.191	0.152
20%	0.112	0.173	0.137
30%	0.103	0.161	0.127
40%	0.098	0.151	0.120
50%	0.092	0.142	0.113
60%	0.087	0.133	0.107
70%	0.082	0.125	0.100
80%	0.076	0.116	0.094
90%	0.070	0.104	0.086
99%	0.057	0.084	0.069

Table 3.1: The statistic of KS test for different samples.

P-D-z cube. Sources in observed samples are presented as individual crosses, while the large numbers of sources in the artificial samples are shown as density contours in these plots. The contours enclose areas of 1%, 10%, 40% and 80% of the maximum density in each plot.

Note that in the following I always show the radio luminosity density of sources in the 3CRR sample and associated artificial samples at 178 MHz rather than 151 MHz. While I use the RLF at 151 MHz in my models to calculate relative source numbers as detailed above, I calculate the luminosity for my artificial sources at 178 MHz and use the appropriate flux limit for this frequency when comparing with the 3CRR sample.

3.6.1 Model A

The simplest model I can build within the framework described above has uniform distributions with fixed upper limits for the source age and the density parameter. I assume a fixed $t_{\rm max} = 2.5 \times 10^7$ years and investigate a range of possible $\Lambda_{\rm max}$. None of the $\Lambda_{\rm max}$ tried leads to a probability significantly different from zero as measured by the KS test

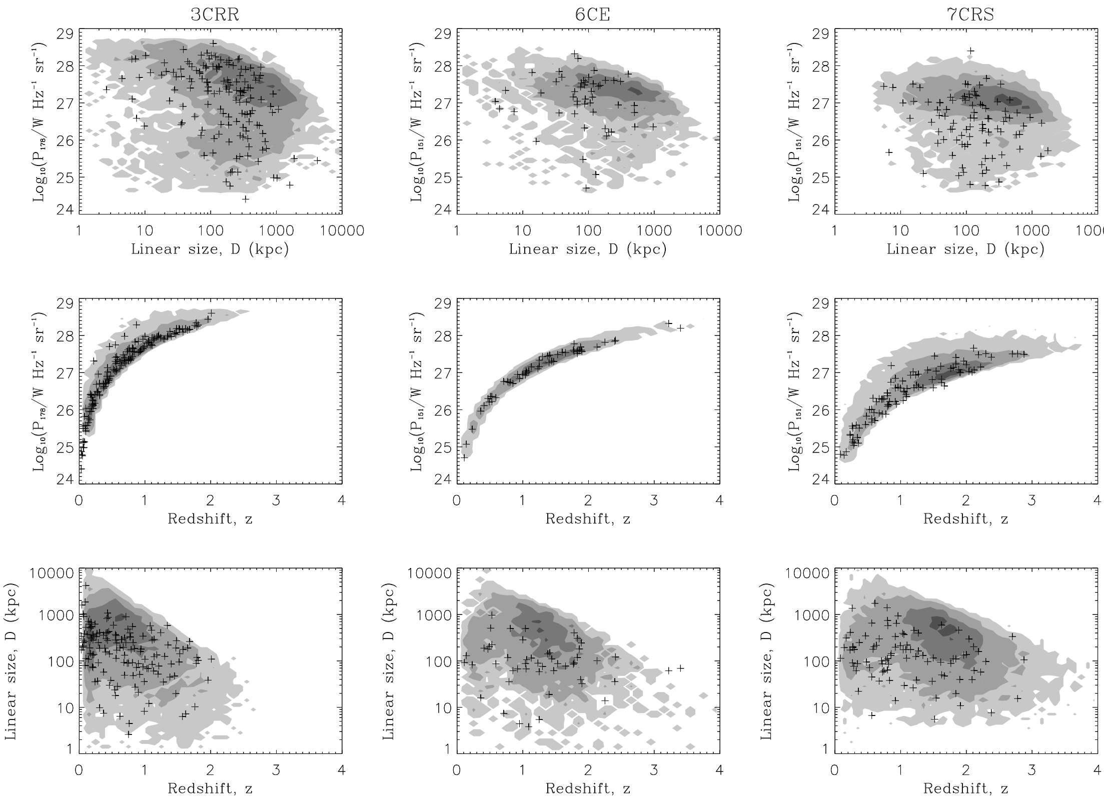

Figure 3.3: Projections of the P-D-z data cube for observed samples with source density contours from Model A. The parameters I use here are $t_{\rm max} = 2.5 \times 10^7\,{\rm yr}$ and $\Lambda_{\rm max} = 1 \times 10^{18}\,{\rm kg\,m^{-1}}$. Crosses indicate FRII sources in the observed samples. Gray scales indicate the number density of the artificial samples.

$(P(D_{\rm KS}) < 0.1\%)$. Varying $t_{\rm max}$ instead of $\Lambda_{\rm max}$ leads to the same result.

As an example, in Figure 3.3 I show a comparison of the resulting artificial samples with $\Lambda_{\rm max} = 1 \times 10^{18}\,{\rm kg\,m^{-1}}$ with the observed samples. Clearly high luminosity sources located at high redshifts are too large in my artificial samples compared to the observed sources. The sources in the artificial samples show a trend of increasing size with increasing luminosity until the trend is reversed at the highest luminosities. The radio luminosity of a source in the KDA model is mainly governed by the jet power, Q_0. However, a larger value of Q_0 also implies faster growth of the lobes and, all other parameters being equal on average, it is not surprising that I find a trend of radio luminosity with size in my artificial sample.

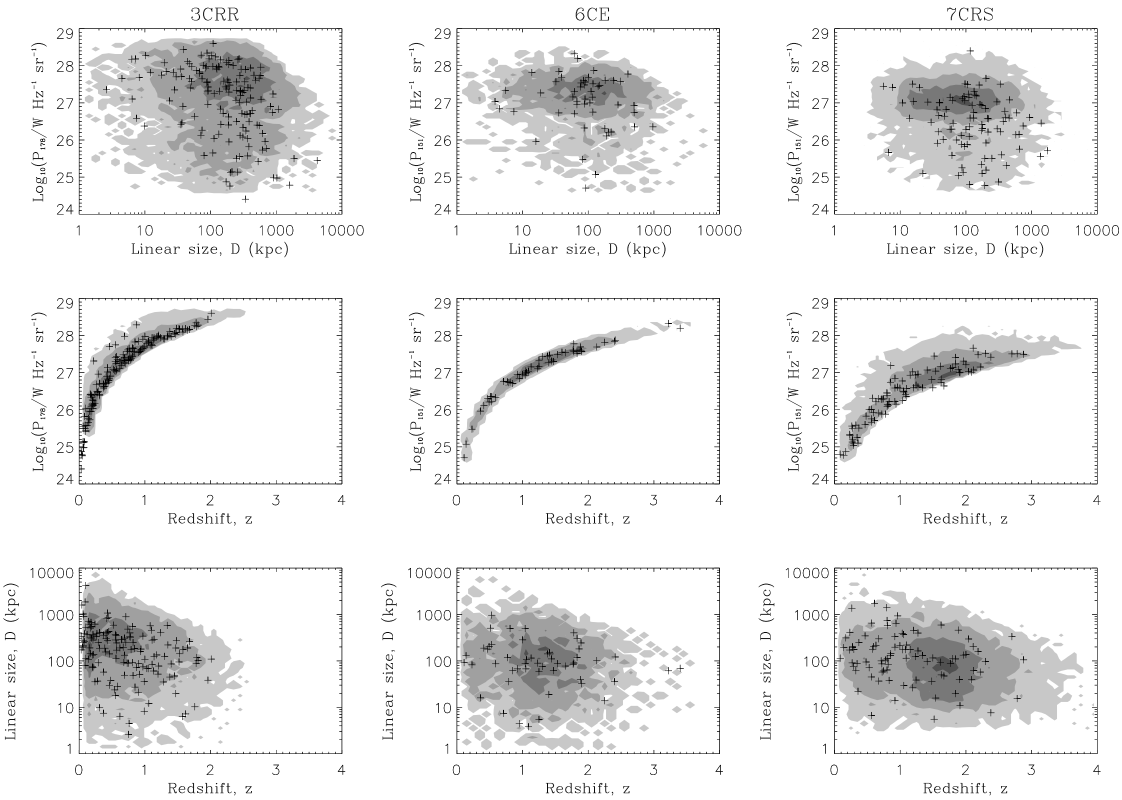

Figure 3.4: Projections of the P-D-z data cube comparing observed samples with the source density contours resulting from Model B. The parameters I use here are $t_{\max} = 5 \times 10^7\,\mathrm{yr}$, $\Lambda_{\max}(0) = 3.7 \times 10^{18}\,\mathrm{kg\,m^{-1}}$ and $\psi = 5.8$. Crosses indicate FRII sources in the observed samples. Gray scales indicate the number density of the artificial samples.

The reversal of this trend at the highest luminosities has been noted by many authors (e.g. Oort et al., 1987; Neeser et al., 1995) for observed samples. In the artificial samples it is caused by the flux limits of the samples in combination with the decreasing luminosity of older, and therefore larger, sources. Clearly the evolutionary model used here predicts that this effect alone is not sufficient to explain the observed trend reversal and some other effects must contribute to reconcile the model with the observations (see also KA99). I will investigate such effects in the next two sections.

Modified models with a steeper luminosity evolution of individual sources do not need to invoke such additional effects (BRW and MK). However, they may be less consistent with the overall source distribution (BW06). I shall apply these models in the same way to the data as the combined models of KA97 and KDA in section 3.7.

3.6.2 Model B

In this and the following sections I investigate which additional factors may lead to a better fit of the predicted distribution of sources in the P-D-z cube with the observational data. I have shown above that in my modeling framework I need an additional effect to explain the apparent shortening of the lobes of sources with the highest radio luminosities located at the highest redshifts. In this section I introduce a redshift dependence for the upper limit of the density parameter Λ. In the following section I do the same for the upper limit of the source age distribution.

I start by fixing the maximum source age to $t_{\max} = 5\times10^7$ years and introduce a variable upper limit for the distribution of Λ such that $\Lambda_{\max}(z) = \Lambda_{\max}(0)\,(1+z)^{\psi}$. The best agreement between artificial and observed samples is achieved for 3CRR with $\Lambda_{\max}(0) = 3.7 \pm 0.2 \times 10^{18}\,\mathrm{kg\,m^{-1}}$ and $\psi = 5.9 \pm 0.2$, giving a probability that the observed sample is drawn from a population described by the model of $P(D_{\mathrm{KS}}) = 48\%$. The values for 6CE are $\Lambda_{\max}(0) = 3.8^{+0.2}_{-0.3} \times 10^{18}\,\mathrm{kg\,m^{-1}}$, $\psi = 5.8 \pm 0.2$ and $P(D_{\mathrm{KS}}) = 56\%$. The limits on the model parameters give their value where $P(D_{\mathrm{KS}})$ halves compared to its maximum. Please note that these limits are only indicative and not standard $1-\sigma$ errors. The fit of the model to the 7CRS sample is much worse, and the values for $P(D_{\mathrm{KS}})$ are very low. This is related to problems with the RLF for this sample. I will discuss this issue in Section 8.4.2. In any case, the maximum of $P(D_{\mathrm{KS}})$ for 7CRS occurs close to $\Lambda_{\max}(0) = 3.7 \times 10^{18}\,\mathrm{kg\,m^{-1}}$ and $\psi = 6$, consistent with the results for the other two samples. A model with $\Lambda_{\max}(0) = 3.7 \times 10^{18}\,\mathrm{kg\,m^{-1}}$ and $\psi = 5.8$ provides an acceptable fit to both 3CRR ($P(D_{\mathrm{KS}}) = 40\%$ and 6CE ($P(D_{\mathrm{KS}}) = 41\%$. The comparison of this model and the observed samples is shown in Figure 3.4.

The much better fit of Model B compared to Model A is explained by the considerably higher average density of the source environments at high redshifts. The density parameter Λ has only a moderate influence on the radio luminosity of a model source compared to the jet power. However, a high value of Λ efficiently reduces the expansion speed of the lobes. Hence the strong evolution of $\Lambda_{\max}$ with z in Model B ensures that sources at high redshift remain smaller for longer than their low redshift counterparts. This allows

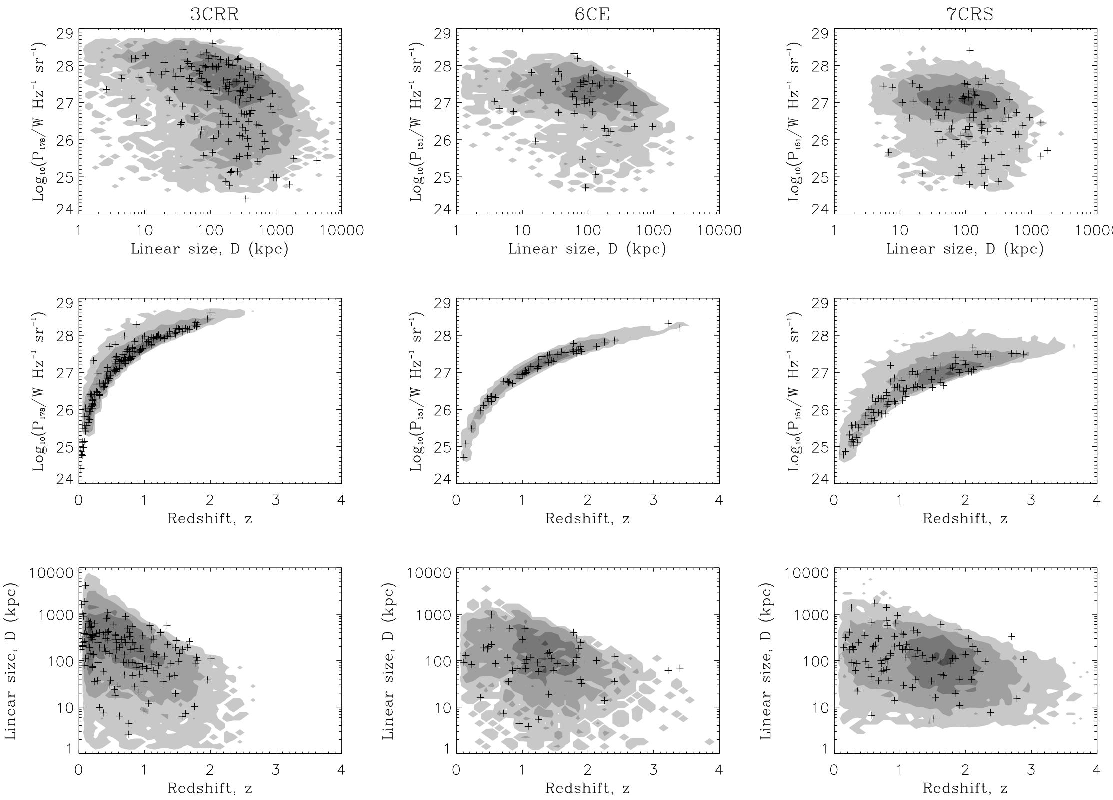

Figure 3.5: Projections of the *P*-*D*-*z* cube for the observed samples with source density contours from Model C. The parameters I use here are $t_{\rm max}(0) = 2.7 \times 10^7\,\rm yr$, $\Lambda_{\rm max} = 6.4 \times 10^{17}\,\rm kg\,m^{-1}$ and $\phi = 2.4$. Crosses indicate FRII sources in the observed samples. Gray scales indicate the number density of the artificial samples.

a better fit of the high luminosity / high redshift part of the source population.

3.6.3 Model C

Instead of invoking denser average source environments at higher redshifts to reduce the average size of the highest luminosity sources, the average lifetime of the sources could also be shorter at higher redshift, as the early universe is less stable than today. For this, I fix $\Lambda_{\rm max}(z)$ at $6.4 \times 10^{17}\,\rm kg\,m^{-1}$ for all z and introduce a variable maximum age as $t_{\rm max}(z) = t_{\rm max}(0)\,(1+z)^{-\phi}$. The best agreement is found for $t_{\rm max}(0) = 2.7^{+0.3}_{-0.2} \times 10^7\,\rm yr$ and $\phi = 2.4 \pm 0.2$ for 3CRR with $P(D_{\rm KS}) = 76\%$. The 6CE sample gives an almost identical result with $t_{\rm max}(0) = 2.7^{+0.1}_{-0.3} \times 10^7\,\rm yr$ and $\phi = 2.4 \pm 0.1$ where $P(D_{\rm KS}) = 59\%$. Again, the comparison with 7CRS does not produce good fits for the reasons I will discuss in Section 3.6.4.4, but the maximum of the probability occurs close to the parameter values for the two other samples. The maximum source age at low redshifts is reassuringly close to the value of the average source lifetime of 1.2×10^7 yr recently derived by Bird et al. (2008) for an independent sample. Figure 3.5 compares the model results with the observed data.

I assume a uniform distribution of Λ in Model C. The real distribution of Λ is unknown, and it does not have to be uniform. Instead of a uniform distribution, I therefore also considered a Gaussian distribution with a peak at $3.2 \times 10^{17}\,\mathrm{kg\,m^{-1}}$ and a width of $\sigma = 1 \times 10^{17}\,\mathrm{kg\,m^{-1}}$. The distribution is truncated so that there are no values of Λ below 0 or above $6.4 \times 10^{17}\,\mathrm{kg\,m^{-1}}$. This distribution covers the same range of Λ, but is of course different from an uniform distribution. The agreement with the same $t_{\mathrm{max}}(0)$ and ϕ are $P(D_{\mathrm{KS}}) = 77\%$ for 3CRR and $P(D_{\mathrm{KS}}) = 52\%$ for 6CE. For the extreme assumption of a fixed value of $\Lambda = 3.2 \times 10^{17}\,\mathrm{kg\,m^{-1}}$ for all sources, I can still find a comparable agreement with $P(D_{\mathrm{KS}}) = 73\%$ for 3CRR and $P(D_{\mathrm{KS}}) = 55\%$ for 6CE. Clearly, I cannot rule out these distributions compared to a uniform distribution. I will discuss this point in detail in section 3.7.

Jet age and density parameter are the two primary random input parameters in the simulation process. (The axial ratio is a random input as well, but it is less important and will be discussed in the following section.) Thus in this thesis, I only discuss the three models listed above as they are the simplest and most straightforward cases. The results show that both models B and C can provide adequate fits to the observed samples 3CRR and 6CE. Given the results detailed above, I cannot formally decide whether it is a reduced maximum lifetime or a denser environment that limits the lobe sizes of sources with the greatest radio luminosities at the highest redshifts accessible to the observed samples. Of course, a combination of the two effects is also not ruled out. However, the result shows that with currently available samples it is not necessary to introduce yet more complicated models to explain the distribution of sources in the P-D-z data cube. Statistically, there is no preference between Model B and Model C. However, physically, the strong evolution of the density in the source environment required in Model B appears unrealistic. Thus, I will concentrate on Model C in the discussion of parameter dependencies, alternative models and the further implications of my results.

3.6.4 Potential problems

3.6.4.1 The power-law exponent, α

The parameter α is the power-law exponent which indicates how fast the environment density decreases away from the center AGN. In the previous sections, I used $\alpha = 2$, but most studies of the environments of low redshift radio galaxies in X-ray band imply that α could be closer to 1.5 than 2. Here I apply $\alpha = 1.5$ in the KDA model to check how much this would affect my results.

With a smaller value of α, the density of the environment decreases more slowly and the speed of growth of the lobe is slower. In this case, it is not surprising to find a larger maximum jet age. The best fitting parameters I find are $t_{\mathrm{max}}(0) = 1.1 \times 10^8$ yr, $\phi = 2.6$ for fixed $\Lambda_{\mathrm{max}} = 3.5 \times 10^8\,\mathrm{kg\,m^{-1.5}}$. The godness of fit decreases slightly to $P(D_{\mathrm{KS}}) = 72\%$ for 3CRR and $P(D_{\mathrm{KS}}) = 41\%$ for 6CE. The agreement is still good, and the value of $t_{\mathrm{max}}(0)$ is still consistent with the range discussed in Section 3.5. Therefore, the adopted value of α does not significantly affact my simulation results and conclusions. I will therefore continue to consider only models with $\alpha = 2$ in the following sections.

3.6.4.2 The axial ratio, R_T

In my construction of the artificial samples, I have used a fixed uniform distribution for the aspect ratio of the lobes R_{T}. Since R_{T} affects both the size and the radio luminosity of the lobes, it is reasonable to ask how much my results depend on my assumptions for R_{T}.

If I replace the uniform distribution of R_{T} (over the range 1.3 to 6) with a constant R_{T} for all model sources, then the distribution of lobe sizes within my artificial samples becomes slightly narrower. The average size also shifts somewhat, depending on the value

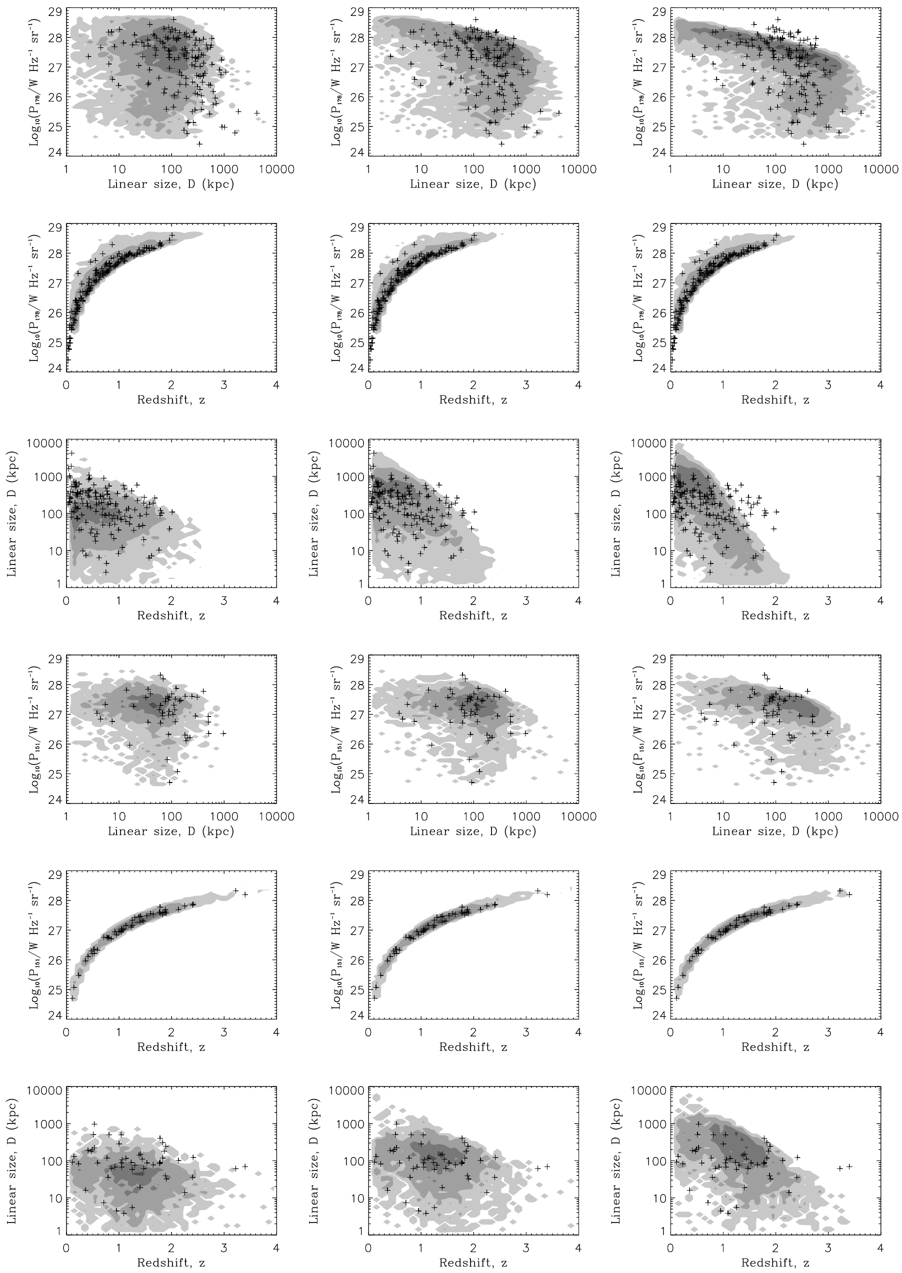

Figure 3.6: Projections of the P-D-z cube of observed and artificial samples with fixed R_T. The parameters I use here are those of the best fitting Model C. Here I only concentrate on 3CRR and 6CE samples as the fit to 7CRS is poor. The upper nine panes are artificial samples corresponding to 3CRR with constant $R_{\mathrm{T}} = 1.3, R_{\mathrm{T}} = 3.4$ and $R_{\mathrm{T}} = 6.0$ from left to right. The lower nine are artificial samples corresponding to 6CE with $R_{\mathrm{T}} = 1.3, R_{\mathrm{T}} = 2.8$ and $R_{\mathrm{T}} = 6.0$ from left to right.

assumed for R_T. This effect is illustrated in Figure 3.6. For Model C with the best fitting parameters, but a constant value for R_T, I find that the probability $P(D_\mathrm{KS})$ decreases to 34% for 3CRR ($R_\mathrm{T} = 3.4$) and remains constant at 59% for 6CE ($R_\mathrm{T} = 2.8$). I conclude that changing the range or distribution of R_T has only a minor effect on my results. This is particularly encouraging, because the alternative evolutionary models for individual sources I introduce below assume fixed values for R_T.

3.6.4.3 The RLF

The adoption of an RLF allows me to include the low-luminosity FRII sources in the artificial sample and is a more direct method to constrain the source distribution than the introduction of a birth function. In general, a RLF requires more parameters than a simple 'birth function'. The changes in these parameters may also change the simulation and fitting results. However, I have carried out tests that show that, within a reasonable range, the good agreement between artificial and observed samples is not affected by slight changes on the RLF parameters. As long as the shape of the RLF does not change too much and provides a good fit to the observations, the simulation results simply do not change very much. In particular, the conclusion that the FRII properties evolve with redshift does not depend on the choice of RLF parameters.

In order to test a more extreme modification to the RLF, I have also used a generalized luminosity function(GLF), which contains completely different parameters but gives similar curves, for comparison with the RLF of W01 used so far. The GLF is constructed by Grimes et al. (2004), considering both radio luminosity and optical luminosity of the AGN and introducing a parameter α' encoding the $L_{151} - L_\mathrm{OIII}$ correlation and a parameter β' encoding scatter about this correlation. The GLF based on α' and β' can generate a smoother RLF than the RLF of W01. However, the total source counts predicted by the GLF do not change very much compared to the RLF of W01 as Grimes et al. (2004) show in their Figure 11. If I substitute the GLF into Model C with the same best fitting parameters and a modified FRII fraction of 50% in the low-α' population, I still find a reasonable agreement with $P(D_\mathrm{KS}) = 34\%$ for 3CRR and $P(D_\mathrm{KS}) = 26\%$ for 6CE.

3.6.4.4 The 7CRS sample

The FRII fraction in the low-luminosity population is another parameter introduced in the RLF that can affect the fitting result. The value of 40% is adopted from the simulation. If I assume a smaller fraction, for example 20%, I find too few low-luminosity sources and the agreement with 3CRR and 6CE drops below 1%. Therefore, although some fainter surveys at low frequency such as the Bologna surveys indicate the FRII fraction at low luminosities could be smaller, I still need to choose 40% as the appropriate value for my work for fitting the 3CRR, 6CE and 7CRS samples.

However, in all my models discussed above I noted that my approach cannot provide an adequate fit to the source distribution of the 7CRS sample. The main problem appears to be the different relative number of sources at low redshifts and high redshifts in the various samples. This may be due to a changing mix of sources with different FR morphology below the break in the RLF. A closer look at the three observed samples reveals that the assumption that the FR II fraction is a constant may be too simplistic.

Within a range from $10^{24}\,\mathrm{W\,Hz^{-1}\,sr^{-1}}$ to $10^{26}\,\mathrm{W\,Hz^{-1}\,sr^{-1}}$ at 151 MHz the 3CRR sample contains 20 sources in a redshift range $0.005 \leq z \leq 0.16$ of which 12 show an FRII-type morphology. In the same luminosity range, 7CRS contains a total of 33 sources spanning a redshift range from $z = 0.086$ to $z = 0.775$ of which 26 are of type FRII. These numbers suggest an increased fraction of FRII-type sources within the low luminosity population at higher redshifts. The 6CE sample does not fit into this trend with 3 FRII-type sources out of a total of 7 within the luminosity range and at redshifts intermediate between 3CRR and 7CRS. However, the number of sources in this sample is very small.

Motivated by these numbers, I have carried out a test to see if a redshift dependence of the FR mix helps to improve the model fit to the 7CRS data. In this test, I set the FRII fraction within the low luminosity population of the RLF of W01 equal to $0.3 + z$ up to $z = 0.7$ and keep it at unity at higher redshifts. With this modification of the RLF the agreement of Model C with the 7CRS data increases, but not significantly with $D_{\mathrm{KS}} = 0.284$, which indicates $P(D_{\mathrm{KS}}) < 0.1\%$. The value of $P(D_{\mathrm{KS}})$ increases for 3CRR to 84%, while it decreases for 6CE to 47%. A comparison of the model with the observational

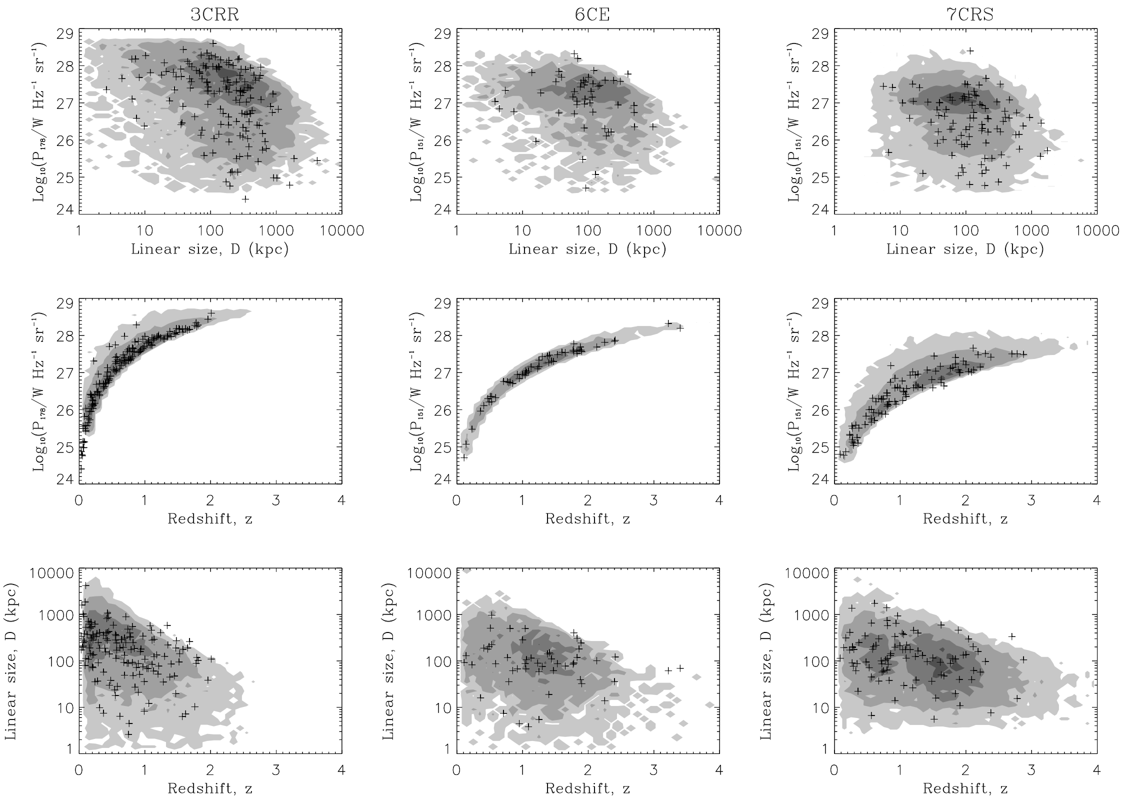

Figure 3.7: Projections of the P-D-z cube of the observed and artificial samples with a modified low-luminosity population of the RLF. The artificial sample is generated by Model C with the best-fitting parameters.

data is shown in Figure 3.7.

Changing the FR mix in the low luminosity part of the RLF does not have the desired effect of improving the fit with the 7CRS data. However, the presently available data do not allow me to decide whether a change with redshift in the composition of the radio source population is taking place or not.

From Figure 3.7 it is clear that there are too many sources in my artificial sample around $z = 2$ and $P_{151} = 10^{27}\,\mathrm{W\,Hz^{-1}\,sr^{-1}}$ compared to the 7CRS sample. This might be caused by the fixed value of p I chose as I discussed in Section 3.3. The FR IIs could have a flatter spectrum at high redshift which allows more sources to be included in the sample. However, as far as we have no idea of the spectral index evolution, I will concentrate on the influence from the RLF. In fact, this problem, that the RLF of W01

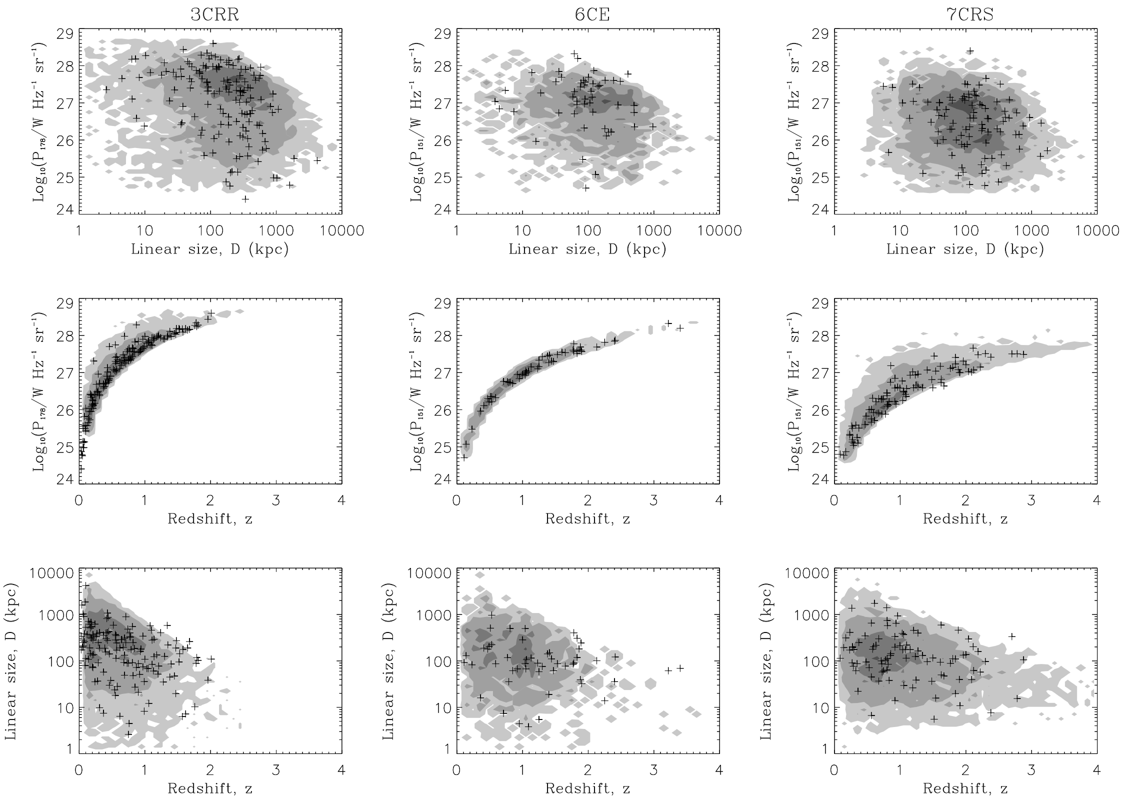

Figure 3.8: Projections of the P-D-z cube of the observed and artificial samples with both the low and high luminosity populations of the RLF modified. The artificial sample is generated by Model C with the best fitting parameters.

overpredicts the number of sources with this radio luminosity at this redshift compared to 7CRS, is discussed by W01 (see their Figures 7 and 8). The 7CRS data is consistent with no further evolution of the high luminosity part of the RLF beyond redshift $z = 1$. Implementing such a constant RLF at redshifts beyond $z = 1$ in my model dramatically improves the agreement between my Model C and the 7CRS data to $P(D_{\rm KS}) = 17\%$. However, this RLF reduces the agreement between Model C and the 3CRR sample to $P(D_{\rm KS}) = 0.1\%$ while $P(D_{\rm KS})$ for the 6CE sample drops below 0.1%. Therefore it is unlikely that this modification of the RLF is correct. The 7CRS sample covers a very small sky area compared to the 3CRR and 6CE samples. This may imply that the members of this sample are not fully representative of the entire source population. Comparisons of the artificial samples arising from this modification of the RLF with the observations are shown in Figure 3.8. Thus, in the following discussion, I am still using the original RLF, exclusively in Section 3.7, I use modified RLF on 7CRS simulations only, just for getting better fits.

3.6.5 Comparing the 3CRR sample with an equivalent sample

The BRL sample, as discussed in section 2.4, is roughly equivalent to 3CRR with a similar flux limit and source number. Thus the BRL sample and the 3CRR sample can be considered as two samples drawn from the same parent population with similar selection criteria, but from different areas of the sky. The comparison between these two independent samples evaluate the robustness of the inferences drawn from the comparison of the models to the observations.

The BRL sample is observed at 408 MHz, so I use a constant spectral index of -0.8 to convert the radio luminosity of BRL sources to 178 MHz. I ignore the sources whose luminosity is below the flux limit given by 3CRR. Comparing the 3CRR sample and the BRL sample in the P-D-z data cube, I get $D_{\mathrm{KS}} = 0.266$ from the 3-D KS test. If I choose an artificial BRL sample with the same source number as the real BRL sample from the best-fitting artificial 3CRR sample and compare with the real 3CRR sample, D_{KS} is mostly between 0.1 to 0.2. As the smaller values of D_{KS} indicate a better fit, this shows that my best-fitting artificial sample agrees with the observations to a degree similar to the agreement between similar observed samples drawn from the same source population. Figure 3.9 shows the 3CRR sample and the BRL sample in the P-D-z data cube.

3.7 Comparison between models of radio lobe evolution

Before discussing my results in more detail, I now assess how much they depend on my particular choice for the model of the evolution of individual sources. The KA97 model describing the dynamics and expansion of the radio lobe essentially relies on the condition of ram pressure balance between the jet material and the receding ambient gas in front of it. This condition was first introduced by Scheuer (1974) and has formed the basis for

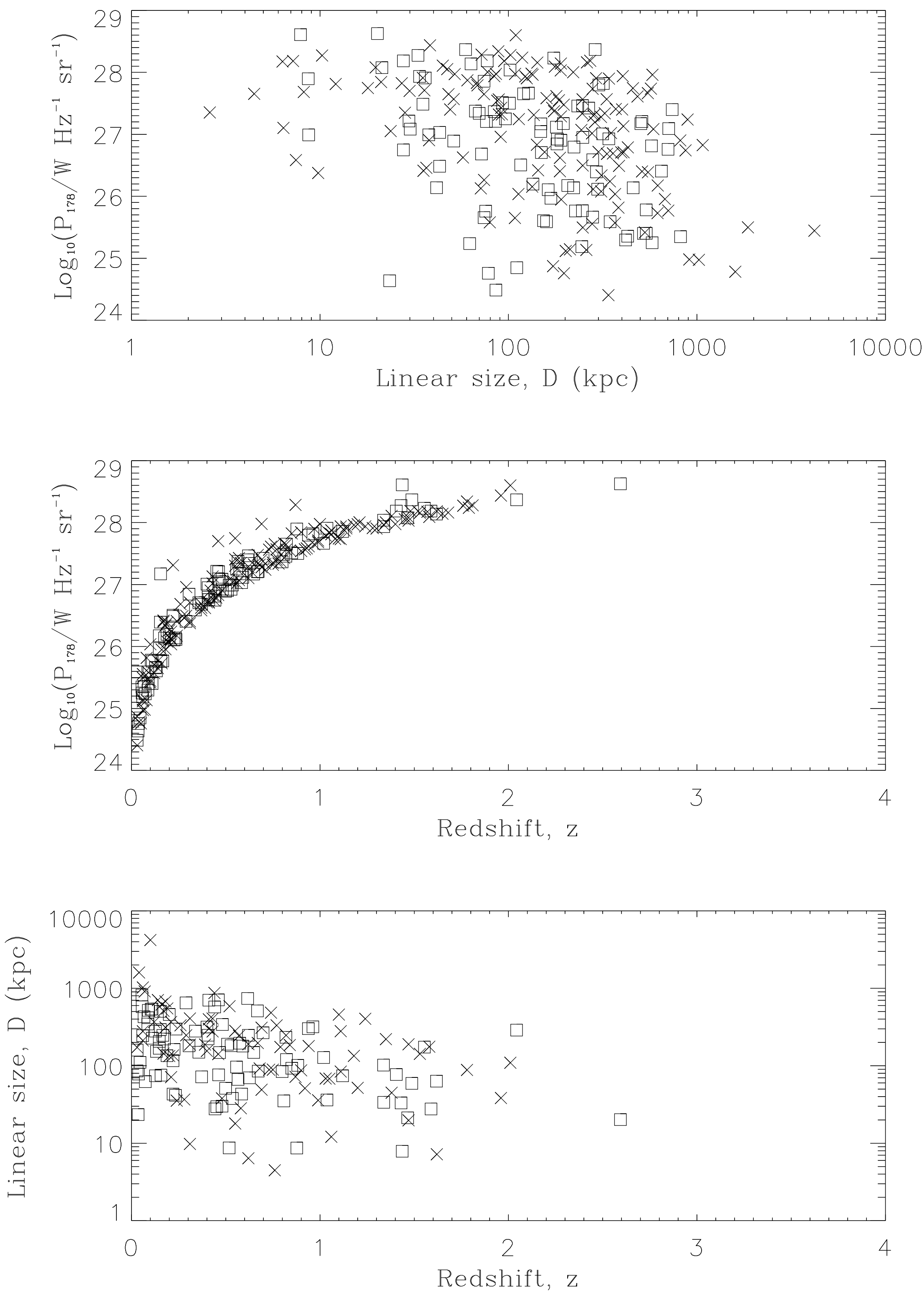

Figure 3.9: 3CRR and BRL objects in the P-D-z diagram at 178 MHz. Cross symbols refer to 3CRR while squares refer to BRL. Iconvert the BRL sources from 408 MHz to 178 MHz by using a common spectral indexes of 0.8

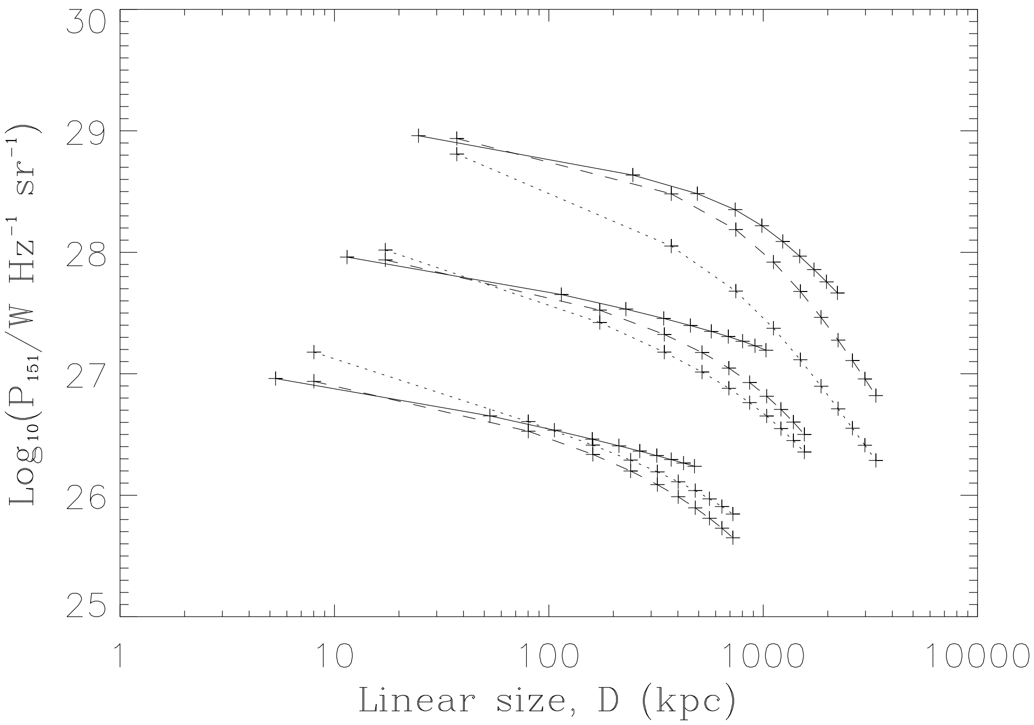

Figure 3.10: Evolutionary track for three sources with different models. The upper curves are for $Q_0 = 1 \times 10^{40}$ W and $z = 1.5$, the centre curves are for $Q_0 = 1 \times 10^{39}$ W and $z = 0.5$, and the lower curves are for $Q_0 = 1 \times 10^{38}$ W and $z = 0.2$. Each of the solid, dashed and dotted curves refer to the tracks given by KDA, MK and BRW models respectively. The pluses on the curves are time markers denoting source lifetimes of 1,10,20,...90 Myr.

virtually all subsequent models of the dynamical evolution of radio sources with an FRII-type morphology (e.g. Begelman & Cioffi, 1989; Falle, 1991; Nath, 1995; Chyzy, 1997). While the details of the derivation of the lobe dynamics differ, the basic principle is the same. As I do not consider in detail the evolution of individual objects, I therefore do not use another dynamical source model.

Beside the KDA model, two alternative descriptions for the emission properties of the lobes have been formulated by BRW and MK. The main difference between these models and KDA is the treatment of the radiating electrons as they propagate from the ends of the jets, or hotspots, into the lobes. The KDA model assumes that the energy distribution of the electrons injected into the lobe is described by a simple power-law, with a given minimum and maximum. By contrast, BRW considers broken power-law for the energy distribution and treat the pressure in the head region differently with the pressure in the hotspot. MK describe in detail the diffusion of the electrons from the hotspot into the lobe, taking into account radiative energy losses and possible re-acceleration.

Figure 3.10 shows a comparison of the luminosity evolution of a single radio source as described by the three models. The luminosity evolution is steeper for the two alternative models, with the BRW model being the steepest. The MK model is consistent with the KDA model when the source is young but its track is more like the BRW model when the source is old. The evolutionary tracks shown in the picture are comparable with the tracks in the original papers, and the small differences is because I am using different implementations like I am using $\beta = 2$ here. In the following sections, I will describe both models with my implementations in more details and then substitute them for the KDA model in my Monte-Carlo simulations. BW06 and BW07 use the same models in their comparisons.

When comparing the results arising from the three different evolutionary models, I employ Model C with $\Lambda_{\rm max} = 1.6 \times 10^{18}\,{\rm kg\,m^{-1}}$, consistent with the original formulation of BRW and MK. However, to allow a direct comparison with my previous results, I am making my implementation of these two models by setting $\alpha = 2$, $\gamma_{\rm min} = 1$ and $\gamma_{\rm max} = 10^5$ Meanwhile, as the modified RLF could supply a better fit for 7CRS sample, I use the modified RLF described in Section 3.6.4.4 for 7CRS simulations. However, for the 3CRR and 6CE samples I continue to use the unmodified RLF.

3.7.1 The BRW model

Unlike the KDA model assuming a single power-law of energy distribution, BRW considers that the injection index has two breaks. In the low-energy regime, the exponent is 2, in the high energy regime, the exponent is 3 and between the two breaks, a certain value between 2 and 3 can be adopted. The positions of the breaks are decided by the longest and shortest times that particles reside in the hotspot. Following BRW, I take these two times to be 10^5 and 1 yr. Another main difference between KDA and BRW is that the

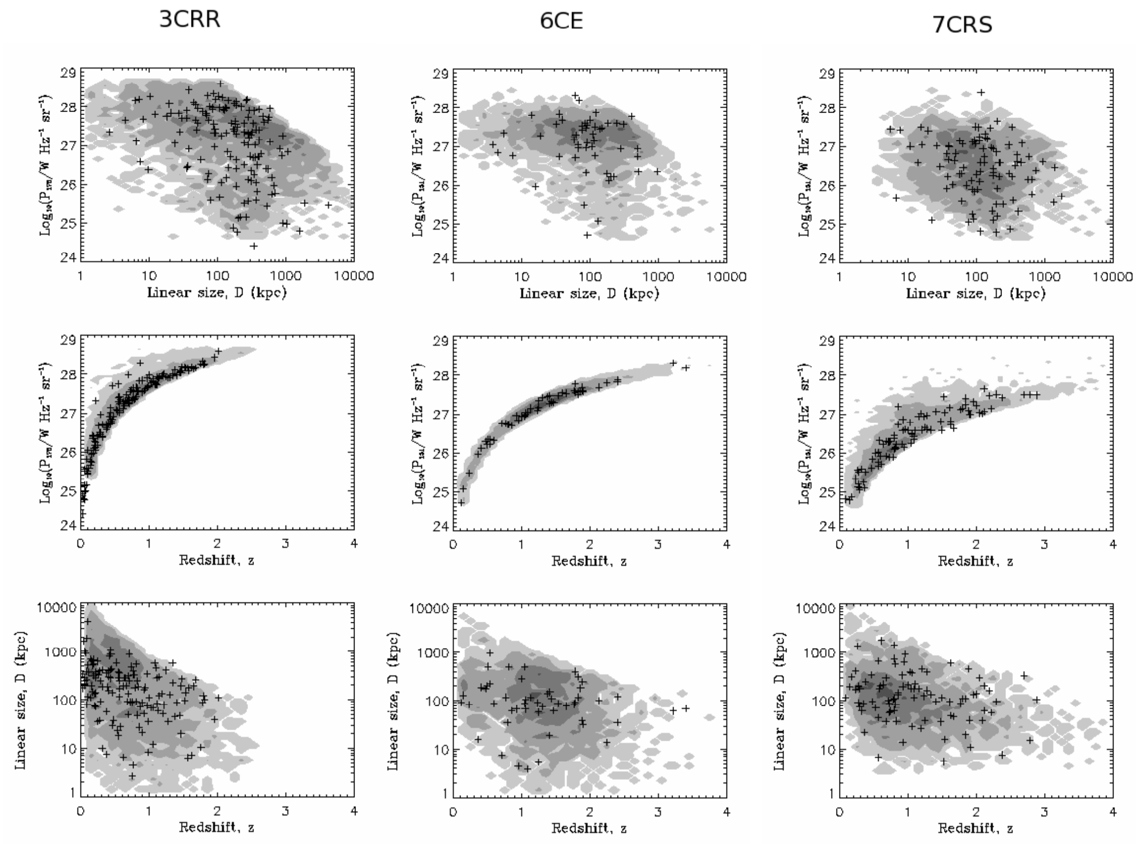

Figure 3.11: Projections of the *P*-*D*-*z* cube of the observed samples with source density contours generated by the BRW model in the framework of Model C. The parameters I use here are $t_{\max}(0) = 5.0 \times 10^7\,\mathrm{yr}$, $\Lambda_{\max} = 1.6 \times 10^{18}\,\mathrm{kg\,m^{-1}}$ and $\phi = 2.4$. Crosses indicate FRII sources in the observed samples. Gray scales indicate the number density of the artificial samples.

BRW model introduced two different pressures. The first one is the pressure in the head of the source, which is the average value of internal pressure across the entire head of the source. It is associated with the environmental ram pressure and the pressure in the lobe, which means it governs the growth of the source length. The other pressure is the hotspot pressure which is closely related to the jet power and given by their equation (10). The hotspot pressure not only governs adiabatic losses out of the hotspot but also decides the break frequencies as it decides the magnetic field in the hotspot with energy equipartition assumption. The final luminosity is given by their equation (21) and I solve it numerically.

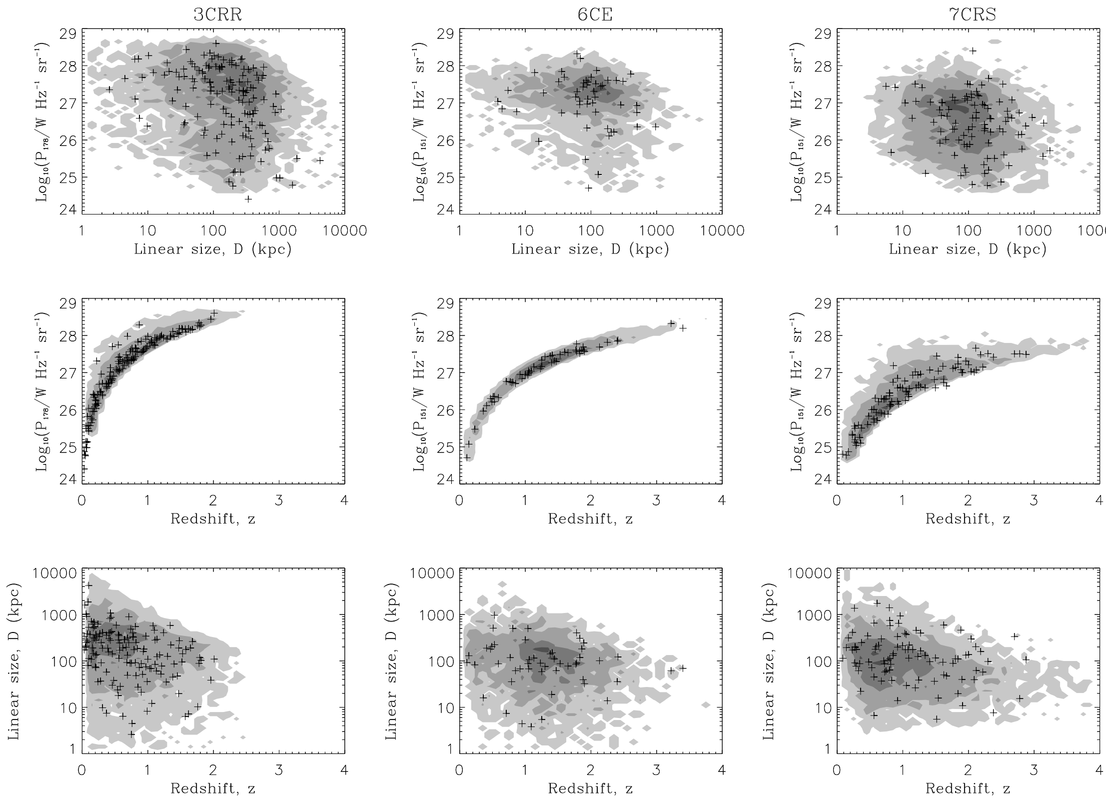

Figure 3.12: Projections of the P-D-z cube of the observed samples with source density contours generated by the MK model within the framework of Model C. The parameters I use here are $t_{\rm max}(0) = 4.0 \times 10^7\,{\rm yr}$, $\Lambda_{\rm max} = 1.6 \times 10^{18}\,{\rm kg\,m^{-1}}$ and $\phi = 2.5$. Crosses indicate FRII sources in the observed samples. Gray scales indicate the number density of the artificial samples.

Figure 3.10 shows that the evolutionary tracks from the model is steep, especially at high redshift. I have to raise the maximum allowed jet power to 10^{41} W in order to cover the sources in the top-right of the P-D diagram. The best agreement of Model C is achieved around $t_{\rm max}(0) = 5.0 \times 10^7\,{\rm yr}$ and $\phi = 2.4$. It gives a $P(D_{\rm KS}) = 14\%$ for 3CRR sample, $P(D_{\rm KS}) = 30\%$ for 6CE sample and $P(D_{\rm KS}) \sim 1\%$ for 7CRS sample. Although it is a bit lower than the KDA model, considering the parameter settings I am using tend to the KDA model, the data above shows that I could also use the BRW model to predict the artificial samples which have a good agreement with the observational samples. Figure 3.11 shows the result of replacing the KDA model in my method with the BRW model.

3.7.2 The MK Model

The MK model is similar to the BRW model, as it also assumes that the jets end in hotspots of a constant physical size, which also contain a magnetic field of constant strength. The radiating electrons are accelerated to an initial power-law energy distribution within the hotspot. In contrast to the BRW model, MK exactly follow the subsequent evolution of the energy distribution under the influence of adiabatic and radiative energy losses as the electrons diffuse through the hotspot into the lobe. More specifically, MK adopt a diffusive transport model in which the mean square distance traveled by individual electrons on their way from the hotspot into the lobe is proportional to t^{μ}, where t is the time since their acceleration. A value of $\mu = 1$ corresponds to the diffusion regime, and I adopt this here, since the sub-diffusion regime, $\mu < 1$, makes the model comparable to the BRW model and the supra-diffusion regime, $\mu > 1$, approximates the KDA model.

The MK model takes into account adiabatic and radiative losses of the electrons during the diffusion process. However, MK find that the adiabatic losses lead to luminosity evolution of their sources in disagreement with observations. To avoid this problem I adopt their model B, with all corresponding parameter settings, which neglects adiabatic losses. I also follow MK in setting the ratio of the diffusive transport time and the cooling time of an electron, their parameter τ, to 2×10^{-3}. After the electrons have diffused into the lobe, the MK model describes the further evolution of the electron energy distribution in the same way as the KDA model. An example for the luminosity evolution using the MK model in the way described here is shown in Figure 3.10.

Replacing the KDA model with the MK model in my method, I find the best fitting Model C with the parameters $t_{\rm max}(0) = 4.0 \pm 0.2 \times 10^{7}\,$yr and $\phi = 2.6 \pm 0.1$ for 3CRR at $P(D_{\rm KS}) = 53\%$. For 6CE I find $P(D_{\rm KS}) = 58\%$ for $t_{\rm max}(0) = 4.2 \pm 0.3 \times 10^{7}\,$yr and $\phi = 2.5 \pm 0.1$. Thus, the values of the model parameters agree between the two samples, and Figure 3.12 shows a comparison of the artificial and observed samples for $t_{\rm max}(0) = 4.0 \times 10^{7}\,$yr and $\phi = 2.5$ resulting in $P(D_{\rm KS}) = 41\%$ for 3CRR, $P(D_{\rm KS}) = 50\%$ for 6CE and $P(D_{\rm KS}) \sim 1\%$ for 7CRS, with the modified RLF. The fitting result for 7CRS is not as good as that for the KDA model, because the evolutionary tracks of the MK model are steeper and predict more sources with small linear size at the high redshift / high luminosity end.

For the 3CRR and 6CE samples, the MK model provides a level of agreement between the artificial and observed samples similar to that of the KDA model. The somewhat higher value for $t_{\rm max}(0)$ I find for the MK model is partially due to the large value of $\Lambda_{\rm max}$ I use for this model compared to the KDA model. However, the steeper luminosity evolution of the MK model also requires somewhat longer lifetimes of the sources to accommodate the larger objects. With the currently available data I cannot decide which of the two models provides a better description. I continue to focus on the KDA model because its mathematical formulation is simpler than that of MK.

3.8 Discussion

In this chapter, I have created artificial samples of radio-loud AGN with an FRII-type morphology and compared their properties with those of observed samples. I find that the artificial samples are consistent with the observed ones, provided that there is some cosmological evolution of the radio source population. The models require either that the density of the source environments increases on average with increasing cosmological redshift, or that the lifetime of the jet flows decreases with increasing redshift. A combination of both effects may also be at work. To simplify the following discussion of the properties of the artificial samples, I concentrate on model C, implying the cosmological evolution of the jet lifetimes, for the reasons given in Section 3.6.3.

With certain assumption, my implementation of the BRW and MK model will still predict the observational samples with reasonable fittings. BW07 considered modified models taking into account the increase of hotspot sizes with jet lengths. They found that the modified BRW and MK models produce better fits which are at least as good as the KDA model, while the modified KDA model produces a worse fit. Different parameter settings do give predictions for each models. However, as far as I am not attempting to construct a new, improved model or the best values of parameter settings for individual

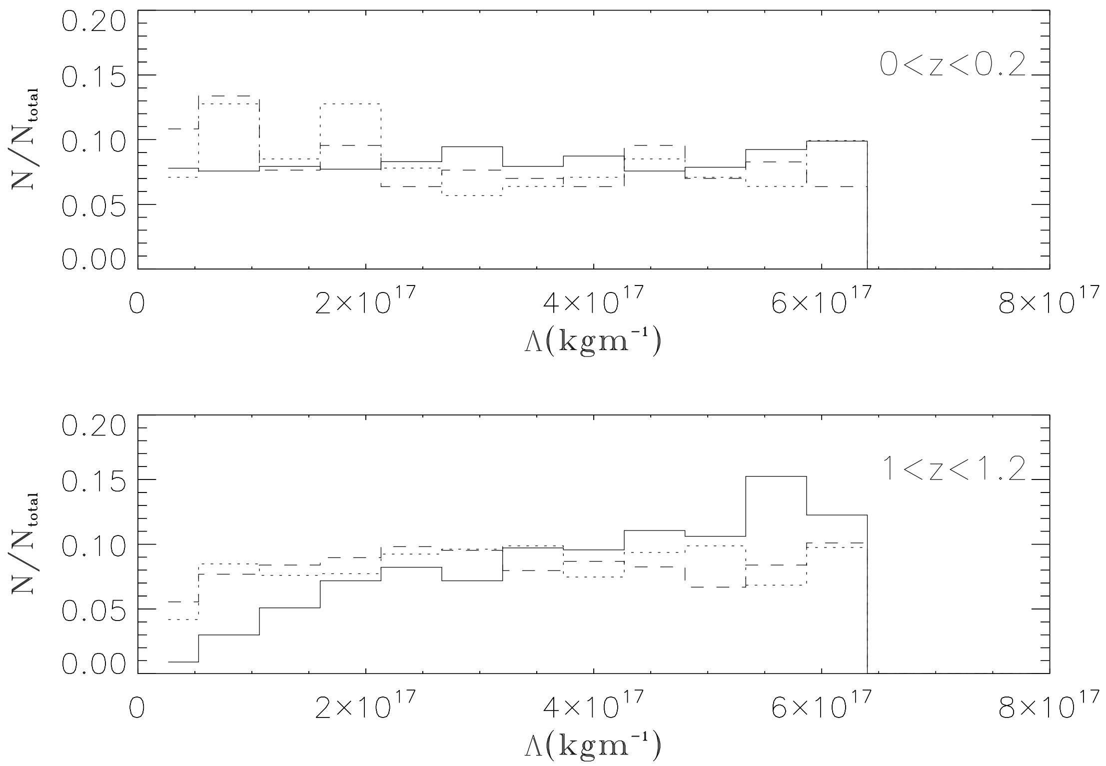

Figure 3.13: Final Λ distribution of the artificial samples generated by Model C in two redshift ranges. The upper plane is for $0 \leq z \leq 0.2$ and the lower plane is for $1.0 \leq z \leq 1.2$. $N_{\rm total}$ is the total source number in each redshift bin. The solid line is for 3CRR, the dotted line for 6CE and the dashed line for 7CRS.

FRII-type objects, and so I concentrate on the original KDA model which is considerably simpler and mathematically less complex.

In constructing my artificial samples, I choose random values for the density parameter Λ and the source age t from uniform distributions. The jet power Q_0 is then adjusted to give the model source the correct radio luminosity. Not every possible combination of the set of three parameters Λ, t and Q_0 is allowed, because of restrictions on the magnitude of Q_0 and the selection criteria of the observed sample I compare with. It is therefore not clear *a priori* whether the distributions of Λ and t amongst the objects within the final artificial sample are also uniform. Any deviation from a uniform distribution in the final sample may reveal a genuine property of the source environments or source ages in the universe.

I first investigate the distribution of Λ in the artificial sample arising from Model C. Figure 3.13 shows the binned distribution of Λ for two different redshift ranges, $0 \leq z \leq 0.2$ and $1 \leq z \leq 1.2$. At low redshifts the distribution is uniform within the fluctuations arising from the finite number of sources in the artificial samples, regardless of which observed sample I compare with. At high redshifts the distribution of Λ in the artificial sample mimicking the 3CRR sample is biased towards large values. The distributions within the artificial samples compared with 6CE and 7CRS remain uniform except for a drop in the bin of the smallest density. This behaviour is caused by the flux limits of the samples. Objects located in denser environments are more luminous. At low redshifts the flux limit of all samples corresponds to such low luminosities that the entire radio source population with an FRII-type morphology is represented in the samples. However, at higher redshifts the flux limit excludes sources in less dense environments as their luminosity is too low. Samples with a lower flux limit, like 6CE and 7CRS, obviously suffer less from this problem.

The result for the final distribution of Λ arising from an initially uniform distribution suggests that my current data is insufficient to constrain the distribution of the environmental properties of FRII-type sources. The uniform distribution 'survives' unchanged through the source selection process. However, it is also possible that the distribution of Λ in the universe itself is actually uniform, i.e. that I have selected the correct distribution by chance. To test this I have generated artificial samples with a Gaussian distribution and also a fixed value of Λ. As discussed in Section 8.3, the artificial samples using these two alternatives agree with the observed samples to a similar degree as the standard Model C with a uniform distribution. The final distribution of Λ in the artificial sample drawing random values from a Gaussian distribution is also Gaussian. By construction, all the sources in the final sample with a fixed value of Λ are assigned this one value. From these results I conclude that the distribution of Λ in the universe cannot be constrained with the currently available data.

The distributions of source ages in my artificial samples for two redshift bins are shown in Figure 3.14. The distributions at low redshift are uniform with a slow decrease for old ages. This decrease is caused by two effects. For Model C, the source lifetime decreases with increasing redshift. Hence within the respective redshift ranges there is also, by

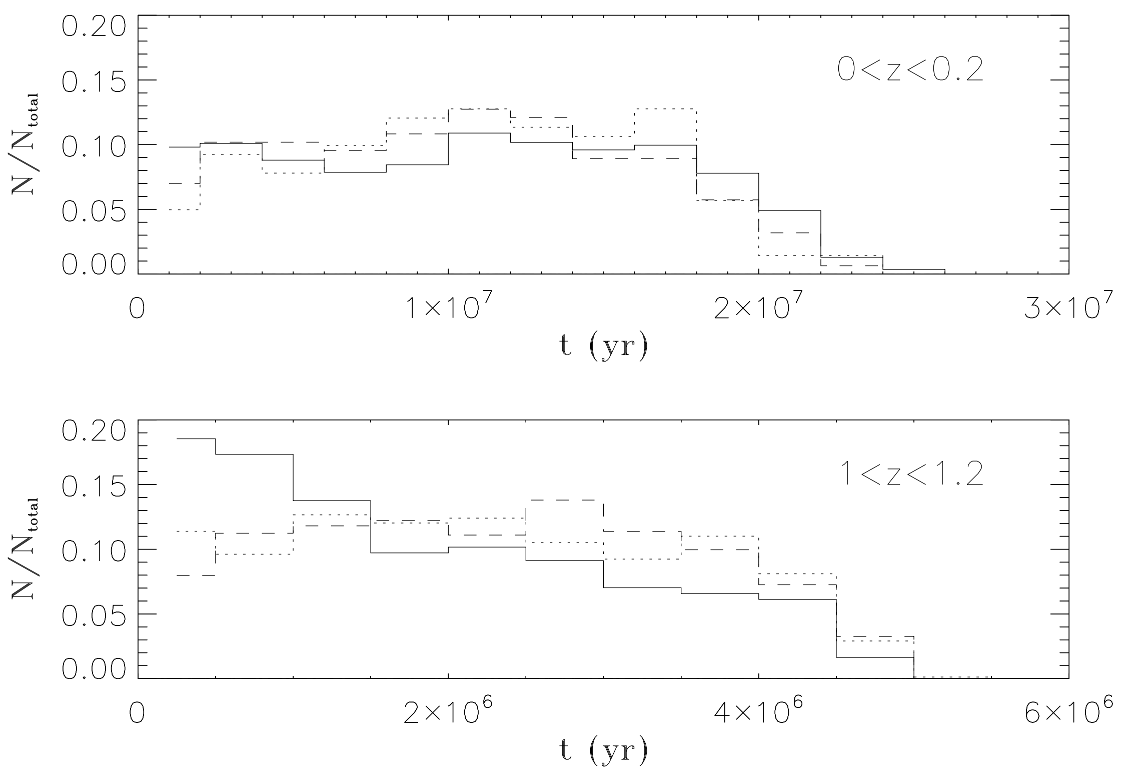

Figure 3.14: Final distribution of t in the artificial samples generated with Model C in two redshift ranges. The upper plane is for $0 \leq z \leq 0.2$ and the lower plane is for $1.0 \leq z \leq 1.2$. $N_{\rm total}$ is the total source number in each redshift bin. The solid line is for 3CRR, the dotted line for 6CE and the dashed line for 7CRS.

construction, a range of source lifetimes. Sources towards the high redshift end of the range cannot contribute to the bins of t corresponding to the oldest sources. The second effect is again due to the flux limit of the samples. The radio luminosity of sources decreases as they get older. Therefore older sources are less likely to be included in the samples (see also Gopal-Krishna et al., 1989; Blundell & Rawlings, 1999).

At higher redshifts the high flux limit of the 3CRR sample leads to an age distribution skewed towards younger ages, where the sources are more luminous. This effect plays no significant role for the 6CE and 7CRS samples because of their lower flux limits. The drop in the source numbers in the bin containing the youngest objects is caused by the limit I impose on the size of sources included in the artificial samples.

The uniform distribution of t in the artificial samples is consistent with my assumption of a maximum lifetime common to all sources at a given redshift. Any deviations from a uniform distribution, apart from those discussed above, would imply that my assumption is flawed. However, I cannot turn this argument around. The fact that the uniform distribution of t 'survives' the source selection in my model only demonstrates that, similarly to the situation with the distribution of Λ, the current data does not constrain the distribution of source lifetimes. I cannot conclude that $t_{\rm max}$ is the same for all sources at a given redshift.

I do not initially constrain the distribution of the jet power, Q_0, to take a specific form, as I do with Λ and t. Instead, for each source, I adjust Q_0 to give the correct radio luminosity using the randomly selected values for Λ and t. The only restrictions I apply are that Q_0 cannot lie outside the range from 10^{37} W to 5×10^{40} W. In this way the resulting final distribution for Q_0 arises from the constraints of the observed samples themselves. Figure 3.15 shows the results for the artificial samples related to the 3CRR and 7CRS samples for three redshift ranges. I do not consider the result for the 6CE sample here, as this sample also has an upper flux limit which affects the distribution of Q_0 at the high power end.

The shape of the distribution at the low power end is determined by the flux limit of the observed samples. Weaker jets produce less luminous lobes below the flux limit, unless the sources are located in very dense environments and/or are very young. For high jet powers, I expect that virtually all objects are above the sample flux limit, independent of environment or age, and that the Q_0 distributions shown in Figure 3.15 are representative of the entire radio source population in the universe. This is supported by the agreement in the slope of the distributions for the 3CRR and the 7CRS samples in this region. The distribution for the artificial sample corresponding to the 3CRR sample turns over at higher jet powers because the flux limit for this sample is higher. I do not show results for redshifts beyond $z = 0.6$, because there the flux limit influences the high power end of the distribution, even for 7CRS.

The high power part of the Q_0 distribution is well approximated by a power-law. I find that $\mathrm{d}N/\mathrm{d}\log Q_0 \propto Q_0^{-0.90}$ for all three redshift ranges shown in Figure 3.15. I do not find

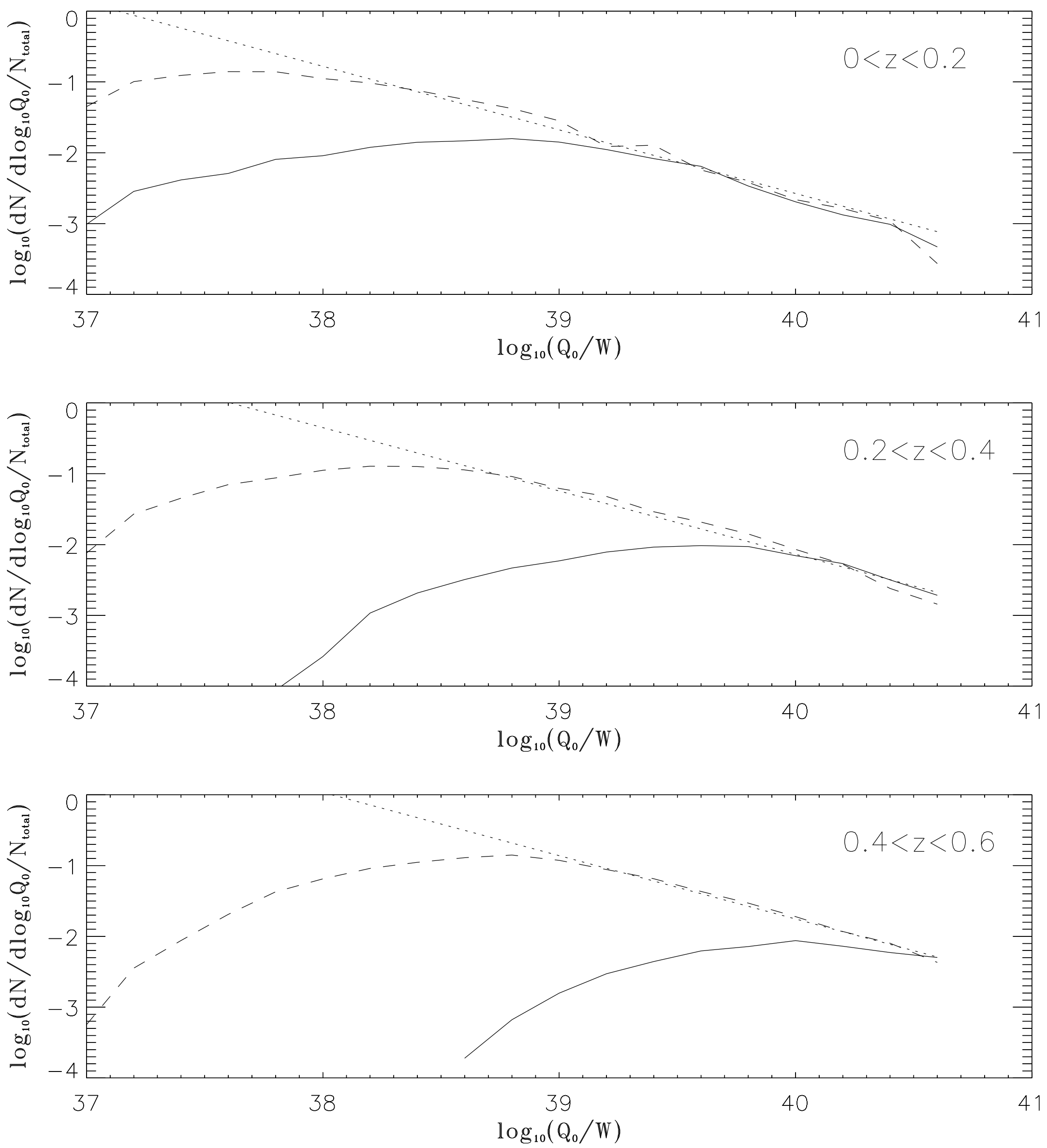

Figure 3.15: Final distribution of jet power, Q_0 in three redshift ranges. $N_{\rm total}$ is the total source number in each redshift bin. The solid line is for 3CRR, the dashed line for 7CRS and the dotted line shows a power-law with exponent -1. Ihave normalized the number of the sources so that the curves at the high power end of the artificial samples equivalent to 3CRR and 7CRS are aligned.

any evidence for a change of this power-law slope as a function of redshift. I have also tested whether the slope changes when I change some parameters in the simulation proccess. If I adopt $\alpha = 1.5$, I find an exponent of -1.05, and the artificial samples from the GLF give an exponent of -0.89. Again, if I adopt a different initial distribution for Λ as discussed in Section 8.3. For the Gaussian distribution the slope of the Q_0 distribution becomes slightly steeper, $\mathrm{d}N/\mathrm{d}\log Q_0 \propto Q_0^{-0.95}$. For the extreme assumption of a single value of Λ for all sources, I find a change of the power-law exponent to -1.3.Thus, I conclude that $\mathrm{d}N/\mathrm{d}\log Q_0 \propto Q_0^{-1}$. This result does not depend on the uncertain value of α or the plausible values for the parameters describing the RLF, or the assumed distribution of Λ as long as very extreme assumptions, e.g. a single value of Λ for all sources, are avoided.

Various other authors have tried to constrain the distribution of Q_0 as well. Most of these studies present values for $\mathrm{d}N/\mathrm{d}Q_0$ rather than $\mathrm{d}N/\mathrm{d}\log Q_0$. Ican easily convert my result by noting that $\mathrm{d}N/\mathrm{d}Q_0 = Q_0^{-1}\mathrm{d}N/\mathrm{d}\log Q_0 \propto Q_0^{-2}$. BRW from their work suggest that the power-law slope should be -2.6. More recently BW07 argued for a steeper exponent of -3, while KB07 find a value of -1.6. My result is somewhat flatter than those of BRW and BW07, but slightly steeper than that of KB07. The differences may be caused by the steeper luminosity evolution of the BRW model and the assumption of a single value for Λ in BW07. KB07 ignored the effect of radiative energy losses of the synchrotron emitting electrons on the luminosity evolution, which may explain the flatter distribution found by them.

The KDA model assumes that the energy contents of the magnetic field and of the relativistic, synchrotron radiation emitting particles in the lobe initially follow the minimum energy relation (e.g. Longair, 1994). Radiative energy losses change this situation somewhat for older sources, but the deviations of the model from minimum energy conditions are small for most sources. Under minimum energy conditions, the strength of the magnetic field and the volume of the emission region completely determine the radio luminosity. Meanwhile, in KA97 model, the volume of the lobe is determined by its length, and the energy density of the magnetic field is determined by $\gamma_{\rm min}$ and the lobe pressure, $p_{\rm c}$. As far as I am considering a fixed $\gamma_{\rm min}$ in this thesis, the measurements of lobe length and radio luminosity allow only a small range of possible lobe pressures. The data from

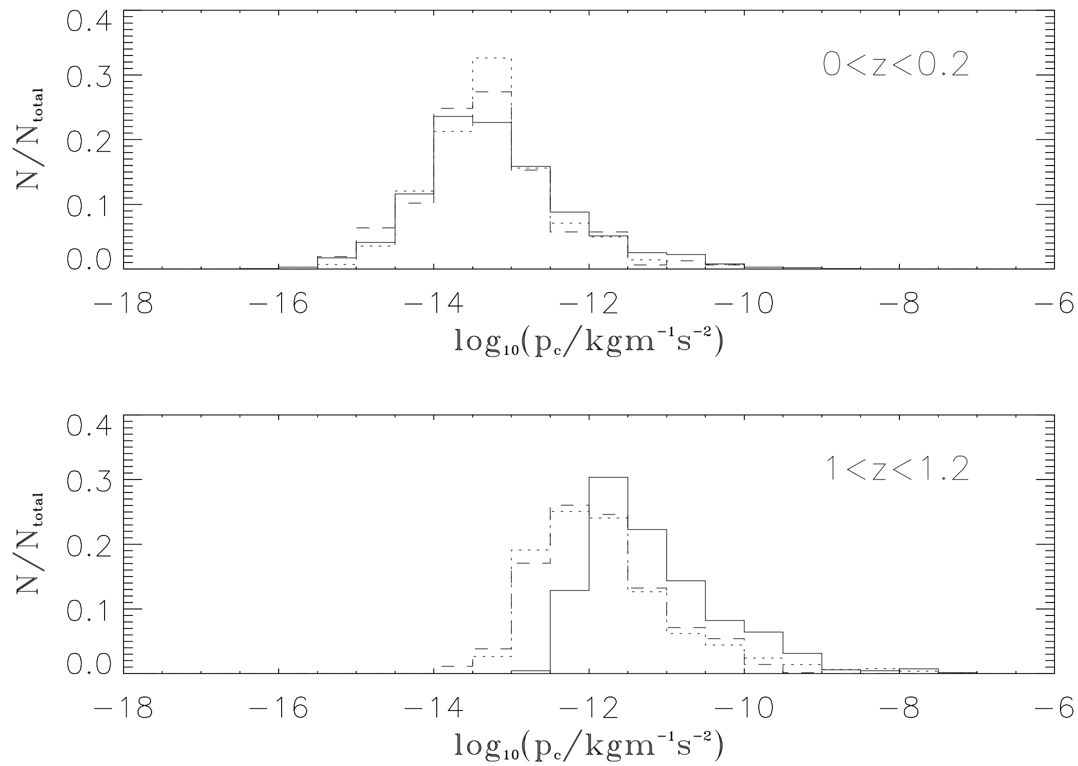

Figure 3.16: Final distribution of lobe pressures, p_c, in two redshift ranges. The upper plane is for $0 \leq z \leq 0.2$ and the lower plane is for $1.0 \leq z \leq 1.2$. $N_{\rm total}$ is the total source number in each redshift bin. The solid line is for 3CRR, the dotted line for 6CE and the dashed line for 7CRS.

the observed samples should therefore tightly constrain the distribution of lobe pressures in my artificial samples.

Figure 3.16 shows the distributions of the lobe pressure for two different redshift ranges. The agreement between the three samples at low redshifts is good, indicating that the different flux limits do not influence the shape of the distribution. I take this as evidence that at low redshifts, I observe the entire FRII population. At high redshifts, the sample with the highest flux limit, 3CRR, shows a shift of the peak in the pressure distribution to higher pressures compared to the other samples. Sources with lower lobe pressures are not luminous enough to be included in the sample and hence are missing. The agreement between the artificial samples corresponding to 6CE and 7CRS may indicate that these samples still include the entire source population at this higher redshift.

The pressure distribution is peaked, and the peak shifts to higher values at higher redshifts. My Model C implies that the maximum lifetime of a source decreases as $(1+z)^{-2.4}$ with increasing redshift. This also implies a proportional decrease of the average age of sources, $\langle t \rangle$, included in the sample. My implementation of the KA97 model predicts that $\langle p_{\rm c} \rangle \propto \langle t \rangle^{-2}$ and therefore $\langle p_{\rm c} \rangle \propto (1+z)^{4.8}$. I thus expect the average lobe pressure to increase by a factor of roughly 22 (1.35 in the logarithmic scale used in Figure 3.16) between redshifts $z = 0.1$ and $z = 1.1$. This is consistent with the shift of the peak in the pressure distributions for the samples with the lower flux limit in the Figure 3.16.

Given the good agreement of the pressure distributions between the artificial samples corresponding to 6CE and 7CRS in both redshift ranges, I argue that the samples cover the entire FRII source population at both redshifts without excluding too many sources through the respective flux limits. If so, then the shift of the peak in the pressure distribution with redshift is evidence for cosmological evolution of the population. This conclusion does rely on my assumption of conditions close to those described by minimum energy assumptions inside the lobes, but it does not depend on the additional assumption of Model C of a decreasing maximum lifetime of sources with increasing redshift. The application of Model B would result in the same shift in the pressure peak. Unless I invoke a systematic change with redshift away from minimum energy conditions inside the lobes, the data imply that the average lobe pressure is increasing rapidly with redshift out to about $z = 1$. Beyond this redshift, the flux limits of the samples used here exclude some of the FRII-type objects, and so I cannot determine whether this trend continues. Also, the current data do not allow me to determine whether this increase in pressure with redshift is due to decreasing source lifetime and/or to an increase in the density of the surrounding medium.

BRW and BW06 use a similar approach to constraining the radio source population. BW06 tested their artificial samples by 2-dimensions while BRW did a 4-way Spearman-Rank analysis. Here I do a 3-dimensional KS test in the P-D-z plane. I do not consider the spectral index since the evolutionary models of FRII sources themselves restrict the possible range of the spectral index. My result is similar to that of BW06, in that the BRW model does not provide an agreement as good as the other two models. However, between the other two models, BW06 prefer the MK model, as it produces a better description of the source number ratios at different redshifts. In my work, I use the RLF to avoid the fitting of number ratios and find that the KDA model gives a slightly better fit than the MK model. The KDA model is also simpler than the MK model, and so I slightly prefer the KDA model here. Using the RLF, I do not need to constrain the distribution of jet powers as BRW and BW06 were required to do. The final distribution of Q_0 in my artificial samples agrees with a power-law distribution with an exponent of approximately -2, which is flatter than the assumption of BRW and the best fit values found by BW06.

3.9 Conclusions

I have constructed a method for generating artificial flux-limited radio samples. I use these samples to study the cosmological evolution of the FRII source population by comparing to several observed samples. I use three different models for the evolution of the linear size and the radio emission of individual FRII sources from KDA, BRW and MK. Comparing artificial with observed samples, the 3-D KS test indicates that these three models provide similar simulation results, which means individual model is not the key factor that decide the distributions of the complete samples.

The properties of FRII sources are required to evolve with the redshift in order for the my artificial sample to reproduce the observations. For $\alpha = 2$, I introduce two models that can both meet the observational requirements:

- Model B: The maximum value of the environment density parameter Λ evolves with redshift. I describle Model B with best fitting parameters by $t = r \times 5 \times 10^7\,\mathrm{yr}$, $\Lambda = r \times 3.7 \times 10^{17}(1+z)^{5.8}\,\mathrm{kg\,m^{-1}}$, where r is a random number with uniform distribution between 0 and 1.

- Model C: The maximum jet age evolves with redshift. Similar to Model B, Model C can be expressed by $t = r \times 2.7 \times 10^7(1+z)^{2.4}\,\mathrm{yr}$, $\Lambda = r \times 6.4 \times 10^{17}\,\mathrm{kg\,m^{-1}}$.

Both Models B and C produce artificial samples in agreement with the observed samples according to 3-D KS test. I cannot decide statistically whether a reduced maximum age or a denser environment is present at high redshift. Of course, I also cannot rule out a combination of these two effects as well. Physically, it seems more likely that a moderate increase of Λ combines with a reduction of the jet lifetimes to produce the observed effect.

Using my artificial samples, I have studied the distribution of the properties of FRII sources. The input distributions of Λ and t are taken to be uniform, and I find that these shapes survive the source selection process in my simulations. I have shown explicitly that this implies that their true distributions cannot be constrained by the currently available data. Unlike Λ and t, I do not initially constrain the distribution of Q_0, but find that a power law distribution arises naturally in the final artificial samples. I find a power law exponent of $x \approx -2$, and the slope shows no significant change at different redshifts up to $z = 0.6$. I also study the distribution of the lobe pressure. The peak shifts to a higher value at higher redshift up to $z = 1.2$. This shift arises from my assumption of conditions inside the lobes close to those expected from the minimum energy requirement. It does not depend on other details of my model.

Chapter 4

A relativistic mixing-layer model for jets in low-luminosity FR I radio galaxies

In the last chapter, I studied the cosmological evolution for FR II sources, but excluded the FR I sources. The main reason for this was that currently there is no successful model describing FR I sources and their evolution. In this chapter, I will present an analytical model describing the steady state jets in FR I radio galaxies.

4.1 Previous work

Over the last few years, detailed modelling of deep VLA observations of jets in five FR I sources has allowed us to quantify their geometries, velocity distributions, magnetic fields and emissivity distributions in three dimensions. Below, I will refer in detail to the analysis of 3C 31 by Laing & Bridle (2002b, hereafter LB02a), but observations and models of a further four sources have also subsequently been published (Canvin & Laing, 2004; Canvin et al., 2005; Laing et al., 2006). A consistent picture of FR I jet deceleration on kiloparsec scales has emerged from these studies. The flow velocities are $\beta = v/c \approx 0.8 - 0.9$ where the jets first brighten abruptly, typically at ∼1 kpc from the nucleus. The jets flare and then recollimate, decelerating rapidly to speeds of $\beta \approx 0.1 - 0.4$. The best-fitting transverse velocity profiles appear to be approximately self-similar. At least in the 4/5 cases where the jets appear to be propagating in contact with the interstellar medium of the host galaxy, rather than inside radio lobes, they are roughly 30% faster on-axis than at their edges. Nevertheless, an evolution of the velocity profiles with distance from the nucleus is not excluded. In particular, the transverse velocity variations are poorly constrained where the jets first brighten abruptly, and a top-hat profile would also be consistent with the observations in these regions of all five sources.

In order to decelerate, a jet must entrain matter, either from stars within its volume (Phinney, 1983; Komissarov, 1994) or by ingestion of the surrounding material at its boundary, as originally suggested by Baan (1980), De Young (1981) and Begelman (1982). In the latter case, the transverse velocity profile almost inevitably evolves with distance from the nucleus.

X-ray observations can be used to infer the temperature, density and pressure profiles of the hot gas associated with the host galaxies of FR I radio galaxies (e.g. Hardcastle et al., 2002; Worrall et al., 2003; Hardcastle et al., 2005). Together with the velocity distributions derived from modelling of the radio emission, these can be used in a conservation-law analysis (Bicknell, 1994, hereafter B94) to derive jet energy fluxes and the variations of mass flux, pressure, internal density and entrainment rate with distance from the nucleus (Laing & Bridle, 2002a, hereafter LB02b). Such an analysis is quasi-one-dimensional and therefore adopts values for the flow variables (in particular the velocity) averaged across the jet cross-section. This is reasonable if the velocity profiles have restricted ranges and do not evolve significantly with distance down the jets, as is consistent with the observations of 3C 31 (LB02b). If FR I jets are in pressure equilibrium with their surroundings after they recollimate, this analysis requires that a significant overpressure drives the initial flaring.

An alternative approach, which would also be consistent with the observations, is to postulate that the transverse velocity profiles evolve significantly as the jets interact with the external medium. The first approximation is then to assume pressure equilibrium between the jet and its surroundings and to take explicit account of the interaction between the jets and their surroundings using a simple mixing-layer model. Such a model is the subject of the present chapter. The key assumption is that there is a turbulent mixing layer between the jet and its environment, produced by the interaction of the two components. The mixing layer grows both into the jet and into the environment, and the initially laminar jet eventually becomes fully turbulent. As in the quasi-one-dimensional analysis of Laing & Bridle (2002a), I use the relativistic formulation of the laws of conservation of mass, momentum and energy given by B94.

In this chapter, I first describe the geometry of the jet-layer model in Section 4.2. The relativistic conservation laws are introduced in Section 4.3. I derive and discuss the solutions for the model in Section 4.4. In Section 4.5, I apply the model to observations of 3C 31. I finally discuss the effects of varying model parameters in Section 4.6 and summarize the main conclusions in Section 4.7. The work in this Chapter has been published in Wang et al. (2009, hereafter W09)

4.2 Structure of an FR I jet

The basic structure of an FR I jet in my model is shown in Figure 5.1. Following the definition given by LB02a, I divide the jet into *flaring* and *outer* regions.[1] Close to the nucleus in the flaring region, the outer isophotes have small, but increasing opening angles. Further out, they spread rapidly and then recollimate. In the outer region, the expansion is conical. The radio emission close to the base of the flaring region is usually faint, and it is always possible to identify a distance from the nucleus where the jet brightens abruptly. I will refer to this location as the *brightening point*[2].

[1]LB02a postulated the existence of an additional conical inner region in the faint inner jets of 3C 31, but observations of the better-resolved source NGC 315 by Canvin et al. (2005) are inconsistent with a constant expansion rate in the corresponding part of the brighter jet. A continuously increasing expansion rate is required in NGC 315 and is equally consistent with the observations of 3C 31 and other sources. A two-zone model is adequate to describe the geometry in all cases.

[2]This is also a change of terminology from LB02a, who refer to the *flaring point*, and is adopted to emphasise that the location marks a change in emissivity profile, not in geometry.

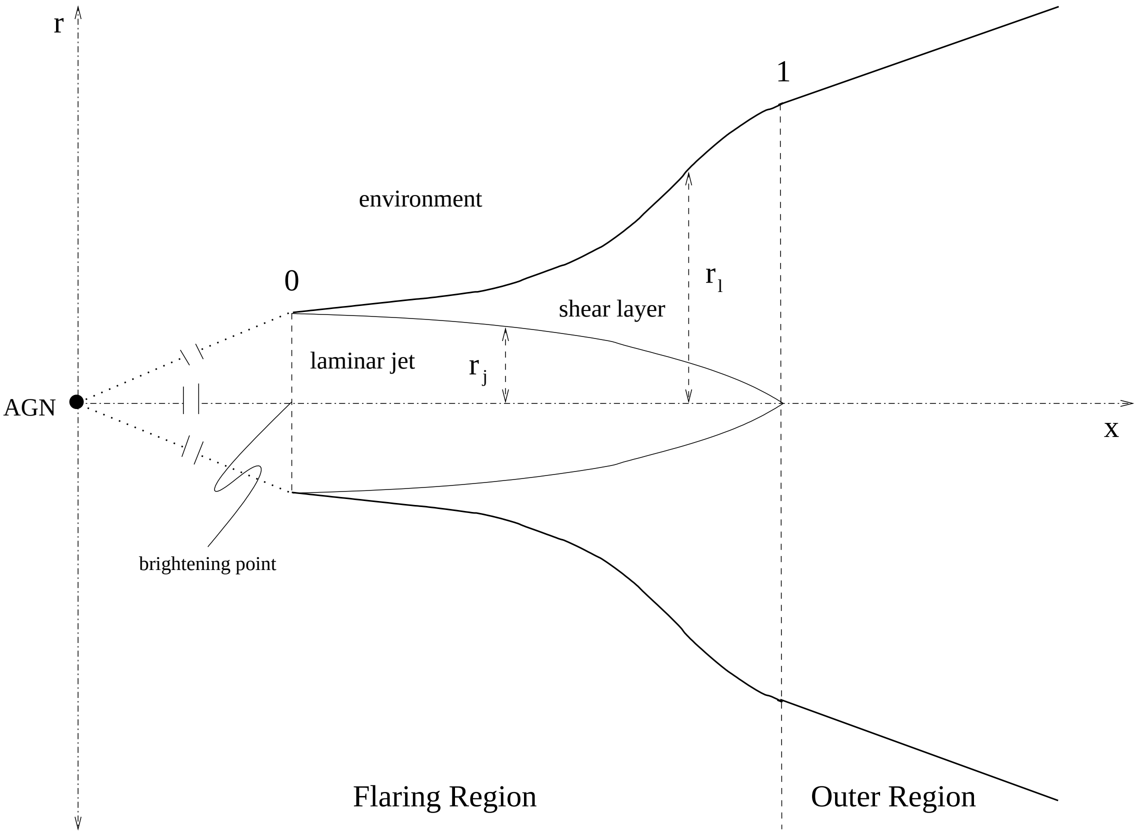

Figure 4.1: A sketch of the principal features of my jet model (not to scale). For comparison with later figures, the brightening point in 3C 31 is 1.1 kpc from the nucleus and the transition between the flaring and outer regions is at 3.5 kpc (see Fig. 4.3a)

I assume pressure equilibrium with the surroundings at all distances from the nucleus and adopt the simplest possible prescription for velocity variations following Canto & Raga (1991). Wherever possible, I approximate the velocity of a component of the flow by its spatially averaged value. I postulate that the flow close to the axis of the flaring region is laminar, with a constant relativistic bulk velocity v_j, and that this occupies the full width of the jet at the brightening point, where interaction with the external medium becomes significant for the first time. As a result of entrainment of external material, a slower *shear layer* forms between the laminar jet and the environment. The steady-state flow in this layer has a constant bulk velocity $v_l < v_j$. Material from both the environment and the laminar jet is continuously injected into the shear layer, the latter component supplying energy and momentum as well as mass. Integrated across the jet, the fraction of slower material then increases with distance from the nucleus; this would be interpreted as deceleration of the entire flow in fits to observations with poor transverse resolution.

The laminar region of the jet in the centre is getting smaller when the jet propagates further and eventually vanishes after certain distance, so no more energy or momentum can be injected into the shear layer from the inside beyond this point. Motivated by the analysis of 3C 31 (LB02a), I assume that this transition occurs precisely at the end of the flaring region. This may not be general: modeling of other sources suggests that the bulk of the jet deceleration occurs in the first part of the flaring region (e.g. NGC 315; Canvin et al. 2005). I assume that the boundary of the shear layer in the outer region expands smoothly and more slowly as the environmental pressure decreases. Entrainment from the environment into the shear layer can still happen in the outer region, but this requires that the velocity be allowed to vary along the jet (Section 4.3.2). Precisely speaking, all parameters could have a transverse gradient. However, as I have divide the jet into different regions, I simply assume that in my model here, there is no transverse gradient in each region for all physical parameters.

The following convention is adopted throughout this chapter: I use subscript 0 for quantities at the brightening point; 1 for quantities at the end of the flaring region; j, l and e for all quantities related to the laminar jet, shear layer and environment, respectively. Detailed descriptions of the parameters are given in Fig. 4.1 and Table 4.1.

4.3 Relativistic conservation laws

I model the structure of FR I jets using relativistic fluid mechanics, applying the laws of conservation of mass, momentum and energy in the forms given by B94. As in that reference, I use the relativistic enthalpy, $\omega = \rho c^2 + \epsilon + p$, and the ratio $\mathscr{R} = \rho c^2/(\epsilon + p)$ of rest-mass energy to non-relativistic enthalpy. Here, ϵ is the internal energy density, and p is the pressure. The advantage of using enthalpy is that I can consider ρ and p as a whole, so that the total number of unknown parameters is reduced. In keeping with the assumption that physical parameters do not change throughout the flaring region, I assume that $\mathscr{R}_j$ is constant.

Name	Physical meaning	Flaring region value	Flaring region origin	Outer region value	Outer region origin
Γ_j	adiabatic index of the laminar jet	4/3, constant	assumed	-	-
Γ_l	adiabatic index of the shear layer	4/3, constant	assumed	4/3, constant	assumed
Γ_e	adiabatic index of the environment	5/3, constant	assumed	5/3, constant	assumed
β_j	bulk velocity of the laminar jet	constant	Radio	-	-
β_l	bulk velocity of the shear layer	constant	Radio	function of x	calculated
β_1	the bulk velocity at the beginning point of the outer region	-	-	constant	Radio
$\mathscr{R}_j$	ratio of rest mass energy to non-relativistic enthalpy for laminar jet	constant	calculated	-	-
$\mathscr{R}_l$	ratio of rest mass energy to non-relativistic enthalpy for shear layer	function of x	calculated	function of x	calculated
$\mathscr{R}_1$	the value of $\mathscr{R}_l$ on the cross section 1	-	-	constant	calculated
p	external pressure on cross section x	function of x	X-ray	function of x	X-ray
r_j	the radius of the laminar jet	function of x	calculated	-	-
r_l	the radius of the shear layer	function of x	Radio	function of x	Radio
r_0	the jet radius at the brightening point	constant	Radio	-	-
r_1	the shear layer radius at the beginning point of the outer region	-	-	constant	Radio
$g_{\rm f}$	entrained mass per time from cross section 0 up to cross section x	function of x	calculated	-	-
$g_{\rm o}$	entrained mass per time from cross section 1 up to cross section x	-	-	function of x	calculated

Table 4.1: Definitions of key parameters and functions. Columns 4 and 6 indicate whether the values are assumed a priori, inferred from fits of relativistic flow models to radio images (‘Radio’), derived from X-ray observations of the surrounding hot gas (‘X-ray’) or calculated.

For an ideal gas, $\epsilon = p/(\Gamma - 1)$, so $\mathscr{R}$ can be written as:

$$\mathscr{R} = \frac{\Gamma - 1}{\Gamma}\frac{\rho c^2}{p} = \frac{\Gamma - 1}{\Gamma}\frac{\widehat{m}c^2}{k_B T}, \tag{4.1}$$

where Γ is the adiabatic index, $\widehat{m}$ is the average particle mass and k_B is the Boltzmann constant. $\mathscr{R}^{-1}$ is therefore a measure of the temperature. I make the approximation that the external medium around the jet is isothermal, so $\mathscr{R}_e$ is constant. There is evidence for a temperature gradient on the relevant scales (Hardcastle et al., 2002), but the isothermal approximation has a very small effect on my results, since the energy entrained from the external medium is negligible (B94, LB02b) and $\mathscr{R}_e \gg 1$ (Section 4.3.1.3).

4.3.1 Conservation laws for the flaring region

The main difference between my work and that of B94 and LB02b is that I divide the flaring region into two parts: the laminar jet and the shear layer. Thus my conservation equations include distinct terms associated with each of these components.

4.3.1.1 Conservation of rest mass

The rest mass of the material passing through the total jet cross section $A(x) = \pi r_l(x)^2$ per unit time is equal to the rest mass of the material entering through the cross section 0 plus the total entrained mass from the environment. I express the mass fluxes in the laminar jet and the shear layer at distance x separately by:

$$\dot{M}_j(x) = \gamma_j \rho_j(x) v_j \pi r_j(x)^2 \tag{4.2}$$

$$\dot{M}_l(x) = \gamma_l \rho_l(x) v_l \pi \left[r_l(x)^2 - r_j(x)^2 \right] \tag{4.3}$$

From equation (9) of B94,I have

$$\gamma_j \rho_{j,0} v_j \pi r_0^2 + \int_0^x \rho_e(x') f(x') dx' = \dot{M}_j(x) + \dot{M}_l(x) \tag{4.4}$$

where ρ is the proper density, v is the bulk velocity, $\beta = v/c$ and $\gamma = (1 - \beta^2)^{-1/2}$ is the bulk Lorentz factor. r_j and r_l are the radii of the laminar jet and the shear layer, respectively. The first term on the left of equation (4.4) is the rest mass of the material entering through cross section 0 per unit time. The second term on the left is the entrained mass flux. The terms on the right represent the rest masses of the material passing through the cross sections of the laminar jet and the shear layer per unit time at distance x. I assume that the laminar jet continuously supplies energy and momentum to the shear layer in such a way that β_j and β_l remain constant throughout the flaring region. The integral term $g_{\mathrm{f}}(x) = \int_{x_0}^{x} \rho_e(x') f(x') dx'$ is the mass entrainment function, which was given in the form $g_{\mathrm{f}}(x) = \int_S \rho \boldsymbol{v}_{\mathbf{ent}} \cdot \boldsymbol{n}\, dS$ by B94 ($\boldsymbol{n}$ is the normal direction of the unit surface dS). The function $f(x)$ therefore expresses the combination of the perpendicular entrainment velocity and the shape of the jet boundary. The function $g_{\mathrm{f}}(x)$ is a measure of the total mass entrained between the nucleus and distance x per unit time.

I assume that the jet is in pressure equilibrium with the external medium throughout the flaring and outer regions. Thus at fixed x, the pressures in the laminar jet, the shear layer and the environment are all equal. Dividing by $p(x)$ on both sides of equation (4.4), I find,

$$\frac{\mathscr{R}_j\Gamma_j}{\Gamma_j-1}\gamma_j\beta_j\left[\frac{p_0}{p(x)}r_0^2-r_j(x)^2\right]=\frac{\mathscr{R}_l(x)\Gamma_l}{\Gamma_l-1}\gamma_l\beta_l\left[r_l(x)^2-r_j(x)^2\right]-F_{\rm f}(x), \tag{4.5}$$

where $F_{\rm f}(x)=cg_{\rm f}(x)/\left[\pi p(x)\right]$.

4.3.1.2 Conservation of momentum

The momentum flow through the cross section $A(x)$ per unit time should be equal to the momentum of the material coming out of the initial cross section 0 per unit time, modified by the effects of buoyancy and differences in pressure between the flow and its environment. I express the momentum flux by:

$$\dot{P}_j(x)=\left[\gamma_j^2\frac{\omega_j(x)}{c^2}v_j^2+\Delta p_{j,l}(x)\right]\pi r_j(x)^2, \tag{4.6}$$

$$\dot{P}_l(x)=\left[\gamma_l^2\frac{\omega_l(x)}{c^2}v_l^2+\Delta p_{l,e}(x)\right]\pi\left[r_l(x)^2-r_j(x)^2\right], \tag{4.7}$$

where $\Delta p_{j,l}(x)=p_j(x)-p_l(x)$ and $\Delta p_{l,e}(x)=p_l(x)-p_e(x)$ are the pressure differences at distance x. In the pressure-matched case, they are all equal to 0. I assume that material is entrained from the environment with a small bulk velocity and therefore that it contributes negligible momentum compared with that of the jet. I thus rewrite equation (16) in B94 for this case as:

$$\gamma_j^2\frac{\omega_{j,0}}{c^2}v_j^2\pi r_0^2=\dot{P}_j(x)+\dot{P}_l(x)+\phi(x), \tag{4.8}$$

where $\phi(x)=\int_{x_0}^{x}dx'\left[\frac{dp_e}{dx'}\int_A(1-\frac{\rho_j}{\rho_e})dS\right]$ is the buoyancy term which, with $\rho_j\ll\rho_e$ in my model, simplifies to $\phi(x)=\int_{x_0}^{x}\pi r_l(x')^2dp$. The momentum equation can then also be simplified to:

$$\frac{(\mathscr{R}_j+1)\Gamma_j}{\Gamma_j-1}\gamma_j^2\beta_j^2\left[\frac{p_0}{p(x)}r_0^2-r_j(x)^2\right]=\frac{(\mathscr{R}_l(x)+1)\Gamma_l}{\Gamma_l-1}\gamma_l^2\beta_l^2\left[r_l(x)^2-r_j(x)^2\right]+\frac{\phi(x)}{\pi p(x)}. \tag{4.9}$$

4.3.1.3 Conservation of energy

The energy passing through the jet cross section must also be conserved. I express the energy flux (or jet power) at distance x for the two regions as:

$$Q_j(x) = \gamma_j^2 \omega_j(x) v_j \pi r_j(x)^2, \tag{4.10}$$

$$Q_l(x) = \gamma_l^2 \omega_l(x) v_l \pi \left[r_l(x)^2 - r_j(x)^2 \right]. \tag{4.11}$$

B94 gives the relevant conservation law in his equation (26), and I rewrite this as:

$$\gamma_j^2 \omega_{j,0} v_j \pi r_0^2 + \int_{x_0}^{x} \omega_e(x') f(x') dx' = Q_j(x) + Q_l(x). \tag{4.12}$$

As the environment is dominated by the rest mass energy, so $\mathscr{R}_e$ is extremely large, and I can approximate $1 + 1/\mathscr{R}_e \approx 1$ at all positions. Thus,

$$\int_{x_0}^{x} \omega_e(x') f(x') dx' = \int_{x_0}^{x} c^2 \left[1 + 1/\mathscr{R}_e(x') \right] f(x') dx' \approx c^2 g_{\mathrm{f}}(x). \tag{4.13}$$

Dividing both sides by $p(x)$, I get:

$$\frac{(\mathscr{R}_j + 1)\Gamma_j}{\Gamma_j - 1} \gamma_j^2 \beta_j \left[\frac{p_0}{p(x)} r_0^2 - r_j(x)^2 \right] = \frac{\left[\mathscr{R}_l(x) + 1\right] \Gamma_l}{\Gamma_l - 1} \gamma_l^2 \beta_l \left[r_l(x)^2 - r_j(x)^2 \right] - F_{\mathrm{f}}(x). \tag{4.14}$$

4.3.2 Conservation laws for the outer region

For the outer region, the conservation equations are similar, but without the laminar jet term. Another important difference is that the initial cross section is now at the end of the flaring region (point 1 in Fig. 5.1). The entrained mass and energy now denote the values integrated from point 1 (distance x_1) up to distance x. Finally, the velocity of the layer, β_l, is a function of distance x. The three equations analogous to equations (4.4), (4.8), and (4.12) are then given by

$$\gamma_1 \rho_1 v_1 \pi r_1^2 = \dot{M}_l(x) - g_{\mathrm{o}}(x), \tag{4.15}$$

$$\gamma_1^2 \frac{\omega_1}{c^2} v_1^2 \pi r_1^2 = \dot{P}_l(x) + \phi(x), \tag{4.16}$$

$$\gamma_1^2 \omega_1 v_1 \pi r_1^2 = Q_l(x) - \int_{x_1}^{x} \omega_e(x') f(x') dx'. \tag{4.17}$$

The term $g_{\rm o}(x) = \int_{x1}^{x} \rho_e(x')f(x')dx'$ is equal to the amount of entrained mass per unit time. With the same definitions of $F(x)$ and R as given above, these three equations can be written in the following ways

$$\frac{\Gamma_l \gamma_1 \beta_1}{\Gamma_l - 1}\frac{p_1 r_1^2}{p(x)} = \frac{\Gamma_l}{\Gamma_l - 1}\frac{\mathscr{R}_l(x)}{\mathscr{R}_1}\gamma_l(x)\beta_l(x)r_l(x)^2 - \frac{F_{\rm o}(x)}{\mathscr{R}_1}, \tag{4.18}$$

$$\frac{\Gamma_l \gamma_1^2 \beta_1^2}{\Gamma_l - 1}\frac{p_1 r_1^2}{p(x)} = \frac{\Gamma_l}{\Gamma_l - 1}\frac{\mathscr{R}_l(x)+1}{\mathscr{R}_1+1}\gamma_l(x)^2\beta_l(x)^2 r_l(x)^2 + \frac{1}{\mathscr{R}_1+1}\frac{\phi(x)}{\pi p(x)}, \tag{4.19}$$

$$\frac{\Gamma_l \gamma_1^2 \beta_1}{\Gamma_l - 1}\frac{p_1 r_1^2}{p(x)} = \frac{\Gamma_l}{\Gamma_l - 1}\frac{\mathscr{R}_l(x)+1}{\mathscr{R}_1+1}\gamma_l(x)^2\beta_l(x)r_l(x)^2 - \frac{F_{\rm o}(x)}{\mathscr{R}_1+1}. \tag{4.20}$$

4.4 Solutions

In this section, I will solve equations (4.5), (4.9), (4.14) for the flaring region, and equations (4.18), (4.19), (4.20) for the outer region in terms of quantities which can be inferred either from fits of relativistic flow models to radio images (jet and layer velocities in the flaring region, together with the radius of the layer in both regions) or from X-ray observations of the surrounding hot gas (external density, temperature and pressure). I can then derive the shape of the laminar jet, $r_j(x)$, the variation of velocity with distance in the outer region, $\beta_l(x)$, the values of $\mathscr{R}$ in the various regions, the entrainment function and the velocity of entrainment.

I assume that the laminar jet has a relativistic equation of state with $\Gamma_j = 4/3$; the environment has $\Gamma_e = 5/3$. The shear layer contains mixed material, but the energy density must still be dominated by relativistic particles (B94), and I therefore take $\Gamma_l = 4/3$.

4.4.1 Solutions for the flaring region

From equations (4.5) and (4.14), I obtain:

$$\frac{r_l(x)^2 - r_j(x)^2}{\frac{p_0}{p(x)}r_0^2 - r_j(x)^2} = \frac{\frac{\Gamma_j}{\Gamma_j - 1}\gamma_j\beta_j\left[\mathscr{R}_j - (\mathscr{R}_j+1)\gamma_j\right]}{\frac{\Gamma_l}{\Gamma_l - 1}\gamma_l\beta_l\{\mathscr{R}_l(x) - \left[\mathscr{R}_l(x)+1\right]\gamma_l\}}. \tag{4.21}$$

At the same time, from equation (4.9), I find:

$$\frac{r_l(x)^2 - r_j(x)^2}{\frac{p_0}{p(x)}r_0^2 - r_j(x)^2} = \frac{\frac{\Gamma_j}{\Gamma_j - 1}(\mathscr{R}_j+1)\gamma_j^2\beta_j^2 - \frac{\phi(x)}{p(x)r_l(x)^2 - p_0 r_0^2}}{\frac{\Gamma_l}{\Gamma_l - 1}\left[(\mathscr{R}_l(x)+1\right]\gamma_l^2\beta_l^2 - \frac{\phi(x)}{p(x)r_l(x)^2 - p_0 r_0^2}}. \tag{4.22}$$

Thus, I can express $\mathscr{R}_l$ as a function of $\mathscr{R}_j$, β_j, β_l and the buoyancy term, $\phi(x)$, which can be calculated from the pressure profile and the shape of the jet $r_l(x)$:

$$\mathscr{R}_l(x) = \frac{C(x) + B(x)\gamma_l}{D(x) - A\gamma_l\beta_l}, \tag{4.23}$$

where

$$A = \mathscr{R}_j - (\mathscr{R}_j + 1)\gamma_j, \tag{4.24}$$

$$B(x) = (R_j+1)\gamma_j\beta_j + \frac{\Gamma_j - 1}{\Gamma_j\gamma_j\beta_j}\frac{\phi(x)}{p(x)\pi r_l(x)^2 - p_0\pi r_0^2}, \tag{4.25}$$

$$C(x) = A\left[\gamma_l\beta_l + \frac{\Gamma_l - 1}{\Gamma_l\gamma_l\beta_l}\frac{\phi(x)}{p(x)\pi r_l(x)^2 - p_0\pi r_0^2}\right], \tag{4.26}$$

$$D(x) = B(x)(1-\gamma_l). \tag{4.27}$$

Also, from equations (4.5) and (4.22), I can express the shape of the laminar jet and the entrainment function by:

$$r_j(x)^2 = \frac{p_0 r_0^2}{p(x)} - \frac{r_l(x)^2\{\dot{P}_l(x)\left[\frac{p_0 r_0^2}{p(x)r_l(x)^2} - 1\right] + \tau(x)\phi(x)\}}{\dot{P}_l(x) - \dot{P}_j(x)\frac{\tau(x)}{\kappa(x)}}, \tag{4.28}$$

$$g_{\mathrm{f}}(x) = \frac{\left[1 - \frac{p_0 r_0^2}{p(x)r_l(x)^2}\right](\beta_j - \beta_l) + c\phi(x)\left[\frac{\kappa(x)}{Q_j(x)} - \frac{\tau(x)}{Q_l(x)}\right]}{c^2\left[\frac{\beta_j\tau(x)}{Q_l(x)} - \frac{\beta_l\kappa(x)}{Q_j(x)}\right]}, \tag{4.29}$$

where $\kappa(x) = [r_j(x)/r_l(x)]^2$ and $\tau(x) = 1 - \kappa(x)$ are the fractions of jet and shear layer, respectively, at distance x. Although the expressions for $\dot{P}_l(x)$ and $\dot{P}_j(x)$ contain $r_j(x)$ [equation (4.28)], $\dot{P}_l(x)/\tau(x)$ and $\dot{P}_j(x)/\kappa(x)$ are functions only of observable parameters together with $\mathscr{R}_l(x)$ and $\mathscr{R}_j$. By applying the boundary condition $r_j(x_1) = 0$, I can derive

$\mathscr{R}_j$ and then solve for $\mathscr{R}_l(x)$ from equation (4.23) given the shape of the outer boundary of the shear layer, $r_l(x)$. Finally, I can determine the shape of the laminar jet boundary, and the function $F(x)$, which can then be used to calculate the entrainment function.

4.4.2 Solutions for the outer region

In the outer region, there is no laminar jet to supply energy to the shear layer, but matter continues to be entrained from the environment. Thus both β_l and $\mathscr{R}_l$ are expected to be functions of x. I solve the equations numerically, using the following steps. Equations (4.18) and (4.20) give:

$$\mathscr{R}_l(x) = \frac{\frac{\dot{M}_1 \mathscr{R}_l(x)}{\dot{M}_l(x)\mathscr{R}_1}\left[\mathscr{R}_1(\gamma_1 - 1) + \gamma_1\right] - \gamma_l(x)}{\gamma_l(x) - 1}, \tag{4.30}$$

while equation (4.19) gives:

$$\mathscr{R}_l(x) = \frac{\Gamma_l - 1}{\Gamma_l}\frac{\dot{P}_1 - \pi p(x)\phi(x)}{\dot{P}_l(x)/\left[\mathscr{R}_l(x) + 1\right]} - 1. \tag{4.31}$$

Again, $\mathscr{R}_l(x)$ occurs on the right-hand sides of equation (4.30) and (4.31), but $\dot{M}_l(x)/\mathscr{R}_l(x)$ and $\dot{P}_l(x)/[\mathscr{R}_l(x) + 1]$ are just functions of $\beta_l(x)$ and other observable parameters. Combining these two equations, I can solve numerically for the value of $\beta_l(x)$: the shape of the boundary, $r_l(x)$, is constrained from observations, so the only unknown parameters are $\beta_l(x)$, which in turn determines $\gamma_l(x)$. Then, with the known value of $\beta_l(x)$, I can express the entrainment function as:

$$g_{\mathrm{o}}(x) = \frac{\dot{M}_1}{\mathscr{R}_1}\frac{\gamma_1(\mathscr{R}_1 + 1) - \left[\frac{\dot{M}_1 \mathscr{R}_l(x)}{\dot{M}_l(x)\mathscr{R}_1} + 1\right]\gamma_l(x)}{\gamma_l(x) - 1}. \tag{4.32}$$

Observations show that the radius of the shear layer in the outer region $r_l(x)$ increases linearly with x. I use this observed variation as input to the model and predict the resulting distributions of $\beta_l(x)$, $\mathscr{R}_l(x)$ and $g_{\mathrm{o}}(x)$

4.4.3 Summary of the solutions

In order to find solutions for both the flaring region and the outer region, I adopt the shape function $r_l(x)$ from model-fitting to radio images, together with the velocities β_l

and β_j for the flaring region. I also adopt the pressure profiles from X-ray observations. This leaves three functions which need to be evaluated at each distance x: $r_j(x)$, $F(x)$ and $\mathscr{R}_l(x)$ for the flaring region, and $\beta_l(x)$, $\mathscr{R}_l(x)$ and $F(x)$ for the outer region.

The three equations from the conservation laws thus form a closed system. The input and derived parameters are listed in Table 4.1.

4.5 Application to 3C 31

Having established a system of equations which describe the structure and kinematics of an FR I jet, I now compare the results with observational data and models for the well-observed source 3C 31. Geometrical (projection factor and radius) and velocity information are inferred from the relativistic-flow models of LB02a. Fits to the density, temperature and pressure of the hot gas surrounding the jets are as given by Hardcastle et al. (2002) and used in the quasi-one-dimensional conservation-law analysis of LB02b. For the Hubble constant and concordance cosmology I adopt, at the redshift of the host galaxy of 3C 31, $z = 0.0169$, this gives a scale of $0.344\,\mathrm{kpc\,arcsec^{-1}}$.

4.5.1 Inferences from observation

The parameters defining the edge of the shear layer projected on the sky are determined by fitting to the total-intensity distribution. The angle to the line of sight required to correct for projection (52° for 3C 31) is derived from the relativistic-flow model. In LB02a, the shape of the shear layer in the flaring region is described by the polynomial $r_l(x) = a + bx + cx^2 + dx^3$ with $r_0 = 0.125\,\mathrm{kpc}$ at $1.1\,\mathrm{kpc}$ and $r_1 = 0.815\,\mathrm{kpc}$ at $3.5\,\mathrm{kpc}$. The shear layer initially expands slowly, then goes through a phase of faster expansion before recollimating at the end of the flaring region. In the outer region, the shear layer expands conically, with an intrinsic half-angle of 13.1°. I also assume that there is no shear layer at the beginning of the flaring region, so I use the on-axis bulk velocity inferred by LB02a to characterize the jet, $v_j = 0.77c$. I suppose that the shear layer makes up essentially all of the flow at the end of the flaring region. LB02a infer a variation of velocity across the flow from $0.37c - 0.55c$ at this distance, so I take a representative value of $v_l = 0.45c$.

Hardcastle et al. (2002) have estimated the external density and pressure profiles for 3C 31 from X-ray observations. The density profile is given by:

$$\rho_e(x) = m_p n_e(x)/\chi_H, \tag{4.33}$$

where m_p is the mass of a proton, $\chi_H = 0.74$ is the abundance of hydrogen by mass and $n_e(x)$ is the proton number density of the environment given by:

$$n_e(x) = n_c(1 + x^2/x_c^2)^{-3\beta_c/2} + n_g(1 + x^2/x_g^2)^{-3\beta_g/2}. \tag{4.34}$$

The numerical values of the parameters are: $n_c = 1.8 \times 10^5\,\mathrm{m}^{-3}$, $n_g = 1.9 \times 10^3\,\mathrm{m}^{-3}$, $\beta_c = 0.73$, $\beta_g = 0.38$, $x_c = 1.2\,\mathrm{kpc}$, $x_g = 52\,\mathrm{kpc}$. The temperatures estimated by Hardcastle et al. (2002) range from $4.9 \times 10^6\,\mathrm{K}$ to $1.7 \times 10^7\,\mathrm{K}$, corresponding to $\mathscr{R}_e = 5 \times 10^5$ to 1.5×10^5. Thus the approximation $1 + 1/\mathscr{R}_e \approx 1$ (Section 3.1.3) is valid to high accuracy. The pressure is given by Birkinshaw & Worrall (1993):

$$p(x) = kT(x)n_e(x)/(\mu\chi_H), \tag{4.35}$$

where $\mu = 0.6$ is the mass per particle. For simplicity, I approximate the pressure and density distributions using power-law forms:

$$\rho_e(x) = \rho_{e,0}(\frac{x}{x_0})^{-\alpha_1}, \tag{4.36}$$

$$p(x) = p_0(\frac{x}{x_0})^{-\alpha_2}, \tag{4.37}$$

where x_0 is the position of the brightening point. $\rho_{e,0} = 2.16 \times 10^{-22}\,\mathrm{kg\,m}^{-3}$ and $p_0 = 1.93 \times 10^{-11}\,\mathrm{Pa}$ are the density and pressure at x_0, respectively. The values $\alpha_1 = 1.5$ and $\alpha_2 = 1.1$ give good approximations to the profiles, and I adopt them in the following calculations. The corresponding density and the pressure profiles are compared with those from Hardcastle et al. (2002) in Figure 4.2. Although I use an isothermal approximation in the development of my model (Section 4.3), the assumed pressure profile includes the effects of the temperature gradient.

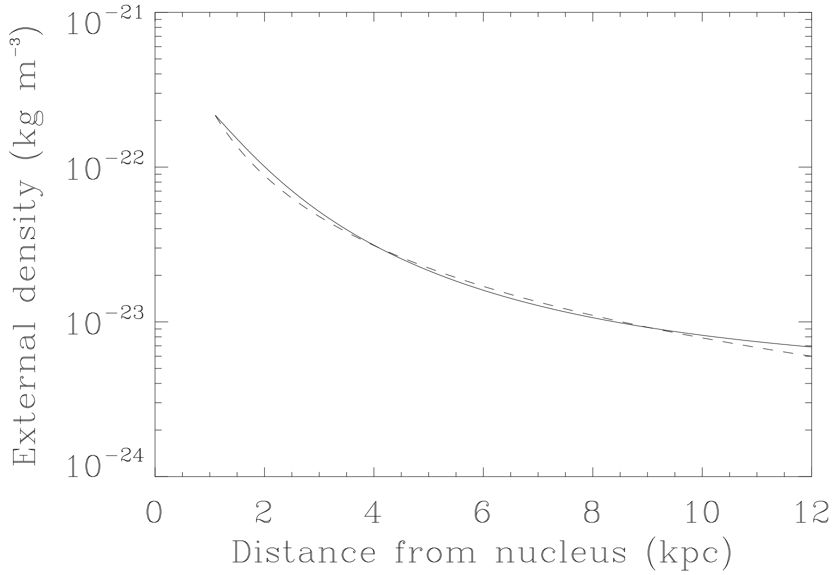

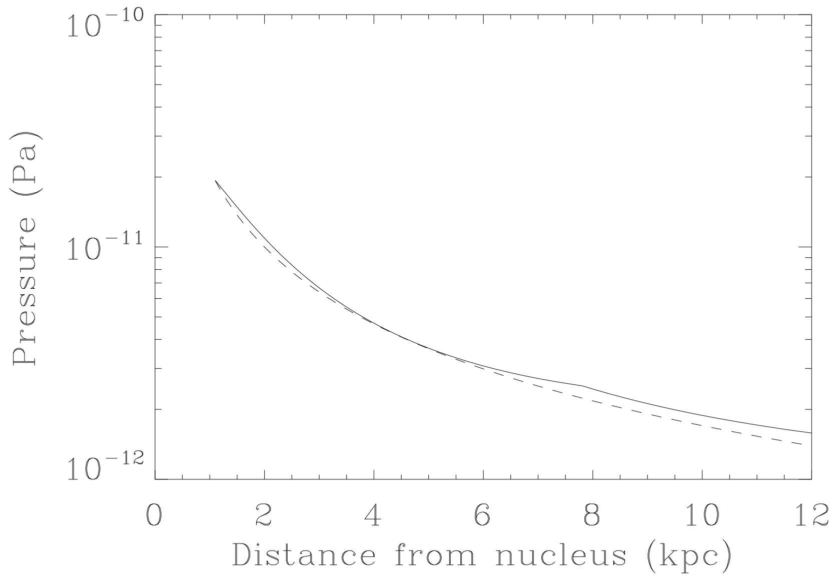

Figure 4.2: The external density and pressure profiles for 3C 31. The solid lines are derived from the double-beta-model fit to the number density and pressure [equations (4.34) and (4.35)] while the dashed lines are power-law approximations with indices of $\alpha_1 = 1.5$ and $\alpha_2 = 1.1$, as described in the text.

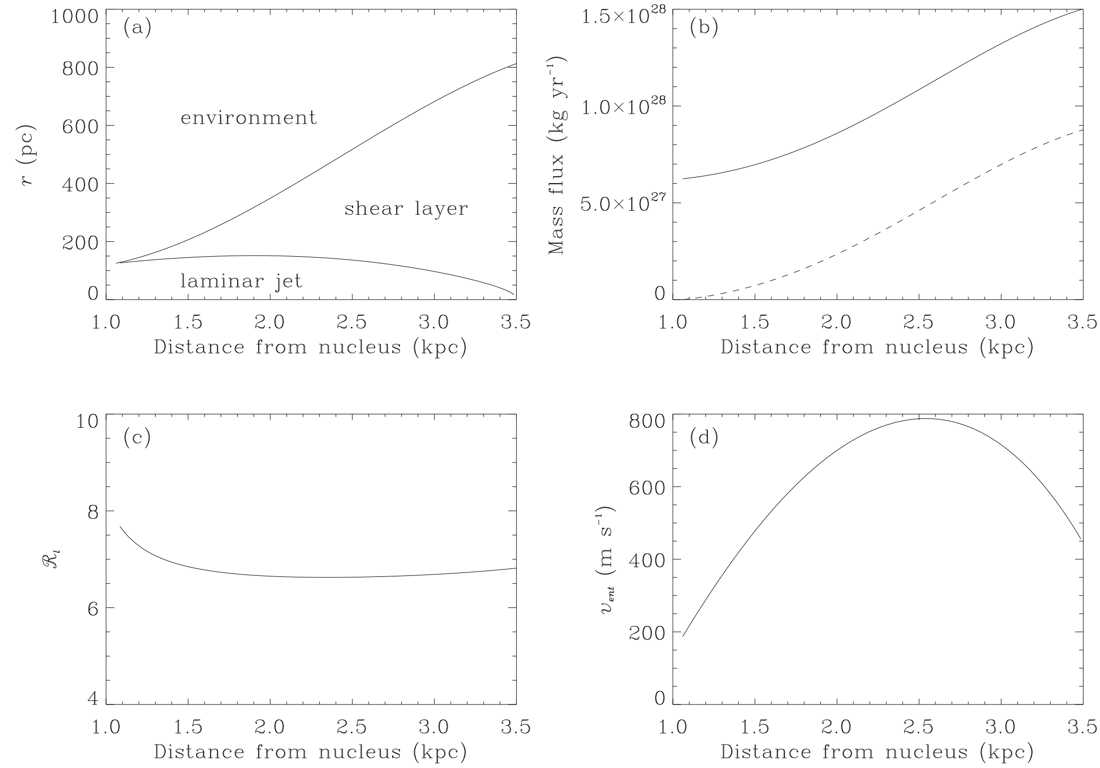

Figure 4.3: Results from my model for the flaring region of 3C 31. (a) Geometry. The outer edge of the flow and the boundary between the laminar core and shear layer are shown. (b) Mass flux at distance x. The full and dashed lines indicate the total mass flux and the contribution from entrainment, respectively. (c) Profile of $\mathscr{R}_l(x)$. (d) The entrainment velocity perpendicular to the outer boundary at distance x.

4.5.2 Results from the model

4.5.2.1 Flaring region

With the parameters given in Section 4.5.1, I obtain $\mathscr{R}_j = 13.4$ in the flaring region. The profiles of $\mathscr{R}_l(x)$ and the total mass flux passing through a given cross section, $\dot{M}$, are plotted in Figure 4.3. In the same figure, I also plot $v_{\rm ent}$, the normal component of the entrainment velocity across the surface of the jet. This is related to the entrainment function by $v_{\rm ent} = (1/\rho_e)dg/ds$.

The model predicts that the laminar jet initially expands at the beginning of the flaring

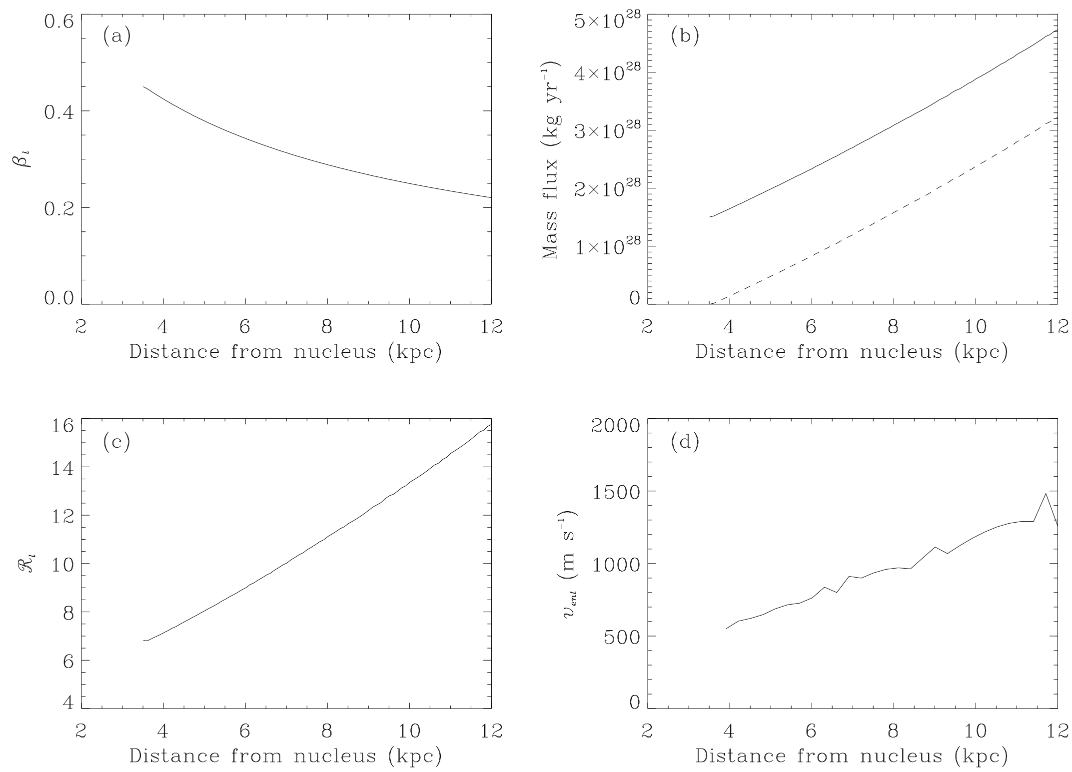

Figure 4.4: Results from my model for the outer region of 3C 31. (a) Profile of bulk velocity $\beta_l(x)$. (b) Mass flux $\dot{M}(x)$ at distance x. The full and dashed lines indicate the total mass flux and the contribution from entrainment, respectively. (c) Profile of $\mathscr{R}_l(x)$. (d) The entrainment velocity perpendicular to the outer boundary as a function of distance, x. The jagged shape of the profile is a numerical artefact, but the overall shape is correct.

region and then starts to collapse ≈1.7 kpc away from the brightening point. Meanwhile, the value of $\mathscr{R}_l(x)$ drops a little at the beginning of the flaring region and then reaches an asymptotic value of ≈6.7. The initial decrease of $\mathscr{R}_l(x)$ occurs because the small amount of entrained material at the beginning of the flaring region can easily be heated by the laminar jet. The functional forms of $\mathscr{R}_l(x)$ and $v_{\rm ent}(x)$ are constrained by the parameters inferred for 3C 31 and may differ in other sources. For example, if the shear layer initially expands faster, $R_l(x)$ will be higher and $v_{\rm ent}$ lower throughout the flaring region.

4.5.2.2 Outer region

In the outer region, my model predicts that the bulk velocity β_l should decrease smoothly with x. I find $\beta_l = 0.45$ at 3.5 kpc, where it is normalized to the mean value of the distribution derived by LB02a, decreasing to 0.22 at 12 kpc. This is reasonably consistent with the velocity range derived by LB02a ($\beta = 0.15 - 0.22$ at the same distance). The value of $\mathscr{R}_l$ increases with x in my solution, reflecting the increasing dominance of the mass by entrained material. I plot $\mathscr{R}_l(x)$ and $\beta_l(x)$ together with profiles of mass flux and velocity in Figure 4.4.

4.5.2.3 Estimate of jet power

Using the calculated and observed parameters given above, I can estimate the power of the jets in 3C 31. The relevant parameter for comparison with estimates by other methods (e.g. Bîrzan et al. 2008) is Φ (LB02b), the energy flux of the jet with the rest-mass contribution subtracted. $\Phi = Q - \dot{M}c^2$ in the notation of the present chapter. Applying equation (4.10) at the brightening point, I get values of $Q = 3.4 \times 10^{37}$ W and $\Phi = 1.6 \times 10^{37}$ W. The object 3C 31 is a fairly powerful FR I source, with a monochromatic luminosity of $10^{24.5}$ W at 1.4 GHz, approximately a factor of 10 below the FR I/FR II dividing line plotted by Ledlow & Owen (1996), given the absolute magnitude of its host galaxy (Owen & Laing, 1989). A total power of $\Phi = 1.6 \times 10^{37}$ W for the twin jets of 3C 31 is well within the range derived from observations of cavities in the X-ray gas surrounding other radio galaxies of comparable monochromatic luminosity (Bîrzan et al., 2008).

4.5.2.4 Mass input from stellar mass loss

It has been argued that the deceleration in the flaring region could be caused by the entrainment of stellar wind material from stars located inside the jet (Komissarov, 1994). In order to test this idea, I adopt the estimate of mass input from LB02b, who used a deprojection of R-band surface photometry for 3C 31 (Owen & Laing, 1989), together with the same assumptions on conversion between stellar luminosity and mass loss as in

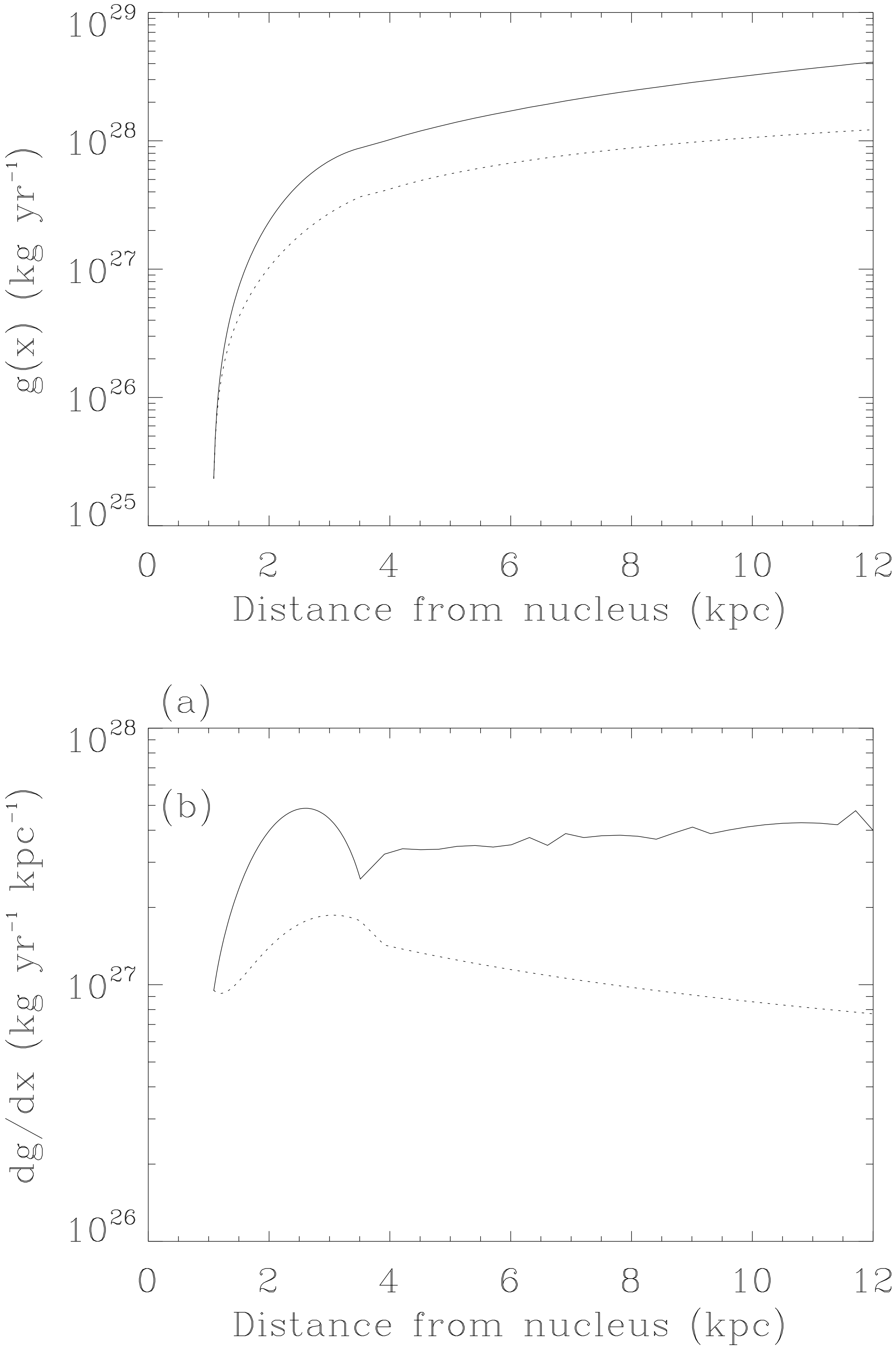

Figure 4.5: (a) The entrainment function, $g(x)$, from my model (full line) compared with the estimate from stellar mass loss within the jet, $g_{\rm s}(x)$ (dotted). (b) As in panel (a), but for the entrainment per unit length of the jet, dg/dx.

Komissarov (1994) and Bowman et al. (1996). The corresponding entrainment per unit length (the derivative of the entrainment function defined above) can be written as

$$dg_{\rm s}/dx = 2.4 \times 10^{28} \pi r_l(x)^2 x^{-2.65}\,{\rm kg\,kpc^{-1}\,yr^{-1}}, \tag{4.38}$$

where $r_l(x)$ and x are in units of kpc. In Fig. 4.5, I compare the entrainment function from my model and its derivative with those estimated for stellar mass loss. At the beginning of the flaring region, the stellar mass input rate is remarkably close to that required, given the crudity of the assumptions. At larger distances, however, it falls well below the level required to decelerate the jet. In the outer region, the entrainment rate per unit length required by my model continues to increase, whereas that from stellar mass loss decreases. Thus, although stellar mass loss may be important in initiating the jet deceleration at the start of the flaring region, boundary-layer entrainment, as described by my model, is clearly required on larger scales.

4.5.3 Comparison with LB02b

It is of interest to compare the results of the present model with the conservation-law analysis of LB02b. The treatments are very similar in many respects, both relying on quasi-one-dimensional approximations and using conservation of mass, momentum and energy in a realistic external environment. The formulation of the conservation laws is identical in the two treatments. The principal differences in the assumptions are as follows.

1. The analysis of LB02b explicitly assumed that there are no variations in physical parameters across the jets, as in my treatment of the outer region. By contrast, I split the flaring region into laminar jet and shear layer components.

2. The jets in LB02b's analysis are assumed to come into approximate pressure equilibrium with their surroundings only after they recollimate. This then requires that they are over-pressured at the start of the flaring region. However, I assume that the jets are everywhere in pressure equilibrium with the external medium. In this picture, the initial expansion is caused by transfer of momentum from the laminar core to the shear layer rather than a pressure-driven expansion.

3. The models are constrained in slightly different ways. Both specify the radius of the jet as a function of distance from the nucleus. In LB02b, the velocity is given everywhere, and the best average match to pressure equilibrium is found for the outer region. In the present model, velocities are specified only in the flaring region, but pressure equilibrium is enforced along the entire length of the jet.

4. In the solutions preferred by LB02b, momentum flux $= \Phi/c$ initially. This is required for the jets to decelerate from highly-relativistic velocities on parsec scales, as in unified models of BL Lac objects and FR I radio galaxies. It is not an explicit constraint in the present models, where the momentum flux is relatively higher (corresponding to the solutions in section 3.3.6 of LB02b).

5. I use power-law, isothermal approximations for the external density and pressure distributions, whereas LB02b use a double-beta-model with varying temperature. The resulting differences are minor (Fig. 4.2).

LB02b discussed the effects of varying the assumptions of their analysis. This led to a spread of values around those for their *reference model* which I quote here. Table 4.2 compares values of key parameters for my model jet and that from LB02b's reference model at the brightening point and at 12 kpc from the nucleus.

The energy fluxes of the two model jets are quite similar, despite the differences in starting assumptions. In terms of the available energy flux Φ (with the rest-mass component subtracted, as in Section 4.5.2.3 and LB02b), I find $\Phi = 1.6 \times 10^{37}$ W, compared with $\Phi = 1.1 \times 10^{37}$ W for LB02b. This is because the geometries of the two jets are identical; in the outer region their velocities are very similar, and they are both close to pressure equilibrium with the surroundings. The main difference is in the mass flux, which is a factor of 1.5 times larger at 12 kpc from the nucleus in the present model.

There is a larger difference between the initial conditions for the two models at the brightening point. The model jet of LB02b has an initial density roughly 5 times lower than that described here, but is also overpressured: its energy density is dominated by the internal energy of relativistic particle rather than by bulk kinetic energy, as can be seen from the differences in the value of $\mathscr{R}$ at the brightening point (Table 4.2). The

Table 4.2: Comparison between derived parameters for 3C 31 derived in this chapter and in LB02b. Following B94 and LB02b, I quote the relativistic Mach number, $\mathscr{M} = \gamma_v v/\gamma_{c_s} c_s$, where c_s is the sound speed and $\gamma_{c_s} = [1 - (c_s/c)^2]^{-1/2}$.

Quantity	This paper	LB02b
Energy flux (10^{37} W) (excluding rest mass)	1.6	1.1
Initial momentum flux (10^{28} kg m s^{-2})	7.7	3.7
Density at brightening point (10^{-27} kg m^{-3})	12	2.5
Mass flux at brightening point (10^{27}kg yr^{-1})	6.2	1.0
Mass flux at 12 kpc (10^{27} kg yr^{-1})	47	32
Pressure at brightening point (10^{-11} Pa)	1.9	15
$\mathscr{R}$ at brightening point	13.4 (jet)	0.4
	7.7 (layer)	0.4
Mach number at brightening point	7.7 (jet)	1.5
	2.5 (layer)	1.5

very low initial density in LB02b's reference model is derived from the requirement for FR I jets to be able to decelerate from bulk Lorentz factors ∼5 on parsec scales. If this requirement is relaxed, as in the high-momentum solutions described in section 3.2.6 of that paper, results closer to those in presented here are obtained. The entrainment rate at the beginning of the flaring region in both models is very low and could be provided by mass input from stars (Section 4.5.2.4). Both models require an additional source of mass at larger distances from the nucleus, however.

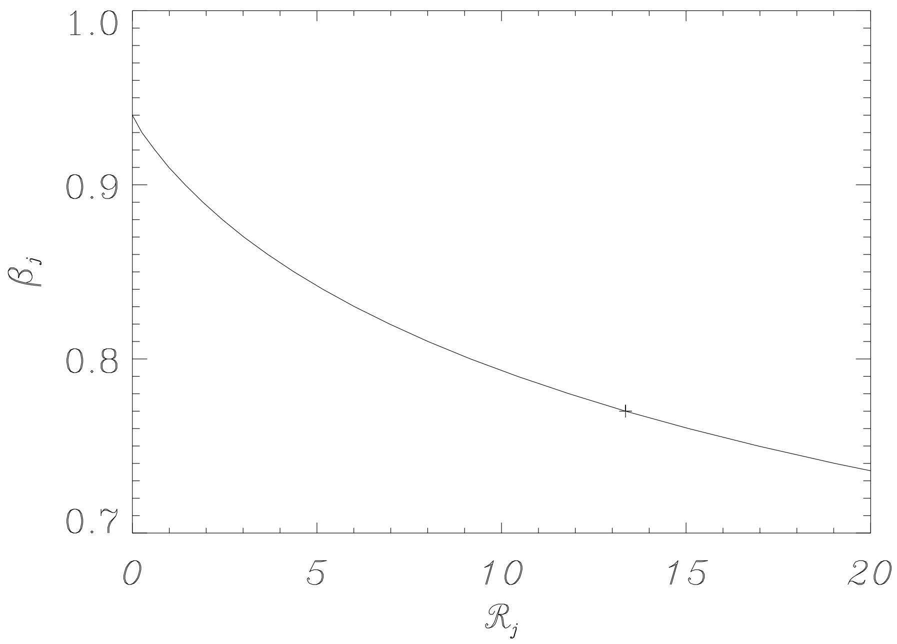

Figure 4.6: The relation between $\mathscr{R}_j$ and β_j for the flaring region. The values of r_0, r_1, $p(x)$ and β_l are fixed at the values determined for 3C 31. The plus sign indicates the value of $\mathscr{R}_j$ for 3C 31.

4.6 Exploring the parameter space of the model

My model uses several parameters derived from observations of 3C 31 to calculate the key physical properties of this object. For other FR I sources, these parameters may be inappropriate, and in this section, I discuss the effects of altering them.

4.6.1 Flaring region

The parameters affecting the solution in the flaring region are the value of $\mathscr{R}_e$, the polynomial coefficients for the outer boundary, the jet and layer velocities and the gradient of the external pressure. I have argued that $\mathscr{R}_e$, which is always very large, cannot affect my solutions significantly. The shape of the outer boundary plays an important role in

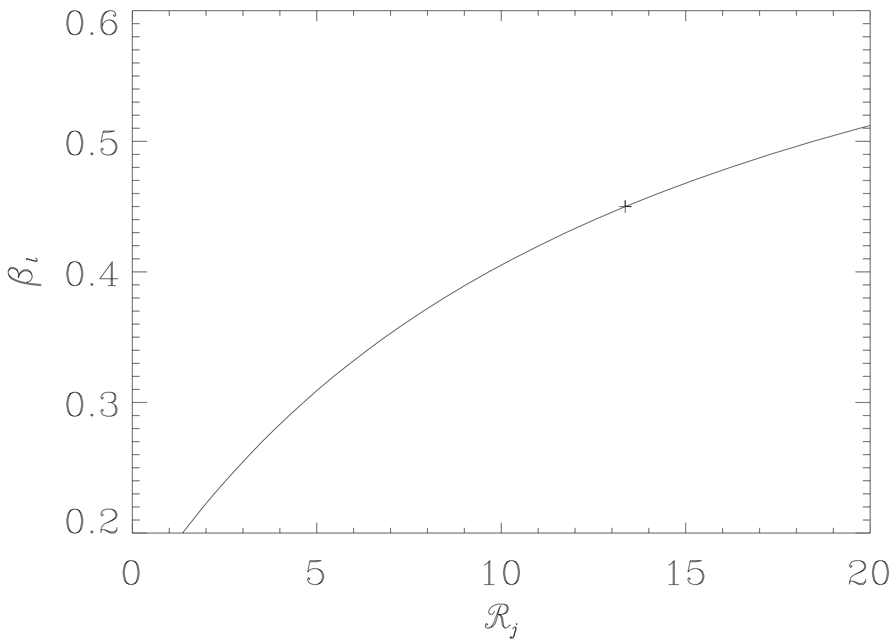

Figure 4.7: The relation between $\mathscr{R}_j$ and β_l for the flaring region. The values of r_0, r_1, $p(x)$ and β_j are set to the values determined for 3C 31. The plus sign indicates the value of $\mathscr{R}_j$ for 3C 31

determining the buoyancy term and varies from source to source. As the shape function has four free parameters, I will not discuss this point in detail here[3], but I note that faster expansion of the shear layer will lead to larger values of $\mathscr{R}_l(x)$ and smaller entrainment velocities. I can vary the remaining three parameters, β_j, β_l and α_2, individually to determine their effect on my solutions and I plot them against $\mathscr{R}_j$ above. The distributions of $\mathscr{R}_l$, mass flux and v_{ent} are closely related to that of $\mathscr{R}_j$.

Given that the laminar jet is assumed to be in pressure equilibrium with its surroundings at the brightening point, its internal energy is determined. If β_l and the form of the pressure profile are also fixed, then the energy flux minus the rest mass term, Φ (defined by its value at x_1) is also unchanged. Since Φ is a conserved quantity, this is also true for the laminar jet at x_0. A faster jet with the same internal energy must therefore have

[3]More recent models use a two-parameter form for the shape of the flaring region (Canvin & Laing, 2004; Canvin et al., 2005; Laing et al., 2006).

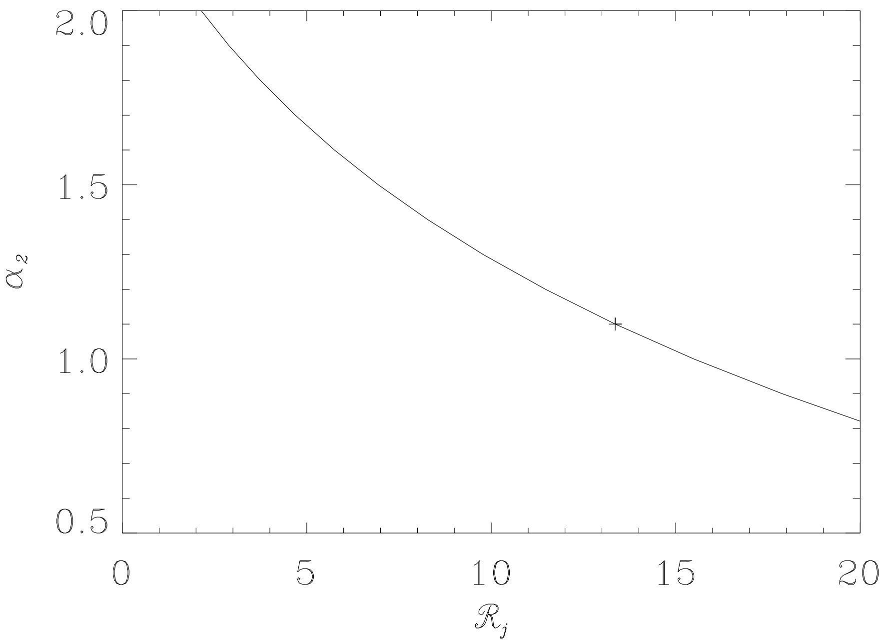

Figure 4.8: The relation between $\mathscr{R}_j$ and α_2 for the flaring region. The values of r_0, r_1, β_j and β_l are fixed at the values determined for 3C 31. The plus sign indicates the value of $\mathscr{R}_j$ for 3C 31.

smaller density and R_j (Fig. 4.6).

Moreover, if one assumes a faster shear layer at x_1, which means that Φ is higher, but β_j remains constant, then the density of the laminar core at x_0 must increase, since the internal energy is fixed there by the pressure balance condition. R_j therefore increases with β_l (Fig. 4.7). The shapes of the distributions of $g_{\rm f}(x)$, $\mathscr{R}_l(x)$ and $v_{ent}(x)$ remain the same, but their normalizations change if the jet or layer velocities are varied. For a faster laminar jet or a slower shear layer, $\mathscr{R}_l$ and $v_{ent}(x)$ both become smaller, indicating that the shear layer is less dense.

The value of $\mathscr{R}_j$ also depends on the pressure profile, quantified here by the exponent α_2 of a power-law distribution. If the pressure decreases more slowly with distance, then the assumption of pressure equilibrium requires the internal energy of the layer to be higher at the end of the flaring region, increasing the energy flux. If the velocity of the laminar core is fixed at the brightening point, as is its internal energy, then a denser laminar jet, and therefore a higher value of $\mathscr{R}_j$ is needed (Fig. 4.8).

4.6.2 Outer region

For the outer region, the situation is much simpler. As $\mathscr{R}_1$, β_1 and r_1 are determined by continuity at the boundary with the flaring region, the only additional parameters inferred from the observations are the half opening angle θ and the power-law exponent of the external pressure profile, α_2. Two factors influence the opening angle: the decrease of external pressure and the expansion associated with entrainment. Of the two, the latter is more important for 3C 31: if I set $v_{ent} = 0$ to remove the entrainment terms, the predicted jet opening angle is around 3° (compared with the observed value of 13°), suggesting that entrainment dominates the expansion.

Figure 4.9 shows how the jet properties change as functions of the exponent of the external density and pressure distributions, α_2. For a jet with a fixed opening angle, a larger value of α_2 (a faster decrease of pressure) reduces the amount of material entrained from the environment into the jet and leads to a slower entrainment velocity. As the buoyancy force can accelerate the material in the jet, a larger value of α_2 can also lead to a slower deceleration in the outer region. The outer region cools due to continuous entrainment of thermal matter from the environment into the shear layer, so $\mathscr{R}_l$ increases with distance at a rate dependent on the entrainment velocity.

If I keep $\alpha_2 = 1.1$ and alter the opening angle, θ, the jet properties vary as shown in Figure 4.10. I find that when the opening angle is small, the jet hardly entrains any material from the environment, and so decelerates more slowly. In extreme cases, the jet could even be accelerated slightly by the pressure gradient. It is interesting to note that the other four sources which have been modelled in detail all have outer region opening angles $< 5°$ (Canvin & Laing, 2004; Canvin et al., 2005; Laing et al., 2006) and show little evidence for deceleration on these scales. Compared with 3C 31, their external environments are significantly less dense and it may be that entrainment is relatively less important at large distances from the nucleus.

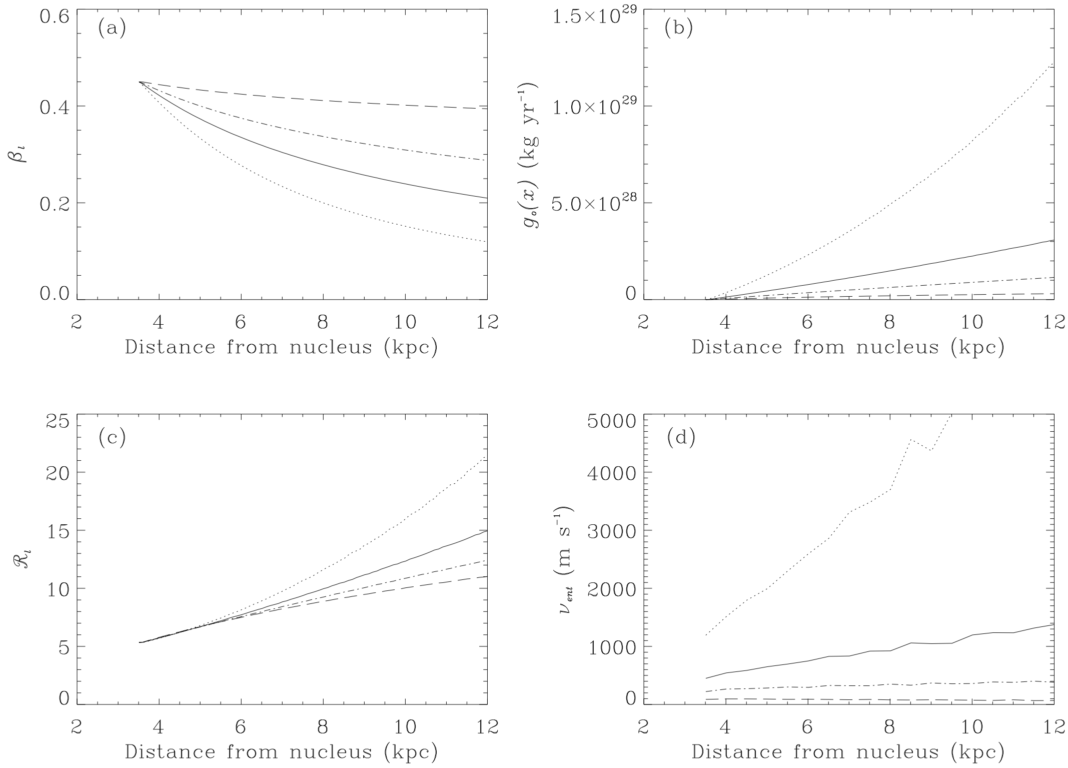

Figure 4.9: The jet properties in the outer region for different values of α_2, the exponent in the external pressure distribution. The solid line is the value estimated for 3C 31, $\alpha_2 = 1.1$. The dotted line, dash dot line and dashed line are for $\alpha_2 = 0.5$, $\alpha_2 = 1.5$ and $\alpha_2 = 2$, respectively. (a) Velocity profile, $\beta_l(x)$. (b) The entrainment function $g_o(x)$. This is the entrained mass flux between the start of the outer region ($x = x_1$) and distance x. (c) Profile of $\mathscr{R}_l(x)$. (d) The entrainment velocity perpendicular to the shear layer surface. Irregularities in the profile are numerical artefacts.

4.7 Conclusions and Further Work

I have constructed an analytical mixing-layer model for jets in FR I radio sources that satisfies the relativistic mass, momentum and energy conservation laws. FR I jets are observed to expand rapidly and then recollimate into conical outflows, and I divide them into flaring and outer regions based on this morphological distinction. I assume that the jet is in pressure equilibrium with its surroundings throughout both regions and divide the flaring region into two parts: a laminar jet with very high bulk velocity, and a slower

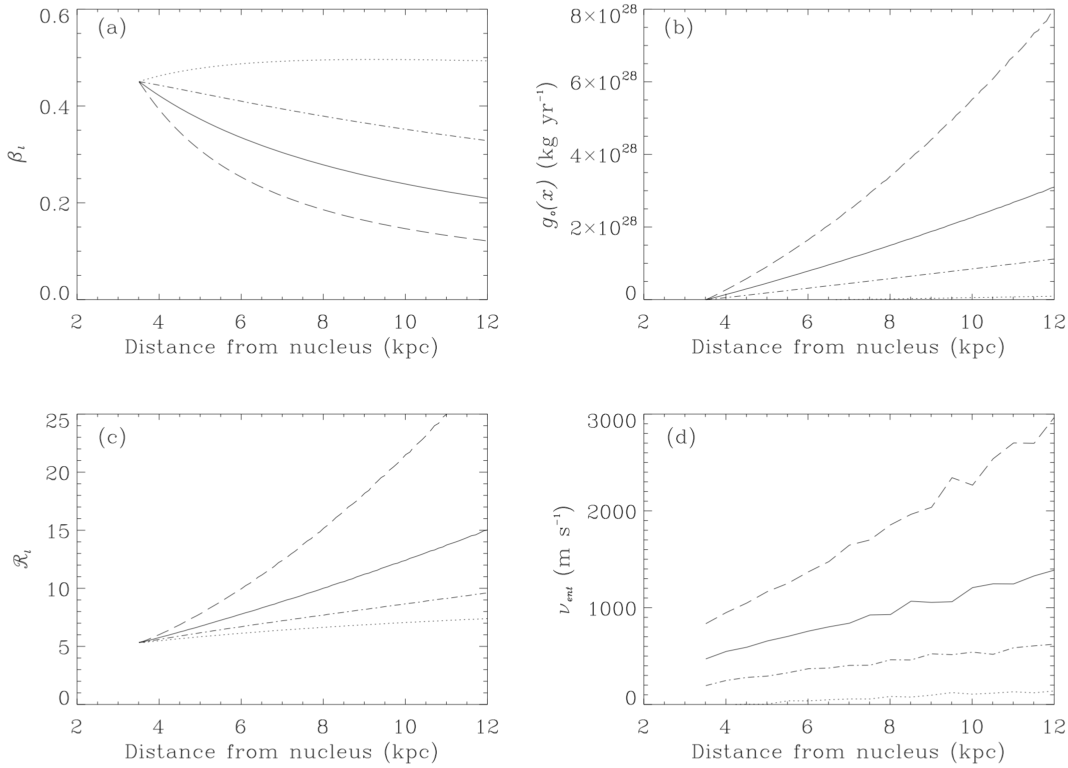

Figure 4.10: The jet properties in the outer region for different values of the opening angle, θ. The solid line is the default value for 3C 31 with $\theta = 13.1°$. The dotted line, dash dot line and dashed line are for $\theta = 3.5°, \theta = 8°$ and $\theta = 20°$ respectively.

shear layer. I prescribe the shape of the shear layer and the (constant) velocities of the laminar jet v_j and shear layer v_l in the flaring region. I can then derive the jet power Q and the ratio of rest mass energy to non-relativistic enthalpy for the laminar jet, R_l. I calculate profiles along the jet of the mass flux $\dot{M}(x)$, the entrainment velocity $v_{ent}(x)$ and the ratio of rest mass energy to non-relativistic enthalpy for the shear layer, $R_l(x)$. Finally, I predict the variation of the bulk velocity of the shear layer, $v_l(x)$, with distance from the nucleus in the outer region and the radius of the laminar core $r_l(x)$ in the flaring region.

I have applied this model to the well-observed FR I radio source 3C 31, and find self-consistent solutions for the jet properties. In the flaring region, I take the shape of the shear layer $r_l(x)$ and the bulk velocities of $v_j = 0.77c$ and $v_l = 0.45c$ from fits to VLA observations (LB02a). In the outer region, the model predicts that the bulk velocity should decrease smoothly to $0.22c$ at 12 kpc, which is consistent with the values derived by LB02a. The corresponding energy flux is $Q = 3.4 \times 10^{37}$ W, equivalent to $\Phi = 1.6 \times 10^{37}$ W if the rest-mass contribution is subtracted.

I find that $\mathscr{R}_j = 13.4$, and that $\mathscr{R}_l(x)$ in the shear layer decreases from $\approx$7.5 at the beginning of the flaring region to 6.7 and then stays almost constant until the jet recollimates. In the outer region, $\mathscr{R}_l(x)$ increases from 6.7 to 15.7 at 12 kpc, indicating that the temperature of the material in the outer region is decreasing with distance. The velocity of entrainment into the jet varies with distance, but has a characteristic value of a few hundred ms^{-1}.

My model gives a somewhat larger energy flux for 3C 31 than that of LB02b, who find $\Phi = 1.1 \times 10^{37}$ W by assuming that there are no transverse velocity variations in the jets. The two models are quite similar in in the outer region, but differ more significantly at the start of the flaring region: my analysis here assumes pressure equilibrium, whereas LB02b require a significant over-pressure and consequently find a lower initial density. Both models require entrainment rates which are consistent with estimates of mass input from stars at the base of the flaring region, but not at larger distances.

I plan to apply a slightly generalized version of my analysis to the other FR I jets for which velocity models and adequate X-ray data are available (Canvin & Laing, 2004; Canvin et al., 2005; Laing et al., 2006). Complex, non-axisymmetric structures are observed at the start of the flaring regions of these jets, as they are in 3C 31 (LB02a). It is plausible that these are shocks in the supersonic flow required in the core, although the detailed morphology of the best-resolved example, NGC 315, suggests otherwise (Laing et al., 2006). The model requires that there should be a clear demarcation in velocity between the core and the shear layer in FR I jets and predicts the shape of the former. This can in principle be tested using the techniques developed by LB02a, but existing observations are limited by insufficient resolution or sensitivity in regions of rapid deceleration close to the nucleus.[4] EVLA and e-MERLIN should be able to image the flaring regions in detail and to resolve a core/shear-layer structure if one is present.

[4]Transverse velocity gradients are clearly detected, but they are well characterized only at larger distances from the nucleus, where the shear layer makes up much or all of the flow in my picture.

Chapter 5

The maximum sizes and ages of FR II sources

In the last chapter, I developed an analytical mixing-layered model describing the steady state of FR I type radio galaxies. Could the entrainment process be important for FR II sources as well? In this chapter, I will investigate how entrainment could affect the evolution of FR II sources and discuss the resulting constraints on their maximum sizes and ages.

The main idea is to consider how the laminar parts of FR II sources are eroded by entrainment due to interaction with their surrounding lobes. I describe the entrainment process by embedding the W09 mixing-layer model for FR I jets in a simple, self-similar model of an FR II radio lobe. I then track the evolution of the resulting FR II source through the P-D diagram, while monitoring how its laminar jet is gradually eroded by the growing turbulent shear layer at the interface between the jet and the lobe. I find that the laminar jet can ultimately be destroyed and that this places interesting limits on the sizes and ages of FR IIs. This leads to the idea that FR IIs may evolve into FR Is, which I briefly explore.

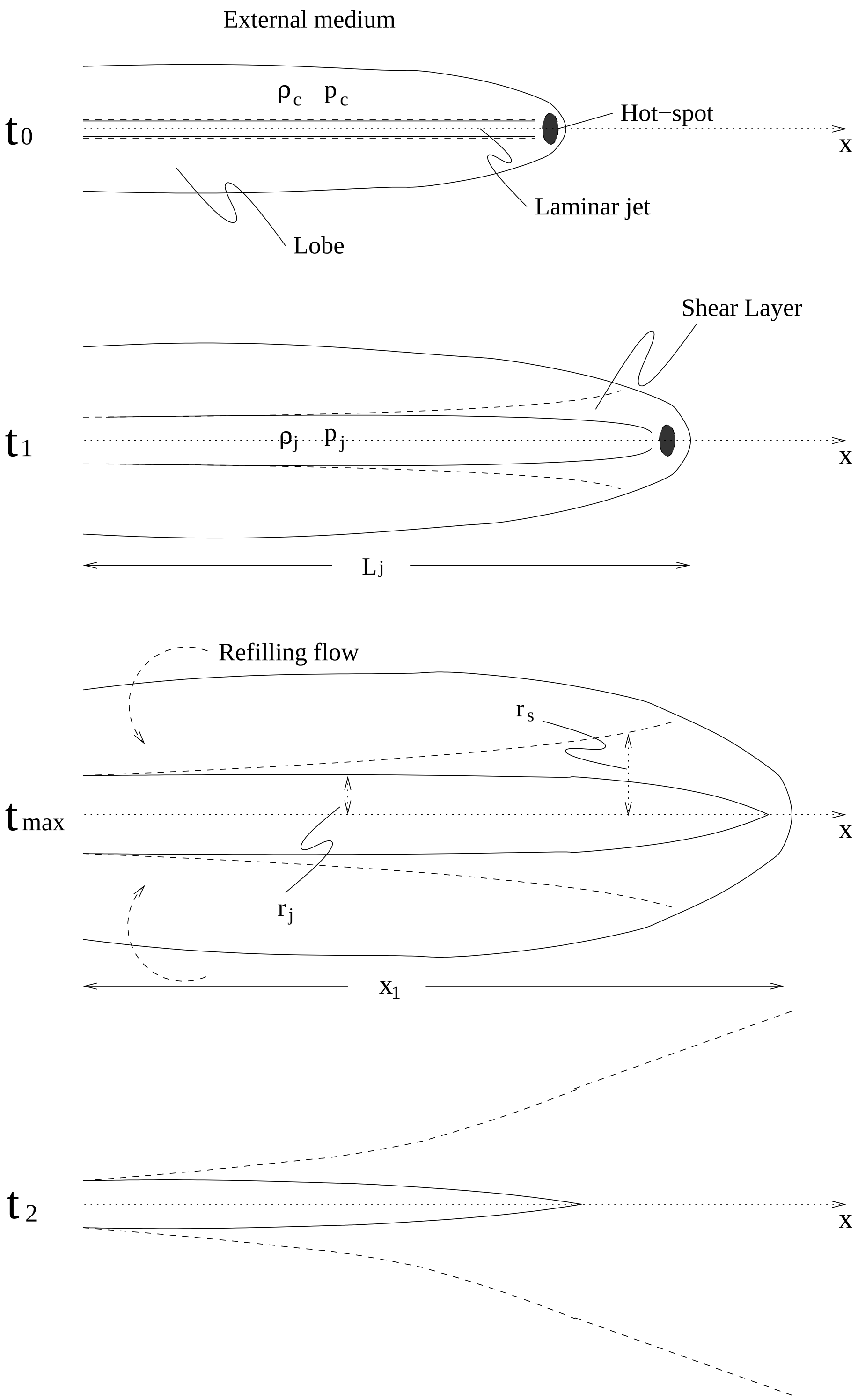

Figure 5.1: Sketch of the evolution of a radio outflow. At t_0, the young outflow is showing a FR II morphology. At t_1, the outflow is still in FR II phase while the shear layer has already grown. At t_2, the hotspot vanish and the outflow will transfer into FR I stage after this age.

5.1 Development of the model

I describe FR II objects by embedding a laminar jet inside a surrounding radio-emitting lobe. A number of simulation work indicate that the density in the lobe is much lower than its environment (Lind et al., 1989; Clarke et al., 1989). However, I assume that a turbulent shear layer may nevertheless form at the jet-lobe interface. This shear layer will entrain and mix material from both regions, and this entrainment will gradually erode the laminar jet. More specifically, once all of the highly relativistic material in the laminar jet has been mixed up with lobe material in the shear layer, the laminar jet is completely destroyed. I further assume that the hotspots seen in FR II objects *require* (i.e. are powered by) the compact laminar jet. Once the laminar jet is destroyed, the shear layer takes over completely, and the jet turns into an expanding turbulent flow. This flow is still supersonic (and thus capable of forming weak shocks and working surfaces), but probably not fast and concentrated enough to support a hotspot. Thus I assume that, once the laminar jet is destroyed, the hotspots will also vanish. At this point, the object will cease to be a "proper" FR II and will most likely resemble a lobed FR I. A sketch of this process is shown in Figure 5.1.

I acknowledge from the outset that the scenario suggested here is necessarily speculative. This is because some key physics (such as the process by which hotspots are powered) remain poorly understood at present and some key parameters (such as the density inside FR II radio lobes and the associated entrainment rates) are not sufficiently constrained by observations. I have therefore tried to be very clear about any key assumptions I make and the reasoning behind them.

In the following sections, I will first outline the analytical FR II lobe model I use and then describe the mixing-layer model introduced in Chapter 4 for the interaction of a laminar jet with its environment. Finally, I will present the results of the combined model for some typical parameter choices.

5.1.1 The self-similar model for FR II lobes

The analytical models for FR II sources have been discussed in detail in Chapter 3. In this section, I summarize only the key features of the KA97 and KDA model that are relevant to the present investigation.

Following KA97's suggestion, the evolution of the size of the jet is determined by a balance of the ram pressure of the jet material and that of the medium surrounding the host galaxy, which is pushed aside by the jet. The density distribution outside the core radius, a_0, is approximated by a power-law, $\rho(x) = \rho_0(a_0/x)^{\alpha}$, where x is the radial distance from the central AGN and ρ_0 is the density at the core radius, a_0. The exponent α is constrained by observations and is typically around 1.5. KA97 suggested that, for typical radio galaxies, $\rho_0 = 7.2 \times 10^{-22}\,\mathrm{kg\,m^{-3}}$ at $a_0 = 2\,\mathrm{kpc}$.

Having set the density profile above, I can express the length of the lobe by $L_j = L_j(Q_0, t)$, where Q_0 is the jet power and t is the jet age. The pressure of the lobe also evolves with jet age and can be written as $p_c = p_c(R_T, Q_0, t)$. R_T is the axial ratio, which is defined as the ratio between the length of the jet (from core to hotspot)and the jet radius and it is normally distributed between 1.3 and 6. In this chapter, I adopt an average value of $R_T = 2.0$ for simplicity (Leahy & Williams, 1984).

For calculating the luminosity evolution of the radio galaxies, I use the original KDA model which express the luminosity of a radio galaxy is a function of Q_0, z and t. Here, for simplicity, I also fix α, ρ_0, a_0 and R_T with the values discussed in last two paragraphs.

5.1.2 Entrainment and the mixing-layer model

In Chapter 4 (also see W09), I constructed a mixing-layer model for FR I sources, in which a laminar jet interacts with its environment by forming a turbulent shear layer at the interface between the two regions. This growing shear layer continuously entrains and mixes material from the jet and its environment, until finally the laminar core has been completely eroded and disappears. The structure of the different layers is determined by using relativistic fluid mechanics and applying the relativistic conservation laws of mass, momentum and energy.

In this chapter, I borrow this basic picture to estimate under what conditions the jet region of an FR II object may disappear. I assume that an FR II lobe evolves as described by the KA97 model, while the jet embedded inside the lobe is presumably subject to entrainment from the lobe and thus evolves following the mixing-layer model described in W09. Although in some FR IIs, the lobe does not appear to extend all the way back from the hotspot to the core, I assume that for the model discussed in this chapter, the jet regions of the FR IIs are not in direct contact with the external environment, but only with the material in the radio lobes. This is the main difference between the application of the mixing layer model to FR I jets (as presented in Chapter 4 & W09) and its application here to FR II jets. In the present case, I assume that the properties of the material in the lobe have uniform distributions and are given by the KA97/KDA model. With this assumption, the mixing layer model for FR II jets is just a simplified, "constant environment" version of the FR I model described in Chapter 4 (W09). In particular, the external pressure, p_e, takes on a constant value p_c, which can be calculated from the KA97 model as $p_c = p_c(Q_0, t)$.

For this simplified case, once the power, Q_0, is fixed for a certain jet, I can express the radii of its laminar jet, r_j and shear layer, r_s as a function of the distance away form the central AGN, x and the jet age, t:

$$r_j^2(x,t) = r_0^2 - \frac{c g_{\mathrm{f}}(x)}{\pi p_c(t) \frac{\Gamma_j}{\Gamma_j - 1} \gamma_j \beta_j \left(\mathscr{R}_s \frac{\mathscr{R}_j + 1}{\mathscr{R}_s + 1} \frac{\gamma_j \beta_j}{\gamma_s \beta_s} - \mathscr{R}_j \right)}, \tag{5.1}$$

$$r_s^2(x,t) = r_j^2(x) + \frac{c g_{\mathrm{f}}(x)}{\pi p_c(t) \frac{\Gamma_s}{\Gamma_s - 1} \gamma_s \beta_s \left(\mathscr{R}_s - \mathscr{R}_j \frac{\mathscr{R}_s + 1}{\mathscr{R}_j + 1} \frac{\gamma_s \beta_s}{\gamma_j \beta_j} \right)}, \tag{5.2}$$

where c is the speed of light, $\Gamma_j = \Gamma_s = 4/3$ are the adiabatic indices of the material inside the laminar part and the shear layer. The other parameters, together with their values on the right hand side of the equations, are discussed in the following paragraphs.

The values $\beta = v/c$ and $\gamma = (1 - \beta^2)^{-0.5}$ are measures of the bulk velocity. The analysis of some typical FR I sources indicate that bulk velocities are $\beta \approx 0.8 - 0.9$ where the jets first brighten abruptly and decelerate rapidly to speeds of $\beta \approx 0.1 - 0.4$ where recollimation takes place. For powerful FR II sources, the bulk velocity can be much higher. Since I am only interested in a qualitative evaluation of the basic entrainment scenario at the moment, I simply adopt $\beta_j = 0.99$ and $\beta_s = 0.4$ as typical values in the following calculations.

$\mathscr{R}_j$ is defined as the ratio between the rest mass energy and non-relativistic enthalpy. It is hard to estimate the value of $\mathscr{R}_j$ from observations, but the result of Chapter 4 (W09) finds $\mathscr{R}_j = 13.4$ from the application of the mixing-layer model to the proto-typical FR I source 3C 31. I assume that the value of $\mathscr{R}_j$ remains the same throughout the jet life and fix the value at 10 for the calculations in this chapter. For uniformly distributed pressure, $\mathscr{R}_s$ is not a function of x any more and is given by:

$$\mathscr{R}_s = \frac{\frac{\mathscr{R}_j\gamma_s\beta_s}{\beta_j-\beta_s} + \mathscr{R}_j\gamma_s\gamma_j + \gamma_j\gamma_s}{\frac{(\mathscr{R}_j+1)\gamma_j\beta_j-\mathscr{R}_j\gamma_s\beta_s}{\beta_j-\beta_s} - (\mathscr{R}_j+1)\gamma_s\gamma_j}. \tag{5.3}$$

The parameter r_0 is the initial radius of the jet at the brightening point. With the parameters defined above, I find:

$$r_0^2(t) = \left(1 - \frac{1}{\Gamma_j}\right) Q_0/[\gamma_j^2(\mathscr{R}_j + 1)p_c(t)\beta_j c\pi]. \tag{5.4}$$

The function $g_{\rm f}(x) = \int \rho_c v_{ent} dS$ is the entrainment rate, which depends on the lobe density, ρ_c and the entrainment velocity, v_{ent}. It also depends on the area of the entrainment surface, which is a function of $r_s(x,t)$. Equation (5.1), (5.2) together with $g_{\rm f}(x)$ form a closed system. I solve them numerically to obtain the shape of the shear layer and of the laminar part using the values of the parameters discussed above.

I assume the density of the material and the entrainment velocity have a uniform distribution inside the lobe, so I can take $\eta = \rho_c v_{ent}$ out of the integration and make it a tuneable parameter representing the efficiency of entrainment. It is hard to obtain the density in the lobe or the entrainment velocity directly from the observation, so I do not consider ρ_c and v_{ent} separately at the moment. Instead, I ask what values of η are indicated by the observed maximum sizes and ages of FR II objects. I then consider whether the entrainment rates implied by these values of $\eta$are plausible.

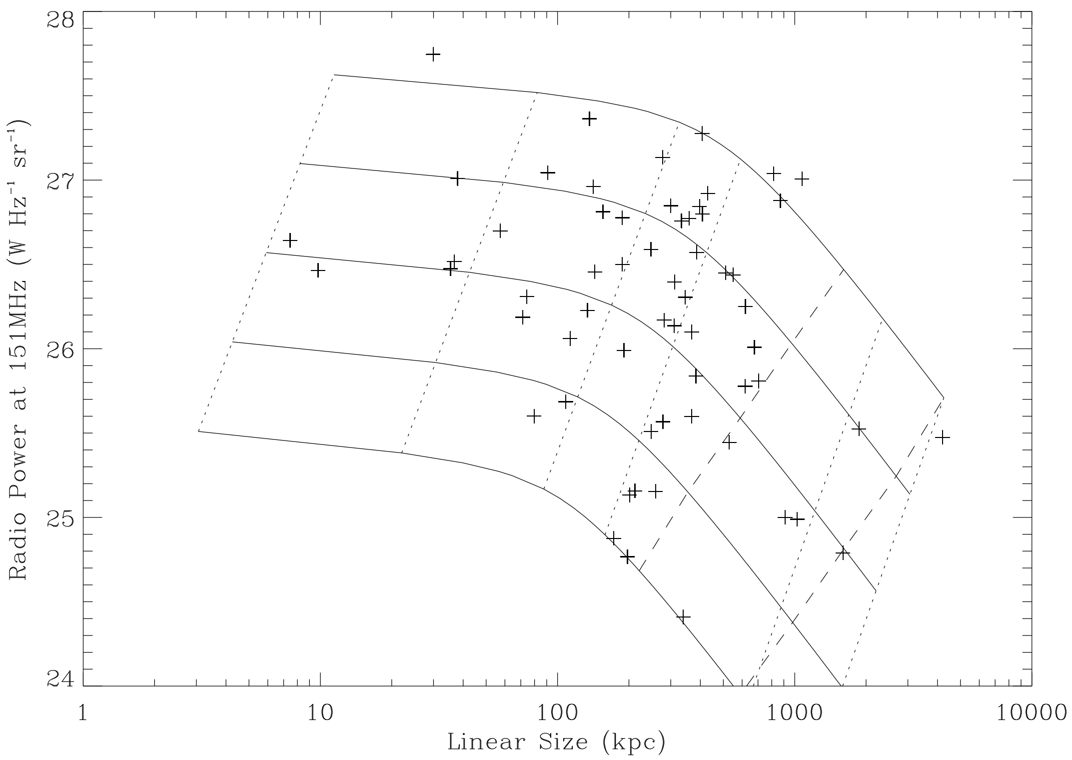

Figure 5.2: The evolution tracks of low-redshift radio outflows on P-D diagram. The solid lines refer to galaxies with different powers, Q_0, range from $\log(Q_0) = 37$ to $\log(Q_0) = 39$, with a step of 0.5. Dotted lines are time markers, which refer to 1 Myr, 10 Myr, 50 Myr, 100 Myr,500 Myr and 1000 Myr respectively. Dashed lines are plausible transition age for jets with different powers. The left line refers to $\eta = 2.5 \times 10^{-23}\,\mathrm{kgm^{-2}s^{-1}}$ while the right line refers to $\eta = 3.8 \times 10^{-24}\,\mathrm{kgm^{-2}s^{-1}}$.

5.1.3 The maximum age of the FR II sources

For a jet with any age t, one can always find a distance, x_1, where $r_j(x_1, t) = 0$. Due to the low density of the lobe and small entrainment rate, x_1 is much larger than $L_j(t)$ initially. As the jet ages, the lobe pressure decreases, which allows the shear layer to expand faster and causes x_1 to decrease. Meanwhile, L_j increases with t. Thus, there should be a certain age, $t_{\max}$, when $x_1(t_{\max}) = L_j(t_{\max})$. At this time, the laminar jet disappears, and the hotspot may vanish, as discussed at the beginning of Section 5.1. I therefore argue that this point marks the maximum age and size of the radio object as an FR II source.

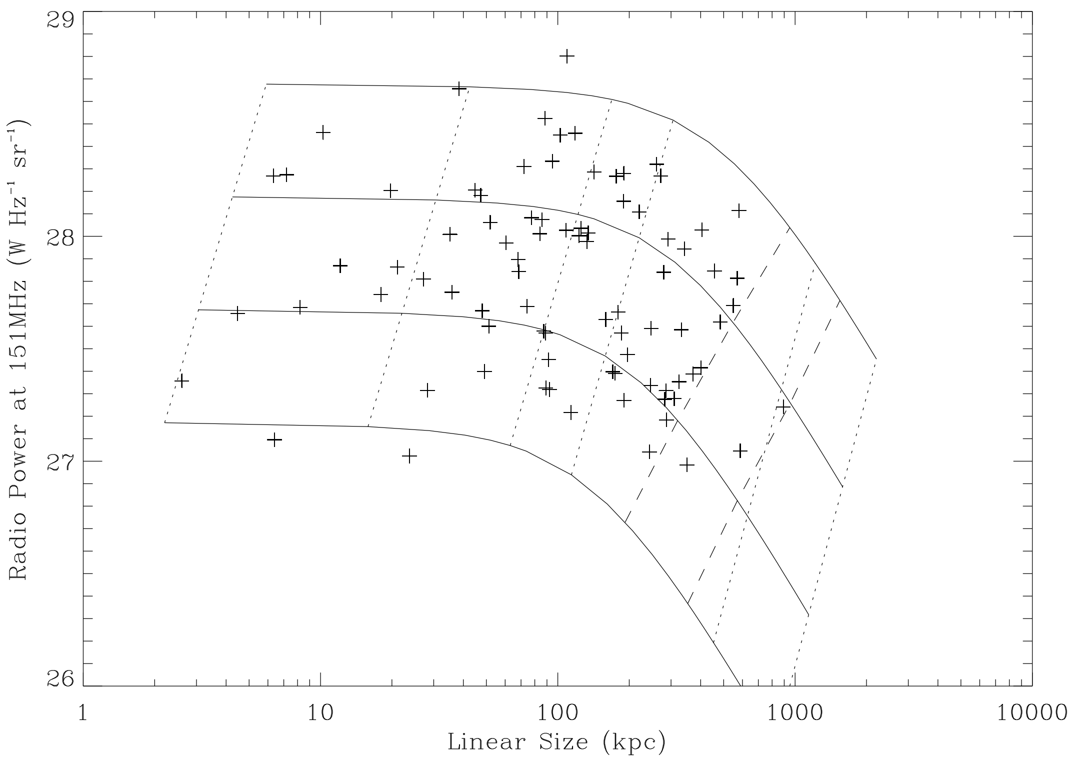

Figure 5.3: Same diagram like Figure 5.2, but for high-redshift sources. The solid lines refer to the jet power from $\log(Q_0) = 38.5$ to $\log(Q_0) = 40$ with a step of 0.5. The left dashed line refers to $\eta = 1.0 \times 10^{-21}\,\mathrm{kgm^{-2}s^{-1}}$ while the right dashed line refers to $\eta = 4.0 \times 10^{-22}\,\mathrm{kgm^{-2}s^{-1}}$.

In order to test if these limiting sizes and ages are of practical interest, I consider FR II objects with different powers located in typical environments and track their evolution (solid lines) on the P-D diagrams shown in Figure 5.2 and Figure 5.3. At the same time, I also plot FR II sources from a complete sample (3CRR) on the same diagrams for comparison. Since the overall jet environments and emission evolution may be different for sources at different redshifts, I split the total sample into a low-redshift sample ($0 < z < 0.5$) and a high-redshift sample ($z > 0.5$). For the low-redshift sample, I consider jets located at $z = 0.2$ with powers ranging from 10^{37} W to 10^{39} W, while for the high-redshift sample, I track jets located at $z = 1.0$ with powers ranging from $10^{38.5}$ W to 10^{40} W. For comparison, the luminosities of the observed sources in each sample are converted to the luminosity that they would have at distances corresponding to $z = 0.2$ and $z = 1.0$, respectively. I adopt KDA's value of ρ_0 and a_0 for the $z = 0.2$ case. However, in Chapter 3 (WK08), I have investigated the cosmological evolution of the environments around radio galaxies and suggested that the density of the external medium might be higher in the earlier universe. Based on WK08 model, I assume that for the $z = 1.0$ case, an environment with 2 orders of magnitude higher density is adopted.

AGN are thought to be active for around 10^9 yr, so I track the evolution of radio galaxies up to this age. Plausible maximum ages can be estimated from Figures 5.2 and 5.3 for different jets with different η, and two *limiting* cases are marked with dashed lines in each figure. The left [right] dashed line corresponds to a value of η for which the model is consistent with most [all[1]] of the observed sources surviving as FR IIs at their inferred age. Numerically, these limiting values of η are as follows. In Figure 5.2, the left mark corresponds to $\eta = 2.5 \times 10^{-23}\,\mathrm{kgm^{-2}s^{-1}}$, while the right mark corresponds to $\eta = 3.8 \times 10^{-24}\,\mathrm{kgm^{-2}s^{-1}}$. Meanwhile, in Figure 5.3 the left mark corresponds to $\eta = 1.0 \times 10^{-21}\,\mathrm{kgm^{-2}s^{-1}}$ while the right mark corresponds to $\eta = 4.0 \times 10^{-22}\,\mathrm{kgm^{-2}s^{-1}}$.

Are these values of η reasonable, in the sense that they represent plausible entrainment rates for FR II jets? Currently, we do not have direct observational measurements of either lobe densities or entrainment velocities for FR II sources. However, some simulations (Lind et al., 1989; Clarke et al., 1989) give an idea that the lobe density might be much lower than the external density. I assume that it is 1000 times lower. With this assumption, I could find v_{ent} is equal to a few thousands $\mathrm{ms^{-1}}$ which is consistent with what I get in Chapter 4(W09), and it is quite reasonable.

From Figures 5.2 and Figure 5.3, I find that the maximum FR II age is significantly affected by the jet power and η. If the shear layer can entrain material from the environment more easily, either because the surrounding gas is denser or the entrainment velocity is higher, the laminar part is eroded more quickly, leading to an earlier end of the FR II stage. At the same time, if the jet is more powerful, the laminar part can survive longer and the FR II morphology is sustained to an older age. This gives a plausible explanation for the observational fact that the most powerful jets tend to be FR II objects. In the context of this scenario, this is because powerful jets spend more of their life in the

[1] Actually, all but one source in the low-z sample.

FR II stage. Extremely powerful jets in certain environments may stay in the FR II stage throughout their entire lifetimes.

My model predicts that the maximum age of FR II sources is a few 10^8 yrs, which is in good agreement with observations that show that some FR IIs can reach a few 10^8 yrs as estimated from spectral aging (Alexander & Leahy, 1987). Chapter 3 (WK08) find a smaller maximum age of a few 10^7 yrs. However, they assume $\alpha = 2.0$, while here I am considering $\alpha = 1.5$ here, which gives a denser environment leading to a more slowly growing lobe. Moreover, I have only tracked the jets with fixed environment and redshift, conditions which will vary in reality between different sources. The reasonable agreement between predicted and observed maximum FR II lengths and ages, for plausible parameter choices, suggests that entrainment may indeed be relevant in limiting the sizes and ages FR II jets.

5.2 Evolution from FR IIs into FR Is

The existence of a maximum size and age for an FR II source due to the erosion of its laminar jet raises an obvious question: what happens to an object that reaches this limit? In this section, I will argue that such FR II sources are likely to evolve into FR Is. Thus I will outline a simple, but hopefully plausible, scenario for the transition of a radio galaxy with an FR II morphology to one with an double fat FR I morphology and then 3C 31 morphology. The basic idea is sketched in Figure 5.1.

When a stable radio outflow is born at time t_0, it exhibits an FR II structure with a laminar flow embedded inside a lobe and a hotspot at the end. At stage t_1, where $t_0 < t_1 < t_{max}$, the outflow grows with age, following KA97 model. Meanwhile, however, the laminar part continuously suffers entrainment from the lobe, and the structure of the centre part of the outflow can be described by the W09 model. The outflow evolves with an FR II morphology until it reaches the maximum age, $t_{\rm max}$, when the hotspot vanishes. For the detailed evolution of the radio outflow at this stage, please see Section 5.1.3.

When the outflow evolves to an age of t_2, where $t_2 > t_{\rm max}$, the shear layer dominates the end region of the jet and the hotspot vanishes. A weaker shock and global lobe structure may still exist at this point, with plasma being injected into the lobe after the shock at the end of the jet. The expected structure at this stage is reminscent of a typical lobed FR I source. As the outflow becomes even older, the energy from the shear layer can hardly support the lobe structure or the working surface of the shock at the end of the jet, so the plasma will form a turbulent tail, with the lobe disappearing either because it is refilled from the environment or because it simply runs out of energy. At the end of this evolution stage, we observe a naked tailed jet like 3C 31. The jet is in direct contact with the environment and a mixing shear layer is formed. At the same time, the laminar part may shrink again as the density of the environment is higher than that of the lobe.

From radio observation, the spectral indexes of different radio sources show different distributions. For FR II sources, the spectral index near the hotspot is flatter compared to that near the core, which means the particle population near the hotspot is younger and the particles travel from the hotspot to the core in the lobe. However, for tailed FR Is, the particles travel from the core to the end of the jet as the spectral indexes near the core are flatter. Lobed FR Is are more complex and both kind of distributions could happen. This is consistent with my transition model: initially we have classic FR II model whose particles injected into the lobe travel backwards from hotspot. Then the radio source evolve into lobed FR I stage when particles still travel backwards although the central jet could not supply enough energy to form a hotspot any more. At the end, the lobe formed by backward particles totally fade away and we will have a naked tailed FR I whose particles simply travel outwards.

My model here mainly explain the transition between different structures and morphologies. The luminosity evolution is based on individual FR I or FR II models, which is in radio band. However Ledlow & Owen (1996) find that in optical band there is a clear transition luminosity as well. It could be interesting if more work can build a connection between radio transition and optical transition. I will include this point in the future work, but at the moment I will concentrate on current model which works in radio band at least.

It is interesting to compare this simple picture of the evolution of an FR II into an FR I with that described by Kaiser & Best (2007). In their model also, all radio sources start with an FR II morphology. They find that weak FR IIs quickly reach pressure equilibrium with their environment inside the core region and thus develop into FR Is. However, they also argue that powerful FR IIs can essentially survive forever with an FR II morphology. The transition scenario developed here is complementary to theirs, providing a new way for more powerful FR IIs to develop into FR Is late in their lives. Combining the two transition modes, it appears that FR IIs evolve into FR Is either at a very young age, before they have even left their core environment, or very late in their lives, after the total erosion of their laminar jets due to entrainment.

5.3 Conclusion

I have embedded a mixing-layer model originally developed for modelling FR I jets into a self-similar model for FR II radio lobes to study the effect of entrainment on the laminar jets in FR II objects. I find that, for reasonable parameters, the growing mixing layer between the laminar jet and the radio lobe can entrain significant amounts of material from both regions. The laminar jet can be completely eroded on a time scale of $t_{\rm max} \sim$ a few 10^8 yrs, comparable to the inferred ages of the oldest observed FR IIs. I argue that, with no laminar jet to power the hotspots, a source reaching $t_{\rm max}$ will cease to be an FR II. Thus entrainment can set strong upper limits on the maximum sizes and ages of FR II sources.

I have also sketched the likely evolution of FR II sources beyond $t_{\rm max}$. Once the hotspots are extinguished, such sources will initially look like lobed FR I objects. However, ultimately their lobes must run out of energy and will be refilled by the environment, at which point they will emerge as classic, 3C 31-like FR I sources. This simple scenario suggests a new evolutionary connection between FR I and FR II sources and may help to shed new light on the FR I/II dichotomy.

In closing, I stress that the picture developed here – especially that of the evolution beyond $t_{\rm max}$ – is still basically a toy model. Further work should include Monte-Carlo population synthesis simulations to explore if the observed size, age and power distributions of FR Is and FR IIs can be explained with a single evolutionary paradigm like that sketched above. I am also planning to model the evolution of the jet from FR II to lobed FR I to tailed FR I in more detail. The ultimate goal of this work is to build a unified model for all types of radio galaxies and track how they evolve and morph into each other across the P-D diagram.

Chapter 6

Summary

In this thesis, I have investigated the evolution of the radio galaxies and discussed important underlying physical processes, which drive the evolution. This chapter summarises findings of the thesis and outlines promising directions for future work.

In Chapter 3, the cosmological evolution of the FR II population was studied. Monte-Carlo simulations were carried out to generate artificial samples which were then compared to the observed samples. The simulations were based on the observed RLF together with an evolutionary model for individual FR II sources. The use of the RLF ensured a proper fit to the relative number counts of FR IIs with different luminosities and redshifts in the P-z diagram. Similarly, using certain assumptions for the values of the jet properties, the FR II evolution model provided good predictions of the source distributions in the P-D diagram. Thus, by introducing a three dimensional P-D-z data cube, I was able to find the distribution of jet properties, which best fit the data, and also study how these properties evolve with redshift.

The main result of this statistical analysis is that the properties of the FR II sources must evolve with redshift. It was concluded that in the early universe, either the environment density was higher or the maximum jet age was smaller, or both were true. It must be noted, however, that the intrinsic distributions of jet parameters cannot be constrained using current observations, except for the jet power and lobe pressure (which are not constrained in the simulation). The artificial samples from my simulation show that the jet power is distributed as a power law, with an exponent of -2. The slope does not change significantly with redshift, at least up to $z = 0.6$. Similarly, the overall lobe pressure of the radio jets rise towards the higher redshift, at least up to $z = 1.2$.

The simulation did not find a good fit for the deepest sample (7CRS) either at the low redshift end or at the high redshift end. The poor quality of the fit at high redshift is mainly because current observations do not have enough sources in the sample at high redshift. Therefore the RLF at the high redshift end is not well known. In order to improve this, deep surveys with larger fields of view must be carried out. The most promising project might be the Texas-Oxford One Thousand (TOOT) radio source redshift survey (Hill & Rawlings, 2003). The TOOT survey is aimed at understanding the evolution of the radio source population down to a flux density of $S_{151\mathrm{MHz}}$=100 mJy, which is 100 times fainter than the 3C survey. With this flux limit, TOOT could probe the typical radio-loud active galaxies to higher redshift. For about a half of the sources in the sample of the TOOT survey the redshifts have been measured, and they provide a high enough surface density of sources at $z \sim 1$. Thus, based on this sample, we can obtain a more accurate number count and distribution of the radio galaxies and generate a more accurate RLF at the high redshift end. Preliminary study of the sample found that the redshift distribution has a deficit of objects with $z \sim 2$, compared to the prediction from the RLF based on the current samples. This is consistent with results from my simulation, which find that there is an excess of sources in the artificial samples at high redshift based on the RLF generated from W01.

At the low redshift end, the main problem is the uncertainty of the FR I/II fraction. The evolution of FR I sources and FR I/II dichotomy are not well understood. Best et al. has analysed a large sample from the Sloan Digital Sky Survey (SDSS), containing thousands of radio galaxies in the local universe. The classification of these radio sources could give us a better knowledge of the ratio between FR Is and FR IIs, and provide a possibility to check if the ratio is evolving with the redshift. With accumulation of the observational data, study of the evolution of FR Is and the plausible FR I/II transition processes will be important directions for the project extension.

Following the ideas discussed above, In Chapter 4 I constructed an analytical model for FR I jets with a shear-layer structure, using a set of relativistic conservation laws. In this model, I assumed that FR Is strongly interact with their environments and that the entrainment plays an important role in the evolution of FR I sources. The external medium was assumed to be continuously entrained into the jet region and result in formation of a shear layer. In the shear layer, the material from the environment is mixed up with the material from the laminar part of the jet. I then applied relativistic conservation laws for mass, momentum and energy fluxes to drive equations describing steady-state FR I jet. Solution of these equations was used to explain the behaviour of a typical FR I source, 3C 31, in good agreement with the observations and previous theoretical work.

I have only applied the model to a single source at present, so an obvious direction for future work with this model is to apply it to other well-studied 3C 31-like FR I sources. This would allow me to estimate the ranges of the distributions of the jet parameters, e.g. the jet power, and test if the implied jet parameters (e.g. the entrainment rate/velocity,) vary widely from source to source or are more or less constant for all FR Is. Understanding the entrainment is one of the key points for understanding the evolution processes of FR Is in this model. We still need more detailed observations to study how the entrainment works? What does the entrained material consist of? What is the typical entrainment rate and is it determined by any condition? ALMA is the next generation mm/sub-mm telescope, which could probably help us answer these questions. ALMA can provide detailed features of the CO emission line, which luminosity is closely related with the mass of the molecular gas. The width of the emission line indicates the turbulent velocity of the molecular gas. Thus, with high-resolution of ALMA, we could detect the amount and the movement of the cold molecular gas around radio galaxy. By comparing it with the predictions of the model, I could test if cold molecular gas could supply enough material to sustain the entrainment rate required by the model or other components are needed. A potential candidate for this observational proposal is Centaurus A, which is one of the closest radio galaxies with FR I type morphology and its jet is believed to contact directly with the environment.

Model for evolution of emission of FR Is can also be an interesting extension of this work. Current research shows that for FR I sources, the spectrum is inconsistent with an ageing model. Although it is possible that the ageing model is wrong Blundell & Rawlings (2002), this could also suggest that there might be a re-acceleration process ongoing in the jet region. By splitting the flaring region into two parts with different velocities, my model implies that the re-acceleration might be caused by the turbulent on the boundary between these two regions. If the turbulent acceleration could solve the spectrum-ageing problem, we could track the evolution of FR Is analytically on the *P*-*D* diagram, similarly to the model for FR IIs.

Building individual models for FR Is can be just a first step towards building a unified model, and explaining the transition between FR Is and FR IIs. It is not clear yet if entrainment is important in evolution of FR IIs. However, if entrainment in FR IIs does happen, its effects can be estimated by embedding the mixing-layer model developed in the Chapter 4 for FR Is into a model for FR II radio lobes. This idea is tested out in the Chapter 5. I assume that the laminar part of an FR II is gradually eroded by the entrainment, causing the jet to cease to be a proper FR II after the laminar part is completely destroyed. It turns out that reasonable maximum jet lengths and ages can be obtained for plausible entrainment rates. Thus the entrainment may indeed limit the maximum sizes and ages of FR IIs. This leads to the idea that FR IIs may evolve into FR Is, which I also briefly explored in the Chapter 5.

This is but a sketch of a plausible scenario for FR I/II transition. Additional processes need to be considered, before it can be generalised, e.g. spectrum of jets must be understood and modelled. Generally speaking, the older populations of particles have steeper synchrotron spectra. In FR II sources, relativistic electrons are accelerated in the hot spot and then injected into the lobe. The spectrum thus is steeper close to the core. For 3C 31-type FR I sources, the spectrum steepens all the way out, since no material flows back to form the lobe. However, for other types of FR Is, things are more complex and both distributions are possible. Such FR Is represent a the transitional phase between the two phases. Using approaches developed in the present work, it is possible to construct models describing any radio sources with any properties. To summarise, the aim of the future project is to develop a unified model of FR I and FR II radio galaxies that correctly describes their evolution, including the possible transitions of objects from one class to the other, and study the evolution of all types of radio galaxies throughout the cosmological ages.

Appendix A

3CRR sample

IAU name	Common name	z	S_{178}/Jy	α_{151}	θ/arcsec	Morphology
0017+124	4C12.03	0.156	10.90	0.870	240.00	II
0013+790	3C6.1	0.840	14.93	0.554	26.00	II
0017+154	3C9	2.012	19.40	0.813	14.00	II
0031+391	3C13	1.351	13.08	0.753	28.10	II
0033+183	3C14	1.469	11.33	0.760	24.00	II
0035+130	3C16	0.406	12.20	0.954	78.00	II
0038+328	3C19	0.482	13.18	0.637	6.80	II
0044+517	3C20	0.174	46.76	0.606	53.10	II
0048+509	3C22	0.937	13.18	0.785	24.40	II
0053+261	3C28	0.195	17.76	1.011	43.40	II
0104+321	3C31	0.018	18.31	0.682	2640.00	I
0106+130	3C33	0.059	59.29	0.701	257.00	II
0106+729	3C33.1	0.181	14.17	0.834	238.70	II
0107+315	3C34	0.689	12.97	1.029	46.70	II
0109+492	3C35	0.067	11.44	0.907	730.00	II
0123+329	3C41	0.794	11.55	0.721	25.00	II
0125+287	3C42	0.395	13.08	0.705	31.00	II

IAU name	Common name	z	S_{178}/Jy	α_{151}	θ/arcsec	Morphology
0127+233	3C43	1.47	12.64	0.756	2.50	II
0132+376	3C46	0.437	11.11	0.905	164.00	II
0133+207	3C47	0.425	28.77	0.994	77.70	II
0134+329	3C48	0.367	59.95	0.341	0.92	I
0138+136	3C49	0.621	11.22	0.410	1.01	II
0154+286	3C55	0.735	23.43	0.725	71.00	II
0210+860	3C61.1	0.188	34.00	0.736	186.00	II
0220+397	3C65	1.176	16.56	0.498	17.40	II
0220+427	3C66B	0.022	26.81	0.736	690.00	I
0221+276	3C67	0.3102	10.90	0.809	2.30	II
0229+341	3C68.1	1.238	13.95	0.736	52.00	II
0231+313	3C68.2	1.575	10.90	0.962	22.30	II
0300+162	3C76.1	0.032	13.29	0.588	200.00	I
0307+169	3C79	0.255	33.24	0.794	88.70	II
0314+416	3C83.1B	0.026	28.99	0.649	650.00	I
0316+413	3C84	0.018	66.81	1.141	510.00	I
0356+102	3C98	0.031	51.44	0.732	307.50	II
0410+110	3C109	0.305	23.54	0.806	96.00	II
0411+141	4C14.11	0.207	12.09	0.840	115.00	II
0433+295	3C123	0.218	206.01	0.652	41.10	II
0453+227	3C132	0.214	14.93	0.790	22.30	II
0518+165	3C138	0.759	24.19	0.225	0.65	II
0538+495	3C147	0.545	65.94	0.137	3.00	II
0605+480	3C153	0.277	16.67	0.577	9.26	II
0651+542	3C171	0.238	21.25	0.731	10.00	II
0659+253	3C172	0.519	16.45	0.822	101.00	II
0702+749	3C173.1	0.292	16.78	0.898	61.00	II
0710+118	3C175	0.768	19.18	0.983	48.00	II

IAU name	Common name	z	S_{178}/Jy	α_{151}	θ/arcsec	Morphology
0711+146	3C175.1	0.920	12.42	0.597	7.00	II
0725+147	3C181	1.382	15.80	0.656	5.70	II
0733+705	3C184	0.994	14.38	0.594	4.80	II
0733+805	3C184.1	0.119	14.17	0.686	182.00	II
0840+380	3C186	1.063	15.36	0.667	1.60	II
0745+560	DA240	0.035	23.21	0.770	2164.00	II
0758+143	3C190	1.197	16.35	0.786	6.70	II
0802+103	3C191	1.956	14.17	0.907	4.90	II
0802+243	3C192	0.059	22.99	0.810	196.00	II
0809+483	3C196	0.871	74.33	0.590	10.00	II
0824+294	3C200	0.458	12.31	0.829	26.00	II
0832+143	4C14.27	0.392	11.22	1.150	38.00	II
0833+654	3C204	1.112	11.44	1.118	36.60	II
0835+580	3C205	1.534	13.73	0.736	18.00	II
0838+133	3C207	0.684	14.82	0.803	14.00	II
0850+140	3C208	1.11	18.31	0.766	11.00	II
0855+143	3C212	1.049	16.45	0.785	9.00	II
0903+169	3C215	0.411	12.42	0.928	59.00	II
0905+380	3C217	0.897	12.31	0.769	12.00	II
0906+430	3C216	0.67	22.01	0.630	30.00	II
0917+458	3C219	0.174	44.90	0.798	189.00	II
0926+793	3C220.1	0.62	17.22	0.946	30.00	II
0931+836	3C220.3	0.685	17.11	0.682	7.40	II
0936+361	3C223	0.136	16.02	0.807	306.00	II
0939+139	3C225B	0.582	23.21	1.095	4.60	II
0941+100	3C226	0.817	16.35	0.861	35.00	II
0945+734	4C73.08	0.0581	15.58	0.850	947.00	II
0947+145	3C228	0.552	23.76	0.713	47.20	II

IAU name	Common name	z	S_{178}/Jy	α_{151}	θ/arcsec	Morphology
0958+290	3C234	0.184	34.22	0.885	110.00	II
1003+351	3C236	0.0989	15.69	0.870	2440.00	II
1008+467	3C239	1.781	14.38	0.857	11.20	II
1009+748	4C74.16	0.568	12.75	0.870	40.00	II
1019+222	3C241	1.617	12.64	0.481	0.91	II
1030+585	3C244.1	0.428	22.12	0.802	53.00	II
1040+123	3C245	1.029	15.69	0.670	9.10	II
1056+432	3C247	0.748	11.55	0.565	13.00	II
1100+772	3C249.1	0.311	11.66	0.872	44.10	II
1108+359	3C252	1.103	11.99	1.085	60.00	II
1111+408	3C254	0.734	21.69	0.752	13.10	II
1137+660	3C263	0.646	16.56	0.754	44.20	II
1140+223	3C263.1	0.824	19.83	0.692	6.80	II
1142+198	3C264	0.022	28.34	0.820	590.00	I
1142+318	3C265	0.811	21.25	0.963	78.00	II
1143+500	3C266	1.275	12.09	0.758	4.50	II
1147+430	3C267	1.14	15.91	0.806	38.00	II
1157+732	3C268.1	0.973	23.32	0.702	46.00	II
1203+645	3C268.3	0.371	11.66	0.449	1.56	II
1206+439	3C268.4	1.40	11.22	0.660	10.90	II
1218+339	3C270.1	1.519	14.82	0.866	12.00	II
1222+131	3C272.1	0.004	21.14	0.600	181.00	I
1227+119	A1552	0.084	12.53	0.940	171.00	I
1228+126	3C274	0.005	1144.50	0.792	836.00	I
1232+216	3C274.1	0.422	17.98	0.936	158.00	II
1241+166	3C275.1	0.557	19.94	0.819	18.80	II
1251+159	3C277.2	0.766	13.08	0.814	58.00	II
1254+476	3C280	0.997	25.83	0.724	14.50	II

IAU name	Common name	z	S_{178}/Jy	α_{151}	θ/arcsec	Morphology
1308+277	3C284	0.239	12.31	0.889	175.00	II
1319+428	3C285	0.079	12.31	0.786	183.80	II
1328+254	3C287	1.055	17.76	0.217	0.09	II
1328+307	3C286	0.849	27.25	-0.401	3.80	II
1336+391	3C288	0.246	20.66	0.775	35.30	I
1343+500	3C289	0.967	13.08	0.630	10.00	II
1349+647	3C292	0.713	11.00	0.800	133.00	II
1350+316	3C293	0.045	13.84	0.614	216.00	II
1404+344	3C294	1.786	11.22	1.022	15.00	II
1409+524	3C295	0.461	91.01	0.285	5.49	II
1414+110	3C296	0.024	14.17	0.745	437.00	I
1419+419	3C299	0.367	12.86	0.557	12.00	II
1420+198	3C300	0.27	19.51	0.837	100.00	II
1441+522	3C303	0.141	12.20	0.719	47.00	II
1448+634	3C305	0.041	17.11	0.816	12.00	I
1458+718	3C309.1	0.904	24.74	0.388	2.90	II
1502+262	3C310	0.054	60.05	0.974	305.00	I
1510+709	3C314.1	0.120	11.55	1.023	201.00	I
1511+263	3C315	0.108	19.40	0.885	200.00	I
1517+204	3C318	1.574	13.40	0.518	0.80	II
1522+546	3C319	0.192	16.67	0.852	105.00	II
1529+242	3C321	0.096	14.71	0.825	307.80	II
1533+557	3C322	1.681	11.00	0.800	33.00	II
1547+215	3C324	1.206	17.22	0.680	10.00	II
1549+202	3C326	0.088	22.23	0.880	1190.00	II
1549+628	3C325	1.135	17.00	0.671	16.00	II
1609+660	3C330	0.55	30.30	0.548	62.00	II
1615+351	NGC6109	0.030	11.66	0.760	790.00	I

IAU name	Common name	z	S_{178}/Jy	α_{151}	θ/arcsec	Morphology
1618+177	3C334	0.555	11.88	1.026	58.00	II
1622+238	3C336	0.927	12.53	0.832	21.70	II
1626+278	3C341	0.448	11.77	0.863	80.00	II
1626+396	3C338	0.030	51.12	1.047	140.00	I
1627+444	3C337	0.635	12.86	0.857	44.70	II
1627+234	3C340	0.775	11.00	0.709	46.70	II
1634+628	3C343	0.988	13.51	0.014	1.10	II
1627+626	3C343.1	0.750	12.53	0.265	0.38	II
1637+826	NGC6251	0.024	10.90	0.720	4030.00	I
1641+173	3C346	0.161	11.88	0.807	13.80	I
1658+471	3C349	0.205	14.49	0.739	88.00	II
1704+608	3C351	0.371	14.93	0.631	75.00	II
1709+460	3C352	0.805	12.31	0.845	13.00	II
1723+510	3C356	1.079	12.31	0.870	75.00	II
1732+160	4C16.49	1.296	11.44	1.000	16.00	II
1759+137	4C13.66	1.45	12.31	0.810	6.00	II
1802+110	3C368	1.132	15.04	1.004	7.90	II
1828+487	3C380	0.691	64.74	0.627	20.00	II
1832+474	3C381	0.16	18.09	0.729	74.00	II
1833+326	3C382	0.057	21.69	0.823	186.00	II
1836+171	3C386	0.018	26.05	0.707	292.00	I
1842+455	3C388	0.09	26.81	0.683	50.80	II
1845+797	3C390.3	0.056	51.77	0.755	229.00	II
1939+605	3C401	0.201	22.78	0.635	24.10	II
2104+763	3C427.1	0.572	28.99	0.876	28.00	II
2120+168	3C432	1.805	11.99	0.780	13.00	II
2121+248	3C433	0.101	61.25	0.719	65.60	II
2141+279	3C436	0.214	19.40	0.855	108.00	II

IAU name	Common name	z	S_{178}/Jy	α_{151}	θ/arcsec	Morphology
2145+151	3C437	1.48	15.91	0.499	34.40	II
2153+377	3C438	0.29	48.72	0.822	22.40	II
2203+292	3C441	0.707	13.73	0.637	36.70	II
2212+135	3C442A	0.027	17.54	0.960	605.00	I
2229+390	3C449	0.017	12.53	0.742	1320.00	I
2243+394	3C452	0.081	59.29	0.825	272.00	II
2247+113	NGC7385	0.024	11.66	0.750	900.00	I
2249+185	3C454	1.757	12.64	0.900	1.30	II
2252+129	3C455	0.543	13.95	0.709	4.00	II
2309+184	3C457	0.428	14.27	1.229	205.00	II
2335+267	3C465	0.030	41.20	0.833	650.00	I
2352+796	3C469.1	1.336	12.09	1.102	74.00	II
2355+438	3C470	1.653	11.00	0.710	24.00	II

Table A.1: Parameters of 3CRR sample used in my work. Column 1: IAU names of the sources. Column 2: Common names of the sources. Column 3: Redshifts of the sources. Column 4: Flux density at $178Mhz$. Column 5: Spectral index between $178MHz$ and $151MHz$. Column 6: Angular size in arcseconds. Column 7: Morphology classification. The data is taken from Willot (2003)

Appendix B

6CE sample

Name	z	S_{151}/Jy	θ/arcsec	Morphology
6C0820+3642	1.860	2.39	24	II
6C0822+3417	0.406	3.06	18	FD(I/II)
6C0822+3434	0.768	2.93	21	II
6C0823+3758	0.207	3.35	81	FD(I/II)
6C0824+3535	2.249	2.42	8	CJ(C)
6C0825+3452	1.467	2.10	7	II
6C0847+3758	0.407	3.07	33	II
6C0854+3956	0.528	2.92	164	II
6C0857+3907	0.229	2.71	24	II
6C0901+3551	1.904	2.07	4	II
6C0902+3419	3.395	2.14	5	PD(I/II)
6C0905+3955	1.882	2.82	5	II
6C0908+3736	0.105	2.33	39	I
6C0913+3907	1.250	2.27	9	CDD(II)
6C0919+3806	1.650	2.72	10	II
6C0922+3640	0.112	3.27	17	I
6C0930+3855	2.395	2.21	5	II

Name	z	S_{151}/Jy	θ/arcsec	Morphology
6C0943+3958	1.035	2.31	12	II
6C0955+3844	1.405	3.45	22	II
6C1011+3632	1.042	2.10	66	II
6C1016+3637	1.892	2.28	31	II
6C1017+3712	1.053	2.68	9	II
6C1018+3729	0.806	2.52	83	II
6C1019+3924	0.922	2.99	9	II
6C1025+3900	0.361	2.97	1	PD(I/II)
6C1031+3405	1.832	2.33	3	II
6C1042+3912	1.770	2.68	11	II
6C1043+3714	0.789	2.62	5	II
6C1045+3403	1.827	2.00	22	II
6C1045+3553	0.851	2.07	9	JD(I/II)
6C1045+3513	1.604	3.03	0.1	CSS(C)
6C1100+3505	1.440	2.26	14	II
6C1108+3956	0.590	2.10	16	JD(I/II)
6C1113+3458	2.406	2.33	17	II
6C1123+3401	1.247	3.40	0.2	II
6C1125+3745	1.233	2.07	18	II
6C1129+3710	1.060	2.36	19	II
6C1130+3456	0.512	3.20	78	II
6C1134+3656	2.125	2.07	17	II
6C1141+3525	1.781	2.40	12	II
6C1143+3703	1.960	2.06	0.1	CSS(C)
6C1148+3638	0.141	3.21	27	FD(I/II)
6C1148+3842	1.303	3.83	10	II
6C1158+3433	0.530	2.12	40	II
6C1159+3651	1.400	2.20	2	CSS(II)

Name	z	S_{151}/Jy	θ/arcsec	Morphology
6C1204+3708	1.779	3.92	51	II
6C1204+3519	1.376	3.43	63	II
6C1205+3912	0.243	3.83	24	JD(I/II)
6C1212+3805	0.947	2.14	0.6	CSS(II)
6C1213+3504	0.857	2.39	0.1	CDD(II)
6C1217+3645	1.089	2.40	0.5	JD(I/II)
6C1220+3723	0.489	2.52	36	II
6C1230+3459	1.533	2.90	12	II
6C1232+3942	3.221	3.27	51/8.7	II
6C1255+3700	0.710	3.66	0.6/1.1	CSS(C)
6C1256+3648	1.128	2.88	18	II
6C1257+3633	1.004	2.40	40	II
6C1301+3812	0.470	3.46	28	II

Table B.1: Parameters of 6CE sample used in my work. Column 1: 6CE source name. Column 2: redshifts of the sources. Column 3: Flux density at $151MHz$. Column 4: Angular size in arcseconds. Column 5: The radio morphology following the definition of Law-Green et al. (1995).The data is taken from various of publications, including Eales (1985); Naundorf et al. (1992); Law-Green et al. (1995); Rawlings et al. (2001)

Appendix C

7CRS sample

C.1 7C-I

Name	z	Linear size (kpc)	$\log_{10}(P_{151})$ $WHz^{-1}sr^{-1}$	FR	Program code	Band	Config.
5C6.5	1.038	186.4	26.31	II	AB371	L	A
5C6.8	1.213	47.4	26.83	C	AR335	X	A
5C6.17	1.05	396.1	26.56	II	AB371	L	A
5C6.19	0.799	68.3	26.51	II	AR335	L	A
5C6.24	1.073	11.1	26.68	II	AB766	X	A
5C6.25	0.706	198.2	26.08	I	AL355	L	A
5C6.29	0.72	92.4	25.94	II	AL355	L	A
5C6.33	1.496	124	26.65	II	AB371	L	A
5C6.34	2.118	66.4	27.13	II	AL355	C	A
5C6.39	1.437	214.5	26.59	I	AL355	L	A
5C6.43	0.775	31.6	26.16	I	AB371	L	A
5C6.62	1.45	271	26.93	I	AL355	L	A
5C6.63	0.465	370.6	25.66	II	AR477	X	ch0
5C6.75	0.775	112	25.94	II	AR365	L	A

Name	z	Linear size (kpc)	$\log_{10}(P_{151})$ $WHz^{-1}sr^{-1}$	FR	Program code	Band	Config.
5C6.83	1.8	119	27.2	II	AR365	L	A
5C6.78	0.263	1459.7	25.62	II	AB667	?	?
5C6.95	2.877	113	27.55	II	AR335	L	A
5C6.160	1.624	53.5	26.88	II	AB371	L	A
5C6.201	0.595	76.9	26.12	I	AR365	L	ch0
5C6.214	0.595	216.4	25.98	II	AR477	X	ch0
5C6.217	1.41	103.1	27.13	II	AR335	L	A
5C6.233	0.56	48.3	26.07	II	AL355	C	A
5C6.237	1.62	23.8	27.11	C	AR365	X	A
5C6.239	0.805	616.4	26.2	II	AB766	C	B
5C6.242	1.9	42.6	27.06	II	AR365	X	A
5C6.251	1.665	50.7	26.7	II	AR365	L	A
5C6.258	0.752	2.4	26	c	AR365	X	A
5C6.264	0.831	40.6	26.28	II	AL355	C	A
5C6.267	0.357	23.7	25.16	II	AB766	X	A
5C6.279	0.473	183.6	25.55	I	AR365	L	A
5C6.282	2.195	8	27.04	C	AR365	X	A
7C0221+3417	0.852	140.8	26.8	II	AL355	L	A
5C6.286	1.339	140.3	26.65	II	AL355	L	A
5C6.288	2.982	7.3	27.6	C	AR335	X	A
5C6.287	2.296	103.9	27.57	II	AR335	L	A
5C6.291	2.91	4.4	27.57	C	AB667	X	A
5C6.292	1.241	41.4	26.72	II	AB371	L	A

Table C.1: Data for the 7C-I sub-field. Column 1 is the source name, column 2 is the redshift, column 3 is the linear size in kpc, column 4 is the logarithm of the radio luminosity at 151 MHz and column 5 is the morphology classification with 1 indicating FRI, 2 indicating FRII. c indicates an unresolved, compact object. Column 6 is the program code of the VLA observations used for the FR classification. Column 7 is the VLA observational band. Column 8 is the VLA configuration of the program used. The data from Column 2 to Column 4 are taken from Grimes' online table.

C.2 7C-II

Name	z	Linear size (kpc)	$\log_{10}(P_{151})$ $WHz^{-1}sr^{-1}$	FR	Program code	Band	Config.
5C7.7	0.435	13.4	25.58	I	AL355	X	A
5C7.8	0.673	320.3	26.36	II	AB371	C	A
5C7.9	0.233	440.8	25.37	II	AB371	L	A
5C7.10	2.185	170.3	27.54	II	AB371	L	A
5C7.15	2.433	16.4	27.36	C	AR335	X	A
5C7.17	0.936	691.5	26.21	II	AL0401	X	C
5C7.23	1.098	235.2	26.63	II	AB371	L	A
5C7.25	0.671	6.3	25.78	C	AB667	X	A
5C7.47	1.7	1.7	26.79	C	AB371	L	A
5C7.57	1.622	634.7	26.79	II	AB371	C	A
5C7.70	2.617	13.7	27.75	II	AR365	X	A
5C7.78	1.151	187.6	26.99	II	AR365	C	A
5C7.79	0.608	1863.9	25.77	II	AL355	L	C
5C7.82	0.918	358.3	26.28	II	AL355	L	C
5C7.85	0.995	227.4	26.64	II	AL0401	L	A
5C7.87	1.764	94.8	27.17	II	AR335	L	A
5C7.95	1.203	486.8	26.65	II	AL0401	L	A
5C7.106	0.264	104.8	25.28	I	AB371	L	A
5C7.111	0.628	80.4	26.29	I	AB371	L	A
5C7.118	0.527	76.3	26.06	II	AL355	C	A
5C7.125	0.801	120.2	26.15	II	AB371	L	A
5C7.145	0.343	93.2	25.31	II	AB371	L	A
5C7.170	0.268	97.1	25.19	II	AB371	L	A
5C7.178	0.246	121.6	25.15	I	AB371	L	C

Name	z	Linear size (kpc)	$\log_{10}(P_{151})$ $WHz^{-1}sr^{-1}$	FR	Program code	Band	Config.
5C7.194	1.738	16.8	27.3	II	AB371	L	A
5C7.195	2.034	22.1	27.12	II	AB371	C	A
5C7.205	0.71	107.3	26.34	II	AB371	L	A
5C7.208	2	146.7	27.27	II	AL0401	L	A
5C7.223	2.087	42.2	27.07	II	AL355	C	A
5C7.242	0.992	389.9	26.22	I	AL355	L	C
5C7.245	1.61	100.2	27.23	II	AB371	L	A
5C7.269	2.218	61.6	27.21	II	AL355	C	A
5C7.271	2.224	9.6	27.06	II	AR365	X	A
5C7.400	1.883	491.9	27.14	II	AR365	L	A
5C7.403	2.315	15.8	26.96	C	AR365	C	A
7C0825+2446	0.243	375.8	24.94	I	AR365	L	C
7C0825+2443	0.086	122.1	24.86	II	AB371	L	C

Table C.2: Same as Table C.1, but for the 7C-II sub-field.

C.3 7C-III

Name	z	S_{151MHz}/Jy	θ/arcsec	FR
1731+6641	0.561	0.52	0.9	II
1732+6535	0.856	6.17	20	II
1733+6719	1.84	1.55	3	II
1736+6710	0.188	0.82	14.5	I
1740+6640	2.10	0.54	0.5	C
1741+6704	1.054	0.72	4	II
1742+6346	1.27	0.62	51	II
1743+6431	1.70	1.89	45	II
1743+6344	0.324	1.59	14	II
1743+6639	0.272	1.97	50	II

Name	z	S_{151MHz}/Jy	θ/arcsec	FR
1745+6415	0.673	0.59	6	II
1743+6639	0.272	1.97	50	II
1745+6415	0.673	0.59	6	II
1745+6422	1.23	1.41	16	II
1745+6624	3.01	0.51	0.4	C
1747+6533	1.516	2.72	0.7	II
1748+6703	3.20	2.17	14	II
1748+6657	1.045	1.15	0.3	II
1748+6731	0.56	0.64	108	II
1751+6809	1.54	1.03	2	II
1751+6455	0.294	0.65	43	II
1753+6311	1.96	1.06	17	II
1753+6543	0.140	1.62	84	II
1754+6420	1.09	0.50	15	II
1755+6314	0.388	1.19	30	I
1755+6830	0.744	1.11	9	II
1756+6520	1.48	0.67	5	II
1758+6535	0.80	1.13	106	II
1758+6553	0.171	1.30	115	II
1758+6307	1.19	1.86	4	II
1758+6719	2.70	0.76	45	II
1801+6902	1.27	1.37	21	II
1802+6456	2.11	1.97	26	II
1804+6625	1.91	0.55	4	II?
1804+6313	1.50	0.62	29	II

Name	z	$S_{151\mathrm{MHz}}$/Jy	θ/arcsec	FR
1805+6332	1.84	1.01	14	II
1807+6831	0.58	2.12	29	II
1807+6719	2.78	0.71	1.7	II
1807+6841	0.816	0.6	12	II
1811+6321	0.273	0.95	52	II
1812+6814	0.816	0.6	23	II
1813+6846	1.03	1.51	52	II
1813+6439	2.04	0.50	38	II
1814+6702	4.05	2.26	14	II
1814+6529	0.96	1.22	126	II
1815+6805	0.230	1.96	50	II
1815+6815	0.794	1.37	200	II
1816+6710	0.92	2.36	27	II
1816+6605	0.92	1.29	2	II
1819+6550	0.724	1.17	9	II
1820+6657	2.98	0.83	0.4	C
1822+6601	0.37	0.97	52	II
1825+6602	2.38	0.84	3	II
1826+6510	0.646	1.39	34	II
1826+6704	0.287	0.60	19	II
1827+6709	0.48	1.10	17	II

Table C.3: Parameters of 7C-III sub-sample used in my work. Column 1: 7CRS source name. Column 2: redshifts of the sources taken from Lacy (1999). Column 3: Flux density at $151MHz$ taken from Lacy (1999). Column 4: Angular size in arcseconds taken from Lacy (1992).

Appendix D

BRL sample

Name	S_{151}/Jy	α_{408}	θ/arcsec	Morphology	z
0000-177	6.51	0.80	2.7	II	1.465
0003-003	10.45	0.80	4.8	II	1.037
0016-129	6.87	0.95	3.5	II	1.589
0020-253	5.36	0.68	79	II	0.35
0022-297	7.83	0.80	44	II	0.406
0023-263	17.00	0.54	< 5	U	0.322
0032-203	6.87	1.02	1.5	II	0.518
0034-014	9.74	0.71	48	II	0.073
0035-024	16.53	0.80	35	I/II	0.220
0038+097	11.54	0.75	46	II	0.188
0051-038	7.03	0.94	< 20	U	0.210
0055-016	10.88	0.57	134	II?	0.045
0056-172	6.21	1.02	17	II	1.019
0101-128	5.18	0.72	16	II	0.387
0105-163	13.24	0.93	63	II	0.400
0114-211	10.64	0.78	< 2	U	1.41

Name	S_{151}/Jy	α_{408}	θ/arcsec	Morphology	z
0115+027	6.07	1.12	13	II	0.672
0116+082	5.20	0.55	1.8	C	0.594
0117-155	13.52	0.79	11	II	0.565
0125-143	7.43	0.85	15	II	0.372
0128+061	5.15	1.04	65	II	0.660
0128-264	5.36	1.05	33	II	2.348
0132+079	5.99	0.79	9	II	0.499
0139-273	5.04	0.95	12	II	1.44
0148-297	7.04	0.70	138	II	0.41
0155-109	5.36	0.73	1.9	II	0.616
0159-117	5.70	0.59	< 2	U	0.669
0213-132	11.37	0.75	70	II	0.147
0218-021	11.77	1.00	80	II	0.175
0219+082	5.29	0.60	155	II	0.266
0222-234	5.44	0.77	16	II	0.230
0235-197	13.27	0.86	39	II	0.620
0254-236	5.87	1.11	33	II	0.509
0255+058	16.20	0.80	670	I	0.023
0305+039	13.60	0.47	100	I	0.029
0310-150	6.10	0.83	< 10	U	1.769
0320+053	7.13	0.76	< 0.2	U	0.575
0325+023	10.90	0.67	153	II	0.030
0331-013	8.66	0.95	80	I	0.139
0340+048	8.65	0.91	32	II	0.357
0347+057	7.47	0.67	62	II	0.339
0349-146	11.60	1.08	117	II	0.616
0349-278	15.80	0.88	363	II	0.066

Name	S_{151}/Jy	α_{408}	θ/arcsec	Morphology	z
0350-073	10.22	0.98	43	II	0.962
0357-163	5.65	0.91	7.0	II	0.584
0358+004	5.29	0.93	4.5	II	0.426
0403-132	6.70	0.37	< 1.3	U	0.571
0404+035	9.35	0.56	335	II	0.089
0405-123	8.17	0.83	32	II	0.574
0406-180	5.6	0.70	< 5	U	0.722
0413-210	7.3	0.78	5.0	II	0.808
0430+052	6.08	0.36	850	I	0.033
0442-282	18.85	0.83	86	II	0.147
0453-206	11.25	0.73	36	II	0.035
0508-220	5.10	0.80	39	II	0.16
0511+008	8.00	0.80	132	II	0.127
0519-208	7.34	1.09	< 2	U	1.086
0528+064	11.19	1.01	49	II	0.406
0604-203	7.39	0.75	< 20	U	0.164
0634-205	22.70	1.07	820	II	0.055
0806-103	13.70	0.99	121	II	0.110
0812-029	9.54	1.28	3.0	C	0.198
0825-202	10.27	0.82	17	II	0.822
0834-196	10.84	0.67	< 5	U	1.032
0850-206	7.49	0.96	13	II	1.337
0851-142	5.19	0.82	7.0	II	1.665
0859-257	17.17	0.81	43	II	0.305
0915-118	132.00	0.95	76	I	0.054
0933+045	5.13	1.35	60	II	1.339
0945+076	15.53	0.92	230	II	0.086
0949+002	12.30	1.10	7.5	II	1.487

Name	S_{151}/Jy	α_{408}	θ/arcsec	Morphology	z
1002-215	6.71	1.50	29	II	0.59
1005+077	15.35	0.69	1.2	II	0.877
1008+066	9.32	0.93	9.8	II	1.405
1039+029	6.38	0.69	6.4	II	0.535
1048-090	5.35	0.79	83	II	0.344
1059-010	8.04	0.86	22	II	
1103-208	7.64	0.90	9.7	II	1.12
1116-027	7.73	1.21	< 1.5	U	1.355
1120+057	5.08	0.86	< 18	U	2.474
1127-145	5.07	-0.08	0.01	C	1.187
1131-171	5.87	1.02	8.0	II	1.618
1136-135	10.50	0.74	16	II	0.557
1138+015	5.72	0.61	5.2	II	0.443
1139-285	6.81	0.79	13	II	0.85
1140-114	5.14	1.07	3.9	II	1.935
1216+061	41.50	0.71	416	I	0.007
1216-100	7.70	0.91	275	II	0.087
1226+023	59.75	0.07	22	C	0.158
1232-249	5.1	0.83	109	II	0.355
1239-044	10.24	0.83	5.4	II	0.480
1245-197	8.61	0.42	< 3.5	U	1.275
1252-122	14.70	0.54	180	I	0.015
1253-055	14.45	0.32	< 4	U	0.538
1303+091	5.21	1.03	8.0	II	1.409
1306-095	7.84	0.50	< 5	U	0.464
1307+000	5.10	0.92	60	II	0.419
1308-220	22.21	1.18	1.1	U	0.8
1327-214	5.63	0.86	31	II	0.528

Name	S_{151}/Jy	α_{408}	θ/arcsec	Morphology	z
1330+022	5.29	0.55	140	II	0.216
1335-061	9.74	0.97	11	II	0.625
1344-078	5.98	0.93	< 10	U	0.384
1354+013	6.59	0.82	33	II	0.819
1411-057	5.49	1.04	47	II	1.094
1413-215	5.57	1.11	19	II	
1416+067	23.36	1.09	1.0	II	1.436
1417-192	5.02	0.76	62	II	0.120
1419-272	8.36	1.02	< 25	U	0.985
1422-297	7.17	0.89	< 10	U	1.632
1425-011	7.21	0.70	< 15	U	1.159
1434+036	5.16	0.49	10	II	1.438
1436-167	5.61	0.85	< 12	U	0.146
1452-041	6.72	0.94	108	II	0.441
1453-109	10.33	0.72	41	II	0.938
1508+080	11.50	0.91	130	II	0.461
1508-055	7.72	0.63	0.02	C	1.185
1509+015	5.56	0.73	7.2	II	0.792
1514+072	25.18	1.23	46	C	0.034
1524-136	6.11	0.61	0.4	U	1.687
1600+021	16.11	0.54	302	II	0.104
1602+014	14.87	1.05	14	II	0.462
1602-093	6.08	0.44	290	II	0.109
1602-174	5.64	1.06	37	II	2.043
1602-288	7.07	0.85	61	II	0.482
1603+001	5.61	0.79	11	I	0.059
1621-115	7.15	0.78	< 20	U	0.375
1628-268	5.66	0.76	93	II	0.166

Name	S_{151}/Jy	α_{408}	θ/arcsec	Morphology	z
1643+022	5.52	0.84	7.1	II	0.095
1643-223	5.68	0.85	12	II	0.799
1648+050	169.50	1.05	202	I/II	0.154
1649-062	5.73	0.86	85	II	0.236
1716+006	5.54	0.75	7.1	II	0.704
1717-009	138.00	0.76	284	II	0.030
1730-130	6.58	0.08	0.03	C	0.902
1732-092	5.30	0.71	45	II	0.317
1810+046	5.51	0.78	6.5	II	1.083
1859-235	10.92	0.88	4.2	II	
1912-269	6.21	0.90	48	II	0.226
1920-077	6.04	0.93	23	II	0.648
1921-293	5.63	-0.70	0.01	C	0.352
1938-155	16.00	0.70	5.5	II	0.452
1949+023	13.57	0.73	230	II	0.059
1953-077	5.88	0.96	4.3	II	
2019+098	10.00	0.89	27	II	0.467
2025-155	5.41	1.05	15	II	1.500
2030-230	6.45	0.76	70	II	0.132
2044-027	5.37	0.69	< 2	U	0.942
2045+068	7.86	0.96	35	II	0.127
2053-201	6.37	0.69	30	II	0.156
2058-282	15.90	0.84	230	I	0.038
2104-256	13.25	0.75	114	II	0.037
2111-259	5.27	0.66	9.0	II	0.602
2113-211	9.05	0.95	40	II	0.698
2120-166	6.09	1.08	14	II	0.882
2128-208	6.15	0.88	< 1	U	1.615

Name	S_{151}/Jy	α_{408}	θ/arcsec	Morphology	z
2135-147	8.78	0.67	149	II	0.200
2135-209	9.76	0.78	< 2	U	0.635
2146-133	5.10	0.84	3.6	II	1.800
2149-200	5.12	0.77	2.0	II	0.424
2149-287	5.68	0.55	< 2	U	0.479
2154-184	6.09	0.97	78	II	0.668
2203-188	9.73	0.34	< 6	U	0.618
2211-172	28.66	0.95	118	II	0.153
2216-281	6.24	0.91	< 2	U	0.657
2221-023	0.99	0.24	570	II	0.056
2223-052	11.89	0.38	0.32	C	1.404
2309+090	6.25	0.75	12	II	0.233
2310+050	7.08	0.72	160	II	0.289
2314+038	15.78	0.99	13	II	0.220
2317-277	5.44	0.72	160	II	0.173
2318-166	8.75	1.06	< 5	U	1.414
2322-052	5.43	1.02	7.8	II	1.188
2322-123	7.20	1.09	7.0	U	0.082
2324-023	5.57	0.69	92	U	0.188
2338+042	5.70	1.03	2.7	II	2.594
2347-026	5.46	0.89	< 2	U	1.036

Table D.1: Properties of the sources in the BRL sample, taken from Table 3 in Best et al. (1999). Column 1: source name. Column 2: integrated flux density at 408 MHz. Column 3: spectral index at 408 MHz. Column 4: angular size of the radio sources. Column 5: morphological classification. Collumn 6: redshift.

Bibliography

Alexander P., 2000, MNRAS, 319, 8

Alexander P., Leahy J. P., 1987, MNRAS, 225, 1

Baan W. A., 1980, ApJ, 239, 433

Baldwin J. E., 1982, in Heeschen D. S., Wade C. M., eds, Extragalactic Radio Sources Vol. 97 of IAU Symposium, Evolutionary tracks of extended radio sources. pp 21–24

Barai P., Wiita P. J., 2006, MNRAS, 372, 381

Barai P., Wiita P. J., 2007, ApJ, 658, 217

Begelman M. C., 1982, in Heeschen D. S., Wade C. M., eds, Extragalactic Radio Sources Vol. 97 of IAU Symposium. Kluwer, Dordrecht, pp 223–225

Begelman M. C., Cioffi D. F., 1989, ApJ, 345, L21

Bennett A. S., 1962, MNRAS, 125, 75

Best P. N., Longair M. S., Rottgering H. J. A., 1996, MNRAS, 280

Best P. N., Peacock J. A., Brookes M. H., Dowsett R. E., Röttgering H. J. A., Dunlop J. S., Lehnert M. D., 2003, MNRAS, 346, 1021

Best P. N., Röttgering H. J. A., Lehnert M. D., 1999, MNRAS, 310, 223

Best P. N., Röttgering H. J. A., Lehnert M. D., 2000, MNRAS, 315, 21

Bicknell G. V., 1994, ApJ, 422, 542

Bicknell G. V., Sutherland R. S., van Breugel W. J. M., Dopita M. A., Dey A., Miley G. K., 2000, ApJ, 540, 678

Bird J., Martini P., Kaiser C., 2008, ApJ, 676, 147

Birkinshaw M., Worrall D. M., 1993, ApJ, 412, 568

Bîrzan L., McNamara B. R., Nulsen P. E. J., Carilli C. L., Wise M. W., 2008, ApJ, 686, 859

Blandford R. D., Rees M. J., 1974, MNRAS, 169, 395

Blundell K. M., Rawlings S., 1999, Nature, 399, 330

Blundell K. M., Rawlings S., 2002, ArXiv Astrophysics e-prints

Blundell K. M., Rawlings S., Willott C. J., 1999, AJ, 117, 677

Bohringer H., Nulsen P. E. J., Braun R., Fabian A. C., 1995, MNRAS, 274, L67

Bowman M., Leahy J. P., Komissarov S. S., 1996, MNRAS, 279, 899

Bridle A. H., 1984, AJ, 89, 979

Canto J., Raga A. C., 1991, ApJ, 372, 646

Canvin J. R., Laing R. A., 2004, MNRAS, 350, 1342

Canvin J. R., Laing R. A., Bridle A. H., Cotton W. D., 2005, MNRAS, 363, 1223

Chokshi A., 1997, ApJ, 491, 78

Chyzy K. T., 1997, MNRAS, 289, 355

Clarke D. A., Burns J. O., Norman M. L., 1989, ApJ, 342, 700

De Young D. S., 1981, Nature, 293, 43

Dey A., van Breugel W., Vacca W. D., Antonucci R., 1997, ApJ, 490, 698

Dunlop J. S., Peacock J. A., 1990, MNRASs, 247, 19

Eales S. A., 1985, MNRAS, 217, 149

Falle S. A. E. G., 1991, MNRAS, 250, 581

Fanaroff B. L., Riley J. M., 1974, MNRAS, 167, 31P

Fasano G., Franceschini A., 1987, MNRAS, 225, 155

Ferrari A., 1998, ARA&A, 36, 539

Fukazawa Y., Makishima K., Ohashi T., 2004, PAsJ, 56, 965

Furlanetto S. R., Loeb A., 2001, ApJ, 556, 619

Gopal-Krishna Wiita P. J., 2001, ApJ, 560, L115

Gopal-Krishna Wiita P. J., Saripalli L., 1989, MNRAS, 239, 173

Greve T. R., Ivison R. J., Stevens J. A., 2006, Astronomische Nachrichten, 327, 208

Grimes J. A., Rawlings S., Willott C. J., 2004, MNRAS, 349, 503

Hardcastle M. J., Worrall D. M., Birkinshaw M., Laing R. A., Bridle A. H., 2002, MNRAS, 334, 182

Hardcastle M. J., Worrall D. M., Birkinshaw M., Laing R. A., Bridle A. H., 2005, MNRAS, 358, 843

Hill G. J., Rawlings S., 2003, New Astronomy Review, 47, 373

Hogg D. W., 1999, ArXiv Astrophysics e-prints

Hopkins P. F., Richards G. T., Hernquist L., 2007, ApJ, 654, 731

Inskip K. J., Best P. N., Rawlings S., Longair M. S., Cotter G., Röttgering H. J. A., Eales S., 2002, MNRAS, 337, 1381

Jackson C. A., Wall J. V., 1999, MNRAS, 304, 160

Jetha N. N., Ponman T. J., Hardcastle M. J., Croston J. H., 2007, MNRAS, 376, 193

Kaiser C. R., Alexander P., 1997, MNRAS, 286, 215

Kaiser C. R., Alexander P., 1999, MNRAS, 305, 707

Kaiser C. R., Best P. N., 2007, MNRAS, 381, 1548

Kaiser C. R., Dennett-Thorpe J., Alexander P., 1997, MNRAS, 292, 723

Kauffmann G., Heckman T. M., Tremonti C., Brinchmann J., Charlot S., White S. D. M., Ridgway S. E., Brinkmann J., Fukugita M., Hall P. B., Ivezić Ž., Richards G. T., Schneider D. P., 2003, MNRAS, 346, 1055

Kawakatu N., Kino M., Nagai H., 2009, ApJ, 697, L173

Komissarov S. S., 1994, MNRAS, 269, 394

Kormendy J., Richstone D., 1995, ARA&A, 33, 581

Kronberg P. P., Dufton Q. W., Li H., Colgate S. A., 2001, ApJ, 560, 178

Lacy M., Rawlings S., Hill G. J., Bunker A. J., Ridgway S. E., Stern D., 1999, MNRAS, 308, 1096

Laing R. A., 1993, in Burgarella D., Livio M., O'Dea C. P., eds, Astrophysical Jets, Vol. 6 of STScI Symposium Series. Cambridge University Press, Cambridge, p. 95

Laing R. A., Bridle A. H., 2002a, MNRAS, 336, 1161

Laing R. A., Bridle A. H., 2002b, MNRAS, 336, 328

Laing R. A., Canvin J. R., Bridle A. H., Hardcastle M. J., 2006, MNRAS, 372, 510

Laing R. A., Riley J. M., Longair M. S., 1983, MNRAS, 204, 151

Law-Green J. D. B., Leahy J. P., Alexander P., Allington-Smith J. R., van Breugel W. J. M., Eales S. A., Rawlings S. G., Spinrad H., 1995, MNRAS, 274, 939

Leahy J. P., Williams A. G., 1984, MNRAS, 210, 929

Ledlow M. J., Owen F. N., 1996, AJ, 112, 9

Lind K. R., Payne D. G., Meier D. L., Blandford R. D., 1989, ApJ, 344, 89

Longair M. S., 1966, MNRAS, 133, 421

Longair M. S., 1994, High energy astrophysics. Vol.2: Stars, the galaxy and the interstellar medium

Lynden-Bell D., 1969, Nature, 223, 690

Magorrian J., Tremaine S., Richstone D., Bender R., Bower G., Dressler A., Faber S. M., Gebhardt K., Green R., Grillmair C., Kormendy J., Lauer T., 1998, AJ, 115, 2285

Manolakou K., Kirk J. G., 2002, A&A, 391, 127

McGilchrist M. M., Baldwin J. E., Riley J. M., Titterington D. J., Waldram E. M., Warner P. J., 1990, MNRAS, 246, 110

Meier D. L., Edgington S., Godon P., Payne D. G., Lind K. R., 1997, Nature, 388, 350

Nath B. B., 1995, MNRAS, 274, 208

Naundorf C. E., Alexander P., Riley J. M., Eales S. A., 1992, MNRAS, 258, 647

Neeser M. J., Eales S. A., Law-Green J. D., Leahy J. P., Rawlings S., 1995, ApJ, 451, 76

Oort M. J. A., Katgert P., Windhorst R. A., 1987, Nature, 328, 500

O'Sullivan E., Forbes D. A., Ponman T. J., 2001, MNRAS, 328, 461

Owen F. N., Laing R. A., 1989, MNRAS, 238, 357

Owen F. N., Ledlow M. J., 1994, in Bicknell G. V., Dopita M. A., Quinn P. J., eds, The Physics of Active Galaxies Vol. 54 of Astronomical Society of the Pacific Conference Series, The FRI/Il Break and the Bivariate Luminosity Function in Abell Clusters of Galaxies. pp 319–+

Owen F. N., White R. A., 1991, MNRAS, 249, 164

Parma P., Murgia M., de Ruiter H. R., Fanti R., 2002, New Astronomy Review, 46, 313

Peacock J. A., 1983, MNRAS, 202, 615

Peacock J. A., 1985, MNRAS, 217, 601

Pearson T. J., Kus A. J., 1978, MNRAS, 182, 273

Phinney E. S., 1983, PhD thesis, University of Cambridge

Rawlings S., Eales S., Lacy M., 2001, MNRAS, 322, 523

Rawlings S., Jarvis M. J., 2004, MNRAS, 355, L9

Rawlings S., Saunders R., 1991, Nature, 349, 138

Reynolds C. S., Brenneman L. W., Stocke J. T., 2005, MNRAS, 357, 381

Scheuer P. A. G., 1974, MNRAS, 166, 513

Seyfert C. K., 1943, ApJ, 97, 28

Shklovskii I. S., 1963, Soviet Astronomy, 6, 465

Silk J., 2005, MNRAS, 364, 1337

Snellen I. A. G., Best P. N., 2001, MNRAS, 328, 897

Ueda Y., Akiyama M., Ohta K., Miyaji T., 2003, ApJ, 598, 886

Urpin V., 2002, A&A, 385, 14

Wall J. V., 1980, Royal Society of London Philosophical Transactions Series A, 296, 367

Wang Y., Kaiser C. R., 2008, MNRAS, 388, 677

Wang Y., Kaiser C. R., Laing R., Alexander P., Pavlovski G., Knigge C., 2009, MNRAS, 397, 1113

Willott C. J., Rawlings S., Blundell K. M., Lacy M., Eales S. A., 2001, MNRAS, 322, 536

Willott C. J., Rawlings S., Blundell K. M., Lacy M., Hill G. J., Scott S. E., 2002, MNRAS, 335, 1120

Willott C. J., Rawlings S., Jarvis M. J., Blundell K. M., 2003, MNRAS, 339, 173

Worrall D. M., Birkinshaw M., Hardcastle M. J., 2003, MNRAS, 343, L73